ACOUSTICALLY DRIVEN PIEZOELECTRIC RADIATING ELEMENTS

BY

MICHAEL BREEN

DISSERTATION

Submitted in partial fulfillment of the requirements
for the degree of Doctor of Philosophy in Electrical and Computer Engineering
in the Graduate College of the
University of Illinois at Urbana-Champaign, 2020

Urbana, Illinois

Doctoral Committee:

Associate Professor Songbin Gong, Chair
Professor Jennifer Bernhard
Associate Professor Minjoo Lawrence Lee
Assistant Professor Jin Zhou

Abstract

This dissertation reports the development of novel acoustically driven, lead zirconate titanate (PZT) piezoelectric radiators for very low frequency (VLF: 3-30 kHz) and low frequency (LF: 30-300 kHz) electromagnetic communication. The low propagation loss of electromagnetic radiation below 1 MHz exhibits great potential for low-power, long-range communication systems. However, the fundamental reduction in efficiency as antenna size decreases below a wavelength (30 m at 1 MHz) has made portable communication systems in the VLF and LF ranges impractical. A paradigm shift from electrical antennas to acoustically driven antennas operating at resonant wavelengths up to 10^5 times smaller than electrical antennas offers great potential for portable, low-power communication systems in the VLF and LF ranges.

In this dissertation, a theoretical analysis is presented for the primary methods of implementing acoustically driven radiating elements, investigating both the radiation and matching efficiencies comprising the total antenna efficiency. Radiation from the linear movement of unipolar charge driven both piezoelectrically and capacitively, the piezoelectrically actuated rotation of fixed dipole charges, and from alternating dipoles inside strain driven piezoelectric resonators are all presented and analyzed in terms of their design parameters and fundamental challenges. Unipolar and fixed dipolar charge-based approaches are unable to sustain sufficient charge density to achieve efficient radiation due to electrical breakdown and charge decay respectively. The dynamic polarization flipping inside strain driven piezoelectric alternating dipole antennas (PADAs) circumvents the decay and breakdown complications of static charge approaches and is well suited to surpassing the efficiency of equivalent electrical antennas by multiple orders of magnitude.

Here, a VLF PZT PADA is demonstrated which leverages a high piezoelectric coupling (d_{31} = 108 pC/N) and moderate quality factor (Q = 1340) to achieve an efficiency that surpasses that of similarly sized dipole antennas by more than 6000 times, significantly improving the portable VLF antenna state-of-the-art. The moderate Q allows the PADA to be directly modulated with bit rates up to 60 bit/s without the need for additional circuitry. However, despite the increased efficiency, the radiated power of the PADAs demonstrated to date remains limited for long-distance communication applications and significant improvements radiated power are required to approach commercial viability. The maximum radiated power of PADAs utilizing high Q, moderate permittivity materials, such as LiNbO$_3$, have been limited by electrical field breakdown near the resonator due to large induced surface charge density. High coupling, high permittivity materials, such as PZT, offer increased field confinement and thus greater effective piezoelectric currents without breakdown. However, the diminished Q results in increased heat dissipation and a corresponding loss in radiation efficiency due to thermal nonlinearity.

To overcome the power handling limitation of individual PADA elements, a PZT rod PADA is presented exhibiting enhanced efficiency and power handling compared to the initial PZT disk prototype. A thickness extensional mode using a higher coupling d_{33} mode is utilized to increase the PADA figure of merit and radiation efficiency. An eight-element proof of concept array is fabricated to demonstrate the potential of parallelism to bolster power handling and radiated power. The eight-element array exhibits a 17-fold increase in radiation efficiency and 5-fold increase in radiated field strength, demonstrating the potential of larger PADA arrays for extending communication ranges.

Acknowledgments

First and foremost, I would like to express my thanks to my doctoral advisor Professor Songbin Gong without whom this work would not have been possible. While his funding support was essential to my success, I am most thankful for his mentorship that helped me grow to be a more diligent, logical and creative researcher. He was patient even when I may not have deserved it and motivated me to surpass the goals I set for myself. “Shoot for the moon,” he’d say. “Even if you miss, you’ll land among the stars.”

Additionally, I would like to thank my friends in the Illinois Integrated RF Microsystems group for their friendship and assistance. In particular, I’d like to thank Dr. Ming-Huang Li and Ahmed Hassanien, who worked closely with me to develop and test the piezoelectric transmitters detailed here. Especially Ahmed, who spent long hours brainstorming, modeling and measuring with me, even outside in subfreezing temperatures. Special thanks must also be given to Dr. Yansong Yang and Dr. Anming Gao who spent long hours with me in the cleanroom collaborating and sharing their expertise as well as Dr. Ruochen Lu who also seems to have innovative solutions to difficult problems.

On a personal note, I’d like to thank my parents, Deb and Bob, for their constant support and love, as well as my brother, Patrick, who always keeps me centered.

Last, but never least, my partner Sarah. Words can’t describe how much I appreciated her patience, love and support throughout my doctoral studies. Her perseverance was, and remains, a constant source of inspiration and motivation.

Contents

Chapter 1: Introduction

Portable wireless devices have become ubiquitous over the last decade, and with the growth of the internet of things (IoT), demand for small, efficient wireless communication systems continues to accelerate. While the development of wireless systems has kept pace with demand at higher frequencies, progress toward portable low-frequency systems has been stagnant for nearly a century. Compact antennas at the very high frequency (VHF: 30-300 MHz) and ultra-high frequency (UHF: 300-3000 MHz) are well developed and suited for transmitting data at high bit rates. However, as spectral crowding of those bands increases, there is a need to look toward new frequency bands to meet future wireless needs. Demand for faster and more compact wireless systems is omnipresent, prompting significant research toward opening new high-frequency bands for the newest generation of wireless communication [1]. Higher operating frequency enables faster communication rates, but it also comes with greater free-space path loss which generally increases with the square of frequency ($\text{FSPL} \propto f^2$), making it unsuitable for long-distance, low-power wireless applications. Growing demand for a widespread internet of things (IoT) consisting of extensive wireless sensor networks, many of which require only moderate bit rates to periodically send small packets of information [2]. Instead, low power consumption is often prioritized in order to maximize sensor lifetime [3], [4]. Especially for widespread arrays of remote, low-power sensors in hard-to-access rural areas, there is a need for low FSPL to increase battery life and enable communication to distant base stations.

Compared to VHF and UHF signals, radiation at the ultra-low (ULF: 0.3-3 kHz) and very low frequency (VLF: 3-30 kHz) ranges exhibits relatively low propagation loss, enabling communication underwater up to 20 meters [5] and through hundreds of feet of earth [6]. Additionally, VLF radiation can propagate as ground waves that reflect back and forth between the Earth's surface and ionosphere with very low atmospheric attenuation of ~2-3 dB/100 km [7]. These propagation characteristics are well suited for long-range, low-power communication elements over remote or rugged terrain for IoT and defense [8] applications. However, while the desirable propagation properties ensure continued demand for compact, long-range VLF transmitters, the use of VLF antennas has been largely restricted to submarines [9], [10] and large base installations [11], [12] such as the VLF transmitter array in Cutler, Maine. Reducing VLF antennas to below 10s-100s of meters has proven untenable as the power savings from reduced propagation loss is negligible to the reduced efficiency as VLF transmitters become electrically small.

1.1 Challenges of Electrically Small Antennas

Miniaturizing electrical systems has been a common goal across engineering disciplines for decades, yet the size of VLF antennas has remained largely unchanged since Guglielmo Marconi debuted them in the early 1900s due to a fundamental tradeoff between antenna efficiency, bandwidth and size. The primary function of antennas is to wirelessly transfer information or energy from one location to another. While the exact specifications of antennas differ from application to application, they must generally meet certain power budget, bandwidth and size requirements. For IoT, antennas should be small enough to not interfere with the monitored surroundings, while point-to-point defense communication necessitates antennas that are compact and portable. However, as the physical size of antennas gets smaller than one-tenth of a wavelength in size, λ/10, their efficiency tends to decrease significantly, and they are termed electrically small antennas (ESAs). Antennas operating at 1 GHz, have a wavelength of 30 cm, enabling them to be used in handheld devices without significant loss in efficiency. On the other hand, antennas at 30 kHz have a wavelength of 10 km, requiring compact VLF antennas to be extremely sub-wavelength in physical size. Extremely sub-wavelength ESAs exhibit diminished radiation resistance which leads to reduced radiation efficiency and greater power consumption to maintain the same signal strength at the receiver [13]. Additionally, antennas with extremely subwavelength physical dimensions experience an exponential increase in their quality factor (Q) which is inversely proportional to the antenna bandwidth. Since bandwidth determines data-rate, data transmission can be very difficult for very small ESAs. Thus, despite the valuable low propagation properties, compact or handheld VLF antennas have been impractical due to low efficiency and data link capabilities.

1.1.1 Diminished Efficiency

For VLF transmitters to be viable, they must achieve a lower total power consumption relative to higher frequency antennas of similar physical size. Total power consumption for a communication link is generally characterized by the Friis transmission formula [14] as:

$$P_R = \frac{P_T G_T G_R c^2}{(4\pi R f)^2} \tag{1.1}$$

where P_R is the power at the receiver inputs, P_T is the power delivered to the transmitting antenna, c is the speed of light, R is the distance between the transmitter and receiver and f is the operating frequency. The gain of the transmitting and receiving antennas respectively are G_T and G_R, where the gain is defined as:

$$G = \eta_{rad} D \tag{1.2}$$

and is the product of the radiation efficiency η_{rad} and the directivity D of the antenna. Typically (1.1) and (1.2) are used to describe antenna systems which can be impedance matched to the power source and thus matching efficiency is ignored. However, as will be discussed later in this section, that assumption does not hold for compact VLF systems which exhibit physical sizes much less than one wavelength. Therefore, it is informative to redefine (1.1) in terms of the power available from the transmitting source P_T^{av}, and (1.2) as a function of the total antenna efficiency.

$$\eta_{tot} = \eta_\Gamma \eta_{rad} = \frac{P_{del}}{P_{av}} \frac{P_{rad}}{P_{del}} = \frac{P_{rad}}{P_{av}} \tag{1.3}$$

where for a transmitting antenna the matching efficiency η_Γ is the ratio of how much of the power available from the source is delivered to the antenna and the radiation efficiency η_{rad} is the ratio of how much of the power delivered to the antenna is radiated. Thus, a figure of merit (FoM) for a low-power transmitter can be written as:

$$FoM = \frac{D \eta_{tot}}{(Rf)^2} \tag{1.4}$$

It should be noted that both (1.1) and (1.4) are contingent upon assumptions that the antennas are aligned, there is no polarization mismatch between the transmitter and receiver, and that there is a clear line of sight between the antennas. For long-distance communication that occurs with very remote sensing or defense applications, VLF communication would exhibit superior diffraction around obstacles and rough terrain compared to higher frequency signals due to the longer wavelength. However, due to the application-specific nature of non-free space propagation, it is neglected here for a more general FoM. Equation (1.4) also neglects other communication considerations such as data rate, for which higher frequency antennas offer superior communication speeds, and is, therefore, addresses only one aspect of a communication link.

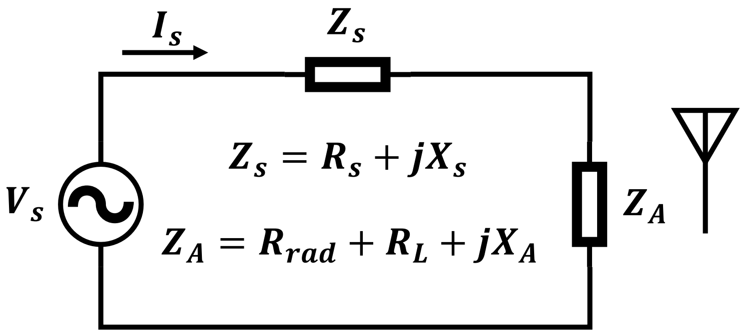

Fig. 1.1. Equivalent circuit model of an electrical antenna.

From (1.4), there is a clear tradeoff between antenna efficiency and operating frequency for small antennas. For a compact, VLF or LF transmitter, antenna design must balance the diminished efficiency of electrically small antennas operating at low wavelengths against the increased propagation loss of higher frequency antennas. Antenna efficiency is defined in terms of the source and antenna impedances. The equivalent circuit model of a transmitting antenna is shown in Fig. 1.1 where R_S and X_S are the resistive and reactive components of the source impedance respectively and I_s is the current supplied by the source to the antenna terminals. Since antennas are reciprocal devices, the impedance terms are the same for an antenna operating in receiving mode. The antenna is characterized by an impedance $Z_A = R_{rad} + R_L + jX_A$ where R_{rad} and R_L represent the energy dissipated in the antenna through radiation or ohmic losses respectively and X_A represents the power stored in the antenna near-field. The power radiated from the antenna and the power delivered to the antenna can then be defined in terms of the equivalent circuit parameters as:

$$P_{rad} = \frac{|I_s|^2 R_{rad}}{2} = \frac{|V_s|^2}{2}\left(\frac{R_{rad}}{(R_{rad} + R_L + R_s)^2 + (X_A + X_s)^2}\right) \qquad (1.5)$$

$$P_{del} = \frac{|I_s|^2 R_A}{2} = \frac{|V_s|^2}{2}\left(\frac{R_{rad} + R_L}{(R_{rad} + R_L + R_s)^2 + (X_A + X_s)^2}\right) \qquad (1.6)$$

where V_s is the source voltage. From (1.5) and (1.6), maximum radiation efficiency occurs when $R_{rad} \gg R_L$. In general, for antenna where the length of the largest dimension is l, the radiation resistance is inversely proportional to that length squared ($R_{rad} \propto l^2/\lambda^2$) [15], [16] while the ohmic loss is proportional to length ($R_L \propto l$). As $l \ll \lambda$, the resistive loss begins to dominate and

$$P_{rad} = \frac{R_{rad}}{R_{rad} + R_L} \propto \frac{l}{\lambda^2} \tag{1.7}$$

Maximum matching efficiency occurs when the source impedance is conjugately matched to the antenna impedance ($Z_A = Z_S^*$) and all the power available from the source is delivered to the antenna.

$$P_{av} = P_{del}^{matched} = \frac{|V_S|^2}{2}\left(\frac{1}{4R_s}\right) \tag{1.8}$$

Then (1.3) can be rewritten in terms of the antenna circuit parameters as:

$$\eta_{tot} = \frac{P_{rad}}{P_{av}} = \frac{4R_{rad}R_s}{(R_{rad} + R_L + R_s)^2 + (X_A + X_s)^2} \tag{1.9}$$

However, as the size of electrical antennas becomes much smaller than a wavelength, the reactive component of the antenna impedance becomes increasingly large ($X_A \propto l/\lambda$). The small radiation resistance in conjunction with the much larger antenna reactance results in a large impedance mismatch with the driving electronics.

$$\eta_\Gamma = \frac{P_{del}}{P_{av}} \tag{1.10}$$

1.1.2 High Q and Low Bandwidth

In addition to the decreased efficiency, the large reactive impedance component of ESAs results in a large quality factor which is defined as:

$$Q_{tot} = \frac{2\omega * \text{Energy Stored}}{\text{Power Dissipated}} = \frac{1}{\frac{1}{Q_o} + \frac{1}{Q_A}} \tag{1.11}$$

where ω is the angular frequency of operation and Q_A and Q_o represent the power dissipated radiation and ohmic losses respectively. The high Q of ESAs corresponds to a low antenna bandwidth, defined as $B = 1/Q$, which limits the transmitted bitrate capacity of the antenna according to the Shannon-Hartley theorem [17]

$$C = B\log_2(1 + \frac{S}{N}) \tag{1.12}$$

where C is the bit capacity of the transmission channel and S/N is the signal to noise ratio of the radiated signal. Improvement in the bandwidth can be achieved by increasing resistive losses in the antenna, but only at the expense of radiation efficiency.

Analysis of the fundamental relationship between antenna size and Q was first conducted by Wheeler [18] and Chu [19] in the 1940s. Extensive subsequent work [20]–[23] defined the limit on the minimum Q of an antenna as $Q \geq 1/(ka) + 1/(ka)^3$ where $k = 2\pi/\lambda$ is the electromagnetic wavenumber and a is the radius of the smallest sphere that contains the antenna. For a handheld antenna in the VLF range with a ka product $<10^{-4}$ the resulting bandwidth is on the order of μHz, untenable for data communication [24], [25].

1.1.3 State-of-the-Art Electrically Small Antennas

For ESAs to be viable as low-frequency transmitters, they must maximize their efficiency to increase the FoM in (1.4). It is clear from the Chu limit that antennas scale unfavorably as the physical size gets small relative to electrical wavelength, but the exact scaling depends on the antenna implementation. The simplest form of electrically small antennas is the ideal dipole comprised of a uniform linear current with a physical length much smaller than the electromagnetic wavelength that it radiates ($L \ll \lambda$). Although the ideal dipole is non-physical, since the currents at the ends of the element must reduce to zero due to the open boundary condition, it serves as a useful model for small current elements since larger current elements can be discretized into smaller lengths of uniform current which can be modeled as an ideal dipole. The fields generated from an ideal dipole can be written as:

$$\boldsymbol{H} = \frac{IL}{4\pi} j\beta \left(1 + \frac{1}{j\beta r}\right) \frac{e^{-j\beta r}}{r} \sin(\theta)\, \hat{\boldsymbol{\phi}} \tag{1.13}$$

$$\boldsymbol{E} = \frac{IL}{4\pi}\frac{e^{-j\beta r}}{r}\left[j\omega\mu\left(1+\frac{1}{j\beta r}-\frac{1}{(\beta r)^2}\right)\sin(\theta)\,\widehat{\boldsymbol{\theta}} + 2\eta\left(1-\frac{1}{j\beta r^2}\right)\cos(\theta)\,\hat{\boldsymbol{r}}\right] \tag{1.14}$$

where r is the measurement distance as shown in Fig. 1.2, ω is the angular propagation frequency, I is the current magnitude in the z-direction, L is the length of the current element, and β, μ, and η are the propagation constant, permeability and intrinsic impedance of the propagation medium. At distances far from the antenna, the $1/r^2$ and $1/r^3$ terms, called near-field terms because they are the dominant field term near the antenna, become negligible and the fields are fully described by the radiating $1/r$ (far-field) term:

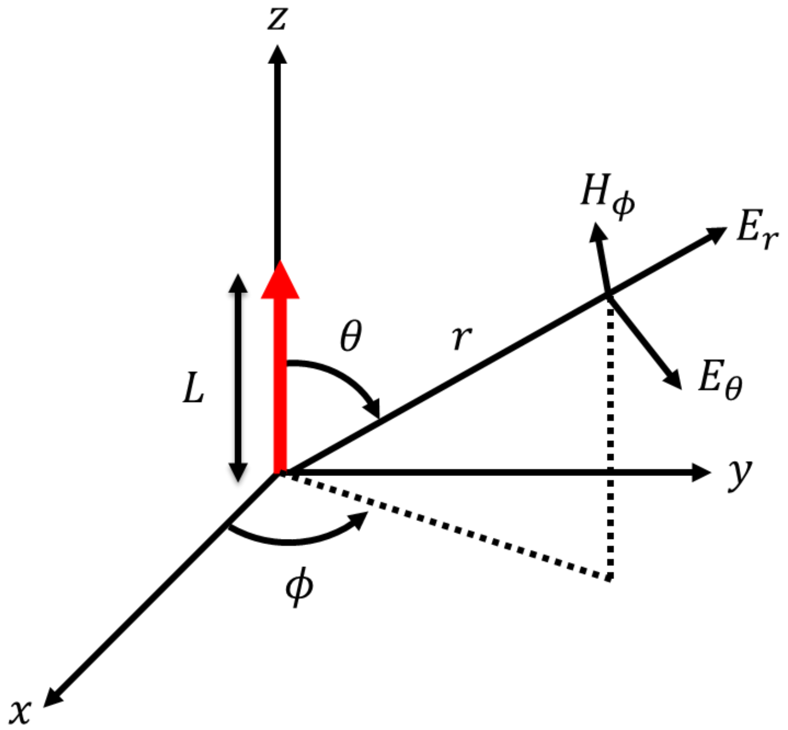

Fig. 1.2. Mock-up of ideal dipole and radiated field components.

$$\boldsymbol{H_{ff}} = \frac{Il}{4\pi}j\beta\frac{e^{-j\beta r}}{r}\sin(\theta)\,\widehat{\boldsymbol{\phi}} \tag{1.15}$$

$$\boldsymbol{E_{ff}} = \frac{Il}{4\pi}\frac{e^{-j\beta r}}{r}j\omega\mu\sin(\theta)\,\widehat{\boldsymbol{\theta}} \tag{1.16}$$

For an ideal dipole operating in free space, the cross-over point where the near-field terms and far-field terms are equal in magnitude is $\lambda/2\pi$ [26]. In general, the region around an antenna can be broken into near-field and far-field regimes based on the size and frequency of the antenna and the cross-over point where the near-field and far-field terms of (1.13) and (1.14) are equal in magnitude. For ESAs, the near-field region can be broken into a reactive near-field and radiative near-field component. The reactive near-field region extends up to the cross-over point at $r = \lambda/2\pi$, while the radiated near-field extends to a distance of one wavelength. Between one to two wavelengths is defined as a transition area between the near and far-field regions, while all distances beyond two wavelengths are considered far-field. However, as will be discussed in Section 3.2, these region definitions do not hold true for antennas comprised of high permittivity piezoelectric materials due to confinement of the near-field components.

The efficiency of an ideal dipole can be calculated from (1.9), where the impedance of an ideal dipole of length L radiating with an electromagnetic wavelength of λ is:

$$X_{ideal\ dipole} = -\frac{120\lambda}{\pi L} ln\left(\frac{L}{2r} - 1\right) \tag{1.17}$$

$$R_{rad}^{ideal\ dipole} = 80\pi^2 \left(\frac{L}{\lambda}\right)^2 \tag{1.18}$$

$$R_{L}^{ideal\ dipole} = \frac{L_{ideal\ dipole}}{\sigma A_{ideal\ dipole}} \tag{1.19}$$

where σ is the conductivity of the ideal dipole and the skin depth is assumed to be large relative to the radius of the dipole which is a reasonable assumption for antennas with a radius less than 1 mm at VLF frequencies. At higher frequencies, the skin depth decreases, resulting in more current confinement near the edge of the conductor and increased resistance. However, at low frequencies, the electrical losses in the antenna are very small relative to the antenna reactance and can thus be ignored.

The efficiency for a copper dipole of length 10 cm and radius 1 cm is shown in Fig. 1.3. The current in the antenna is assumed to be constant such that it can be modeled as an ideal dipole. From Fig. 1.3b, while both mismatch and radiation efficiency decrease with frequency, the mismatch efficiency is the dominant term due to the very large reactance given by (1.17). In order to improve the matching efficiency, a matching network can be used to tune out the antenna reactance. For frequencies below 1 MHz, realistic inductive tuning elements (Q less than a few hundred) are physically large and electrically lossy, with resistive components in the $k\Omega - \mathrm{M}\Omega$ range ($R_{match} = |X_{ESA}|/Q_{inductor}$). For ESAs with a matching network, the ohmic losses in the physical antenna are negligible relative to the case where the copper wire antenna is matched to a 50 Ω source using an inductor with Q of 200 is compared to the unmatched case in Fig. 1.2. The matching efficiency can be improved with multiple matching networks but at the cost of matching bandwidth [27].

Figure 1.3b shows that even with a matching network, for frequencies below 10 MHz, the efficiency of the antenna falls off significantly. In fact, for the antenna shown in Fig. 1.3a, unless the efficiency can be raised above the dashed line defined by the FoM in (1.4), it is more efficient to operate the antenna at frequencies above 1 MHz despite the increased propagation losses.

Significant research has gone into maximizing efficiency in ESAs. In general, ESAs are defined by their ka product, where k is the wavenumber and a represents the radius of the smallest sphere that can enclose the antenna. Typically, ESAs are reported at much higher frequencies (MHz and GHz) and relative sizes ($ka > 0.1$) [28], [29] compared to what would be needed for a portable VLF antenna where $ka < 10^{-4}$. Historically, electrically small antenna research has primarily focused on the lower bound for antenna Q (and thus bandwidth) in the context of the Chu limit. However, for very small antennas where mismatch losses are not negligible, a more meaningful metric for reference is antenna efficiency which governs both communication range and rate [30]. Since both the radiation efficiency and matching efficiency can be well below unity for electrically small antennas, the total efficiency of the antenna system is the key metric. For a given volume defined by a, peak efficiency is achieved by maximizing radiation resistance and tuning out the antenna reactance to improve impedance matching. Within a given volume, radiation resistance is maximized when the effective antenna size is increased by leveraging designs such as folded dipoles [31], helixes [32]–[34] or patterned metal shells [29].

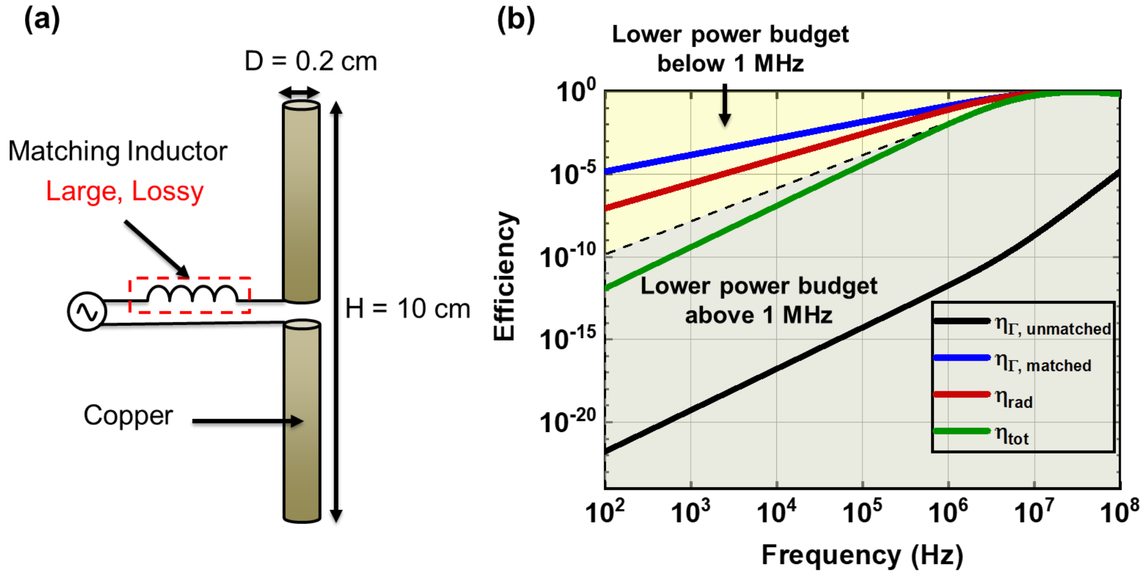

Fig. 1.3. Matching and radiation efficiency for a 10 cm copper wire antenna. (a) Mock-up of a dipole antenna with a lossy matching network to improve mismatch efficiency. (b) Efficiency of the antenna as a function of frequency.

Tuning out the antenna reactance is achieved either using an external matching network [35] or changing the antenna structure to modify the antenna reactance [28]. Incorporating the tuning elements inside the antenna structure, such as with coil antennas [36], [37], provides the advantage of avoiding external circuits by self-resonating the antenna. Optimized, self-resonant electrical antennas have been demonstrated with radiation efficiencies near unity for $0.1 < ka < 1$ [38]–[40] while enabling tunable input impedances to match to driving sources. However, the radiation efficiency of self-resonant antennas falls off as $1/(ka)^4$ for sizes below the critical value [29]:

$$ka_{crit} \sim \left(\frac{2\omega\varepsilon_0}{\sigma}\right)^{\frac{1}{8}} \tag{1.20}$$

where ω is the operation frequency and σ is the metal conductivity.

At VLF frequencies, $ka_{crit} > 0.01$, orders of magnitude larger than ka for a handheld size antenna, and thus the radiation efficiency of self-resonant ESAs decreases as $1/(ka)^4$ for sizes similar to mechanical antennas. While small dipole antennas are generally less efficient than self-resonant antennas when $ka > ka_{crit}$, they exhibit radiation efficiencies that decay as $1/(ka)^2$ [41] when $ka < ka_{crit}$. Including, the necessary lossy matching network to tune out the dipole reactance, small dipole antennas exhibit total efficiencies which scale as $1/(ka)^4$ as well [42]. Therefore, while other geometry-optimized ESAs may yield slightly better efficiencies than an infinitesimal dipole, they are unable to improve the efficiency by the multiple orders of magnitude needed to take advantage of the low propagation losses at VLF frequencies.

1.2 Cross-Domain Antennas

At resonance, antennas exhibit a purely resistive impedance resulting in both a desirable high matching efficiency and low Q. However, the resonant operation requires a physical size near $\lambda/2$ to remove/reduce the reactive component of the antenna. Since the 1940s, the disadvantages of shrinking electrical antennas much below a wavelength have been well understood, and so the impractically of compact VLF antennas has stagnated their development. For physically small or portable VLF transmitters to be viable, a radical paradigm shift is needed to circumvent the limitations of ESAs. If VLF antennas can be reduced to a compact size of tens of cm while still operating at resonance, then mismatch efficiencies can be drastically improved to near unity without sacrificing portability. Logically, such a feat would require several orders of magnitude reduction in phase velocity and consequently decrease in EM wavelength, which is not attainable even with the most advanced high permittivity and permeability materials. Alternatively, cross-cutting into a different physical domain where much slower waves exist can provide a promising solution for resonant size reduction, provided a high energy coupling between the said physical domain and EM domain can be achieved. In fact, such a philosophy has been repeatedly exploited with electromechanical/acoustic devices that leverage acoustic velocities up to 10^5 times slower than the speed of light and can be leveraged to develop compact, resonant acoustic antennas.

For an acoustic resonator to function as an antenna, it must be able to convert an input signal from the electrical domain into the mechanical domain and then back into the electromagnetic domain as radiation. Acoustic devices such as surface acoustic wave delay lines have been used for decades in signal processing applications [43]–[45]. Slower acoustic wave velocities result in shorter resonant wavelengths, enabling physically smaller components relative to electromagnetic counterparts at the same frequency. Acoustic resonant wavelengths can be up to five orders of magnitude smaller than equivalent electromagnetic wavelengths due to the relatively slow speeds of acoustic waves ($v = \sqrt{c/\rho}$):

$$f = \frac{v}{\lambda} = \frac{1}{\lambda}\sqrt{\frac{c}{\rho}} \tag{1.21}$$

where c is the stiffness of the acoustic medium and ρ is the density. Therefore, acoustic antennas operating in the VLF range could enable resonant operation with sizes of ~10 cm compared to 10 km for electrical antennas.

Recently, mechanically resonant antennas have been considered to circumvent the inefficiency of ultra-sub wavelength ESAs required for portable VLF communication. Since radiation occurs due to the acceleration of charge [46], antennas operating via the mechanical movement of charges offer a viable alternative to electrical antennas. Mechanical antennas can generally be considered in terms of their electrical antenna counterparts, where the linear acceleration of unipolar electrical charge, the flipping of aligned dipole charges or the rotation of static dipoles are roughly analogous to monopole, dipole and loop antennas. In the case of either the flipping or rotating dipoles, either electric or magnetic dipoles can be used, while the unipolar case is constrained to electric charges due to the absence of magnetic monopoles. Although work is ongoing to determine the upper limits for radiation efficiency in VLF mechanical antennas, mechanical antennas operating at resonance where the reactive antenna components cancel out offer orders of magnitude improvement in mismatch efficiency compared to ESA counterparts.

To date, numerous approaches for implementing mechanical antennas have been demonstrated. Prototypes based on the rotation of magnetic dipoles [49]–[51] and flipping of magnetic dipoles in magnetostrictive materials [47], [52] have been demonstrated to show promise in surpassing the state-of-the-art (SoA). Investigation of mechanical antennas using electrical charges has primarily been focused on piezoelectric acoustic antennas that produce radiation via flipping internal charges. As first proposed by Mindlin [53], acoustic antennas couple mechanical vibration into electrical radiation through the resonant mechanical displacement of internal electrical charges. More recently, additional studies on the radiation properties of piezoelectric antennas [54], [55] have conducted. Currently, the radiation efficiency ($\xi_{rad} = P_{rad}/P_{del}$) of piezoelectric antennas has yet to surpass equivalent ESAs. However, early prototypes at VLF [48] have been demonstrated to show promise as compact antennas with total efficiencies orders of magnitude greater than ESA's due to the large increase in matching efficiency achieved by operating at resonance. Furthermore, the radiation efficiencies, and thus total efficiency, currently achieved by piezoelectric antennas exhibit the potential for orders of magnitude improvement as material and resonator design is further improved.

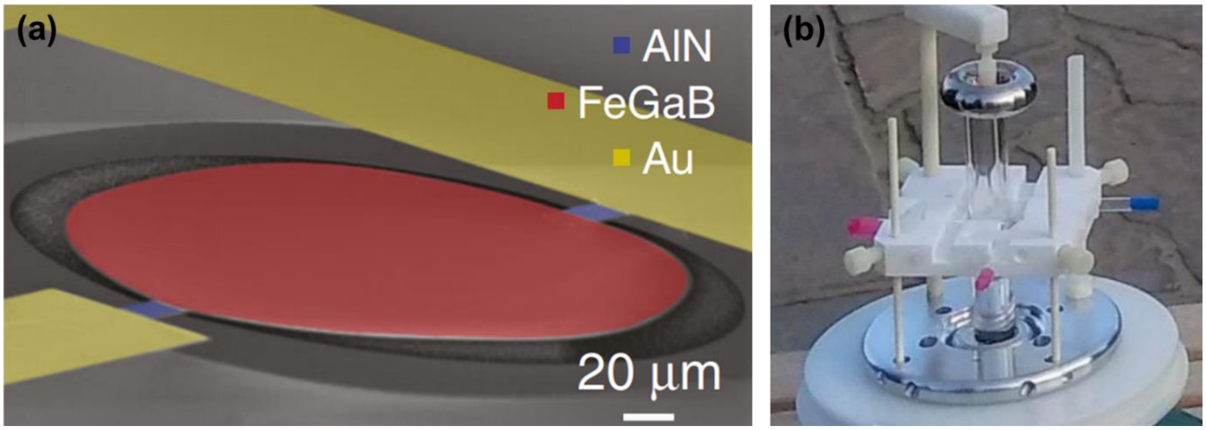

Fig. 1.4. Demonstrated mechanical antennas. (a) Miniaturized magnetoelectric ferromagnetic/piezoelectric thin-film antenna at VHF [47] with more than one order of magnitude improvement in size relative to electrical antenna SoA. (b) Lithium Niobate VLF piezoelectric antenna [48] with 300x the efficiency of comparable SoA electrical antenna.

In this dissertation, piezoelectric alternating dipole antennas are demonstrated using lead zirconate titanate (PZT) as the piezoelectric material. First, a single element PADA comprised of a PZT disk resonating in the radial dilation mode is developed to demonstrate the potential of PADAs as more efficient alternatives to electrical antennas, with a measured efficiency more than 6000x that of an equivalently sized ideal dipole ESA. Although the 6000x improvement in efficiency is significant, it is still well below the expected threshold for PADA efficiency. To demonstrate the potential of further enhancements in efficiency, a short rod PADA comprised of the same PZT material is designed to operate in a more efficient resonant mode. Due to the smaller size of the rod PADA ($V_{disk} \approx 6V_{rod}$) an eight-element rod PADA array is implemented. The demonstrated rod PADA array exhibits a 10x increase in radiation efficiency over the disk PADA and more than a 3x increase in measurement distance.

1.3 The Rest of the Document

This dissertation is arranged as follows. Chapter 1 introduced the challenges of implementing electrically small antennas for low-power, long-distance applications and the need for new cross-domain antennas to surpass the state of the art for portable VLF transmission. Chapter 2 discusses the major methods for implementing cross-domain antennas through the acoustic acceleration of electrical charge and the expected efficiencies and implantation challenges for each method. In particular, antennas formed from alternating dipoles inside of mechanically driven piezoelectric antennas show great promise for exceeding the performance limitations of electrical antennas at VLF frequencies. In Chapter 3, the theory behind piezoelectric alternating dipole antennas (PADA), including the generation or radiating currents and field considerations are discussed. The design of the prototype PADAs is detailed in Chapter 4 while Chapter 5 reports on the measured radiation and modulation performance of the fabricated PADAs. Finally, Chapter 6 discusses future work and the anticipated growth of the field of PADAs.

Chapter 2: Acoustic Antennas

Cross-domain antennas based on flipping dipoles inside of acoustically driven piezoelectric transducers have recently been demonstrated to show promise as compact VLF transmitters with efficiencies more than 1000x greater than similarly sized electrical VLF antennas. However, they represent only one method of implementing antennas based on the acoustic-driven movement of electrical charge. In this chapter, other methods for implementing cross-domain antennas using the acoustically driven acceleration of electrical charge are presented. For each type of antenna, the predicted efficiency values due to material and physical limitations are discussed, as well as implementation challenges.

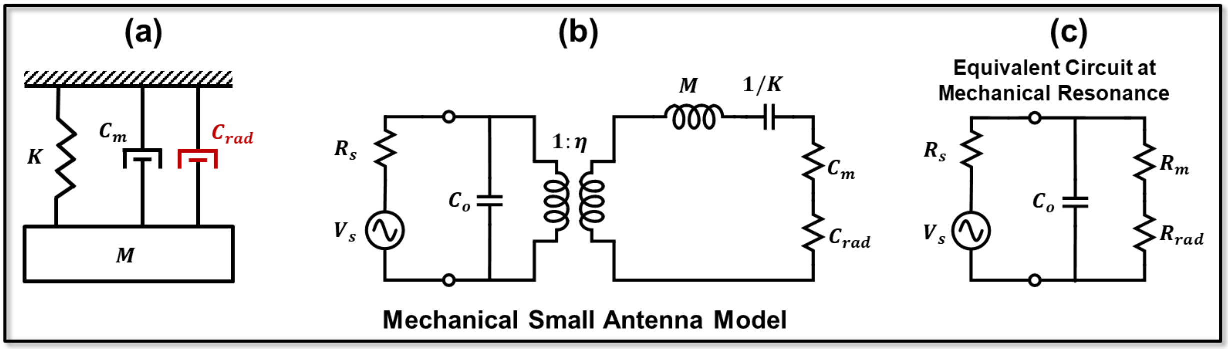

Fig. 2.1. (a) Mechanical antennal model and (b) equivalent electrical circuit model for the mechanical antenna. (c) Equivalent electrical circuit model for the mechanical antenna at mechanical resonance.

One of the primary advantages of mechanical antennas relative to ESAs is that they can be operated at resonance where they exhibit a purely real impedance ($X_A = 0$) even at portable sizes. Mechanical antennas can be simply modeled as a mass (M) on a spring (with stiffness K) with both radiative (C_{rad}) and motional (C_m) damping terms as shown in Fig. 2.1a. The equivalent circuit model for the mechanical antenna is given in Fig. 2.1b, where η represents the electromechanical transformer ratio. At resonance, the mechanical antenna model can be expressed in terms of an electrical equivalent circuit model as shown in Fig. 2.1e, where the motional and radiation resistances R_m and R_{rad} correspond to the motional and radiation damping terms. For resonant operation at VLF frequencies, the parallel branch containing the static capacitance term C_o can be neglected in efficiency calculations since $R_m \gg C_o$. Furthermore, since $R_m \gg R_{rad}$, the mismatch efficiency can be maximized by designing the motional resistance to be equal to the

Table 2.1. Geometric Parameters for Mechanical and Reference Electrical Antennas

Implementation	Mechanical				Reference ESA			
PU	$\boldsymbol{W}$	$\boldsymbol{L}$	$\boldsymbol{A_e}$	$\boldsymbol{T}$	$\boldsymbol{L_{ESA}}$	$\boldsymbol{r_{ESA}}$	$\boldsymbol{R_{match}^{ESA}}$	$\boldsymbol{R_{rad}^{ESA}}$
	1 mm	3 mm	1 mm^2	0.1 mm	3.2 mm	0.16 mm	738 kΩ	90 pΩ
CU	$\boldsymbol{W}$	$\boldsymbol{L}$	$\boldsymbol{A_e}$	$\boldsymbol{T}$	$\boldsymbol{L_{ESA}}$	$\boldsymbol{r_{ESA}}$	$\boldsymbol{R_{match}^{ESA}}$	$\boldsymbol{R_{rad}^{ESA}}$
	5.6 mm	4.6 mm	21.2 mm^2	0.23 mm	7.2 mm	0.36 mm	322 kΩ	472 pΩ
FDE	$\boldsymbol{W}$	$\boldsymbol{L}$	$\boldsymbol{A_{FDE}}$	$\boldsymbol{T}$	$\boldsymbol{L_{ESA}}$	$\boldsymbol{r_{ESA}}$	$\boldsymbol{R_{match}^{ESA}}$	$\boldsymbol{R_{rad}^{ESA}}$
	1.7 mm	3 mm	2.6 mm^2	0.2 mm	3.4 mm	0.17 mm	676 kΩ	107 pΩ
PADA	$\boldsymbol{d_{31}}$	$\boldsymbol{C_{11}^{E}}$	$\boldsymbol{r_{PZT}}$	$\boldsymbol{T}$	$\boldsymbol{L_{ESA}}$	$\boldsymbol{r_{ESA}}$	$\boldsymbol{R_{match}^{ESA}}$	$\boldsymbol{R_{rad}^{ESA}}$
	108 pC/N	152.3 GPa	4 cm	1 cm	8.1 cm	0.41 cm	28 kΩ	63 nΩ

source resistance. Comparing the equivalent circuit models for electrical and mechanical antennas as given by Figs. 1.1 and 2.1c, the total efficiency for a mechanical antenna relative to an ESA employing a lossy matching network is given by:

$$\xi_{tot}^{rel} = \frac{\xi_{tot}^{MA}}{\xi_{tot}^{ESA}} = \frac{R_{rad}^{MA}}{R_{rad}^{ESA}} \frac{(R_{rad}^{ESA} + R_{loss} + R_{match} + R_s)^2}{(R_{rad}^{MA} + R_m + R_s)^2} \tag{2.1}$$

where the superscripts ESA and MA denote electrically small and mechanical antennas respectively. Generally, the radiation and loss resistances are much smaller than the matching, motional and source resistances ($R_{rad}^{ESA}, R_{rad}^{MA}, R_{loss} \ll R_{match}, R_m, R_s$) and thus (2.1) can be rewritten as:

$$\xi_{tot}^{rel} \approx \frac{R_{rad}^{MA}}{R_{rad}^{ESA}} \frac{(R_{match} + R_s)^2}{(R_m + R_s)^2} \tag{2.2}$$

Since R_m can generally be designed to match the desired R_s value, whether that is 50 Ω or otherwise, by tuning the resonator design dimensions, maximum efficiency relative to ESAs is achieved by maximizing R_{rad}^{MA}. In the following text, the formulas for R_m and R_{rad} are presented in order to outline key parameters for achieving maximum efficiency for each mechanical antenna approach.

In all cases, the acoustic antennas are benchmarked to an ideal dipole of comparable size. An ideal dipole is chosen for the reference because:

- Due to the impracticality of ESAs of this size, they are unlikely to be fabricated and thus such optimization provides minimal value.
- The mechanical resonators are presented generally and are also not geometrically optimized.
- Numerous other factors can influence total efficiency, such as increasing ESA Q away from the optimum lower bound to significant increases in efficiency [56].
- Mechanical antennas can achieve multiple orders of magnitude improvements in efficiency over ESAs, so distinguishing between different electrical antennas with similar order of magnitude efficiencies provides little practical value.

Analysis of mechanical antenna efficiency is based around finite element modeling of test cases with effective stiffness and mass resulting in mechanical resonance near 30 kHz. The length of the equivalent ESA dipoles is set as the diameter of the smallest sphere fully enclosing the mechanical antenna, while the radius is set to be 1/20th of that length. The key geometric parameters for the mechanical antennas and the corresponding electric dipoles are presented in Table 2.1. For all analyses presented here, the maximum length/width dimensions of the mechanical resonators are assumed to be constant such that the reference ESA efficiency is fixed for each type of mechanical antenna.

2.1 Radiation from Moving Charge

Electromagnetic radiation occurs due to the perturbation of electromagnetic fields caused by the acceleration of charge. For a constant velocity charge as shown in Fig. 2.2, the resulting electric field is constant and extends radially away from the charge. Sudden acceleration of the charge results in a distortion of the radial field lines near the charge relative to the existing field lines, and sinusoidal changes in acceleration lead to disturbances in the form of waves propagating away from the charge. General radiation from a moving charge was independently developed by Alfred-Marie Liènard in 1898 and Emil Wiechert in 1900. For a charge q accelerating linearly, the magnitude of the radiated magnetic field B is:

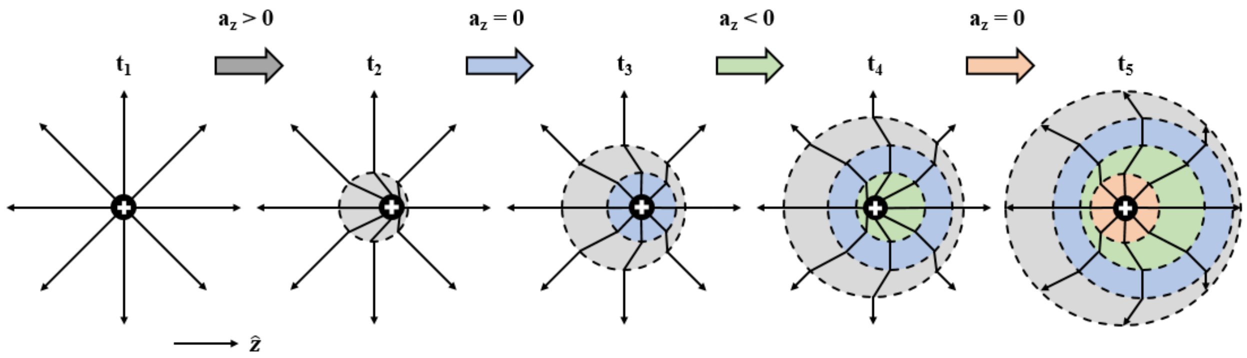

Fig. 2.2. Conceptualization of radiation from an accelerating charge. At charge at constant velocity exhibits field lines extending radially away from it. If the charge is then accelerated from time t1 to time t2 the field lines are distorted during the duration of the acceleration due to the changing speed of the charge. Returning to constant velocity results in the field lines extending radially again. The radius of the circle represents the distance an electromagnetic wave would travel during Δt = ti+1 – ti. For non-relativistic charge, the circles would be nearly concentric but are exaggerated here for emphasis. Repeated acceleration and deceleration of charge leads to electromagnetic waves radiating away from the source, with the largest amplitude perpendicular to the acceleration and no radiation parallel to the acceleration.

$$|B| = \frac{q}{4\pi\varepsilon_0 r c^2}\left|\hat{r} \times \frac{\dot{v}}{c}\right| = \frac{q\dot{v}}{4\pi\varepsilon_0 r c^3} sin(\theta) \tag{2.3}$$

where ε_0 is the permittivity of free space, r is the distance between the charge and the measurement point, $\dot{v}$ is the acceleration of the charge and is the angle θ is defined the same as in Fig. 2.3. The full expression for the magnetic field produced by an accelerating charge includes terms that depend on both velocity and acceleration. However, the velocity term is proportional to R^{-2} and is therefore negligible far from the accelerating charge ($R \gg \lambda$) [46]. To achieve maximum large far-field radiation, both a large amount of charge and fast acceleration (frequency or displacement) are desired.

For accelerating charge to radiate as desired for an antenna, it is necessary to create a time-varying acceleration which will result in the radiation of electromagnetic waves. For electrical antennas, the time-varying charge acceleration is driven by the application of an AC current supplied to the antenna terminals. Mechanical antennas can reproduce the AC current of electrical antennas by mechanically moving discreet charges via a time-varying sinusoidal displacement to create an effective electrical current where $qa \propto I_{eff}$. This charge movement can be accomplished by means of a resonant micro-electro-mechanical system (MEMS) loaded with charge. From (2.1), to achieve large far-field radiation, MEMS antennas should seek to maximize both the amount of charge and the rate at which the charge is accelerated. For resonant systems, acceleration is proportional to the product of the peak displacement of the charge and the resonant frequency squared ($a \approx d_{pk}\omega^2$).

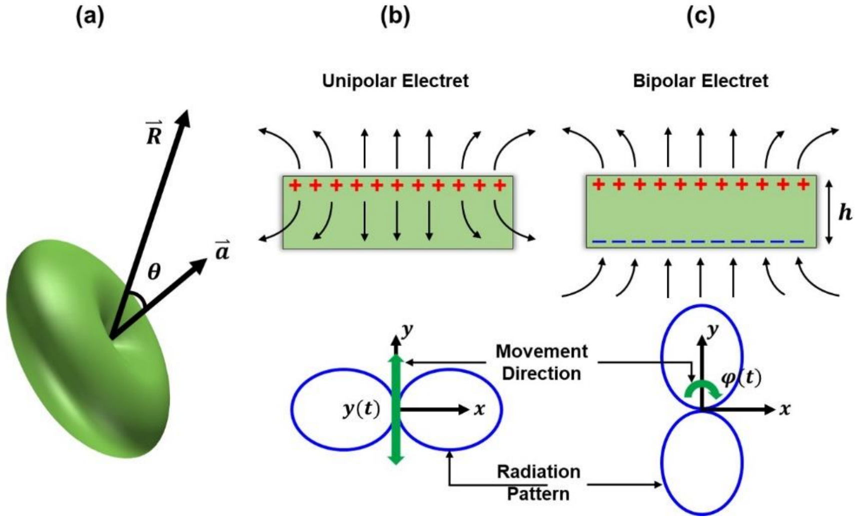

Fig. 2.3. Accelerating charge radiation pattern and implementation. (a) 3D pattern of an accelerating non-relativistic charge with maximum radiation generated perpendicular to acceleration direction. (b) Unipolar and (c) bipolar electrets. Movement directions are depicted by green arrows resulting in omni-directional far-field radiation patterns shown in blue (depicted as 2D cross-section).

The addition of charge to resonating micromechanical structures can be implemented through the application of an electret thin film, and for maximum radiation, the electret should be added to the portion of the resonator experiencing peak displacement. Electrets can be thought of as the electrical equivalent to magnets and consist of materials loaded with electrical charges. Unlike magnets that have north and south poles and stable magnetization, electrets are quasi-permanent devices that carry either unipolar or bipolar electric charges for a specific amount of time before the amount of charge starts to decay. The decay occurs due to the neutralization over time of the electret charges as the fields they produce attract opposing charges from both inside and outside of the electret. Therefore, while the intrinsic charge density of electrets is maintained, the effective charge density presented by the electret is diminished due to the accumulation of neutralizing charges on its surface.

As shown in Fig. 2.3b and 2.3c, two types of electrets can be implemented. First, monopole or unipolar electrets, in which an insulating material is charged with monopole charges using, for example, corona discharge or ion implantation [57]. Unipolar electrets can generally be separated into two categories: organic polymer electrets (e.g. PTFE [58] and Cytop [59]) and inorganic electrets (e.g. SiO_2 [60]) with inorganic SiO_2 electrets typically offering the highest charge densities. Second, dipole or bipolar electrets, in which a ferroelectric material is polarized to have an internal quasi-permanent dipole [61]. An electret can be evaluated based on two main performance metrics: the charge density that can be attained (σ), and the charge retention or the decay rate of the attained charge.

Similarly, to electrical antennas where the routing of electrical currents or energy through different structures (e.g. dipole, loop, horn, etc.) can result in distinct radiation properties, multiple methods of mechanically driving charge for radiation could provide unique antenna opportunities. For unipolar charges, such as ions implanted in an electret, either linear or rotational motion can be used to accelerate the charges. In contrast, dipole charge pairs, which can be achieved by polling a ferroelectric material, will not radiate if subjected to linear acceleration. The positive and negative charges comprising the dipole produce equal but opposite radiation when subjected to the same linear acceleration, resulting in no net radiation. However, radiation from dipole charges can be achieved via rotational acceleration, where components of the radiation from the opposing charges can add constructively. Additionally, flipping of dipoles such that the polarity is switched as a function time will also produce radiation as the opposing charges experience opposite accelerations and thus add constructively.

2.2 Antennas Based on Linearly Accelerated Unipolar Charge

Mechanical antennas leveraging radiation from linearly moving unipolar charges can be implemented by coupling a charged electret with MEMS resonators where the operating frequency of the antenna is determined by the resonant frequency of the MEMS. Once the operating frequency is determined, the resonator is designed to maximize both the electret charge (q) and the maximum displacement of the electret charge (d_{pk}) to produce the largest radiation as defined in (2.3). While many resonator design components contribute to the qd_{pk} product, it is fundamentally limited by the maximum displacement that can be achieved prior to the resonator breaking or entering the nonlinear region of operation and the maximum amount of charge that can be stored in the electret and moved. Many MEMS actuation mechanisms can be implemented to move the electrical charges including piezoelectric, capacitive, thermal, and magnetic actuators; however,

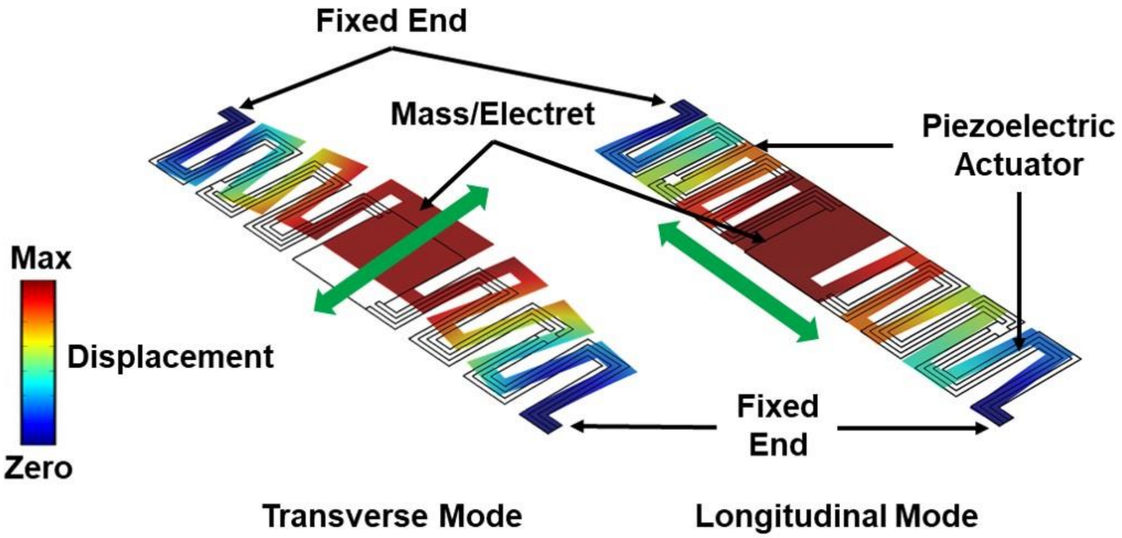

Fig. 2.4. Piezoelectric actuation mechanism for linearly moving charges. Two folded beams/springs made of a piezoelectric material with top electrodes are used to move an electret/mass either in a transversal or longitudinal direction.

the analysis herein is focused on piezoelectric and capacitive actuators as the most commonly used actuation mechanisms.

2.2.1 Piezoelectric Actuation

Piezoelectric materials couple the electrical and mechanical domains leading to the reversible phenomena of piezoelectricity. Through the piezoelectric effect, applying an electric field across a material generates mechanical stress/strain that deforms the material. This deformation can be used to move electrets implemented on a suspended structure which is mechanically driven by a piezoelectric actuator. Figure 2.4 shows an example of a piezoelectric resonator where a proof mass, acting also as an electret loaded with unipolar charges, is tethered at two fixed ends with two folded beam piezoelectric actuators. Upon actuation, the electret undergoes in-plane movement which generates EM radiation. The dimensions of the folded beam and the mass/electret can be tailored to achieve a specific resonance frequency within a certain volume. A piezoelectric resonator can be modeled as a one-port resonator using the MBVD model [62], [63] in Fig. 2.1, where at resonance the input impedance of the resonator is comprised of a motional resistance R_m in series with a radiation resistance R_{rad}. R_m can be expressed as follows:

$$R_m = \frac{\pi^2}{8\omega_r C_o k_t^2 Q} \tag{2.4}$$

where ω_r is the angular resonant frequency, C_o is the capacitance at the input port of the piezoelectric resonator, k_t^2 is the electromechanical coupling coefficient, and Q is the mechanical quality factor of the resonator. Moreover, $R_{rad} = C_{rad}/\eta^2$ where C_{rad}, the radiation damping coefficient, and η, the electromechanical transformer ratio, can be formulated as [55]:

$$C_{rad} = 80\pi^2 \left(\frac{\sigma A}{\lambda}\right)^2 \tag{2.5}$$

$$\eta^2 = \frac{8}{\pi^2} K C_o k_t^2 \tag{2.6}$$

$$R_{rad} = \frac{10\pi^4 \left(\frac{\sigma A}{\lambda}\right)^2}{K C_o k_t^2} \tag{2.7}$$

where σ is the surface charge density, A is the electret area ($q = \sigma A$), λ is the electrical wavelength, and K is the equivalent spring constant of the piezoelectric resonator.

The efficiency of a piezoelectric unipolar antenna relative to a similarly sized ESA can be calculated by substituting (2.4) and (2.7) into (2.3). The relative efficiency as a function of different design parameters is shown in Fig. 2.5. In Fig. 2.5a, the relative efficiency is shown as a function of charge density and mechanical Q, under the assumption that mechanical resonator design is fixed such that K, C_o, and k_t^2 are constant. The black star gives the relative efficiency of an antenna with AlN actuators as shown in Fig. 2.4. The properties of the reference resonator are shown in the inset in Fig. 2.5a with the dimensions listed in Table 2.1, and the shaded region demonstrates the effect of scaling Q by an order of magnitude. Since mechanical efficiency is proportional to charge density squared, peak efficiency is achieved by maximizing the amount of charge on the smallest possible area to maximize the radiation without increasing the size of the mechanical antenna. The charge density is limited by the breakdown electric field that the mechanical antenna can sustain. Above that charge density limit, the resulting electric field will break down the surroundings and charges start escaping from the electret by arcing to the nearest ground or opposite polarity charges.

For the case of a piezoelectric unipolar antenna, breakdown can occur both in the electret and in the surrounding medium. While dielectric electret materials such as SiO_2 have been demonstrated to sustain charge densities as high as 30 mC/m^2 [57], [64], [65] due to a breakdown field strength

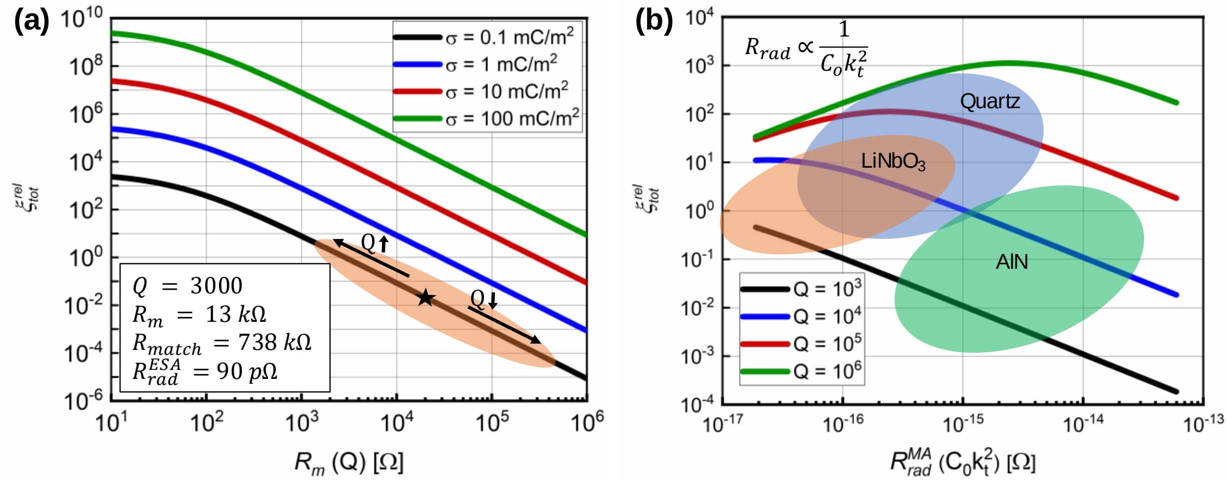

Fig. 2.5. Design space for unipolar piezoelectric antennas. (a) Relative efficiency of piezoelectric unipolar antenna like the one in Fig. 2.4 relative to a similarly sized ESA as a function of the motional resistance for different values of charge density. (b) Relative efficiency of piezoelectric unipolar antenna like the one in Fig. 2.4 relative to a similarly sized ESA as a function of radiation resistance for different values of Q. Both radiation and motional resistance are varied as a function of $C_o k_t^2$ to represent a range of different, similarly sized, designs in common MEMS materials. Simulations are based on a 3 mm long AlN resonator with an electret area of 1 mm^2 and charge density of 0.1 mC/m^2 referenced to a 3.5 mm ESA. Parameters such as C_o, k_t^2, Q, K and M are varied for the ALN design to account for a range of designs in different materials.

of 100 MV/m, the breakdown field strength of air surrounding the electret is 3 MV/m [66]. The maximum electret charge is capped by the lowest breakdown limit in the system. For an electret-based antenna operating in air, this limits the maximum charge density to < 1 mC/m^2, with the exact value depending on electret material, geometry and charge distribution. Packaging schemes that utilize insulating dielectric gases such as SF$_6$ or greater than atmospheric pressure [67] can enable greater charge densities by increasing the breakdown field strength of the surroundings. However, such packaging would result in greater cost and potentially diminished Q due to increased air damping [68], [69]. A tradeoff, therefore, exists between using vacuum packaging to achieve higher Q but lower charge density [70] or packaging with insulating gas for greater charge density but lower Q. This tradeoff is shown generally in Fig. 2.5a but will vary slightly depending on resonator and electret materials and design.

The mechanical quality factor Q is an essential parameter in efficiency calculations as shown in Fig. 2.5a and 2.5b. Large quality factors enhance the displacement of the electret at resonance, enabling greater radiation and diminished motional resistance. Piezoelectric resonators have a wide range of quality factors depending on the resonance frequency, vibration mode, material type, temperature range, and fabrication process. Quality factors can range from a few hundreds to tens of millions [71]–[74] depending on resonator material and design. The relative efficiency of a unipolar piezoelectric antenna as a function of resonator material is shown in Fig. 2.5b for some of the common piezoelectric resonator materials. Relative efficiency is plotted as a function of $C_o k_t^2$ for different values of Q to account for different resonator materials [63], [75]–[77] and designs and the electret is assumed to have an area of 1 mm × 1 mm and charge density of 0.1 mC/m^2. It is assumed that the resonant frequency is maintained for various materials, electrode configurations, etc. by independently scaling the thickness, and thus mass, of the resonator. The efficiency of the unipolar piezoelectric antenna for all material choices can be increased by improving the electret charge, either by increasing the electret area or charge density, since the resonator properties such as C_o, k_t^2 and Q are generally independent of the electret charge. Therefore, it is important to maximize the size of the electret within the spherical volume bounding both the piezoelectric unipolar antenna and the equivalent dipole in order to increase relative efficiency.

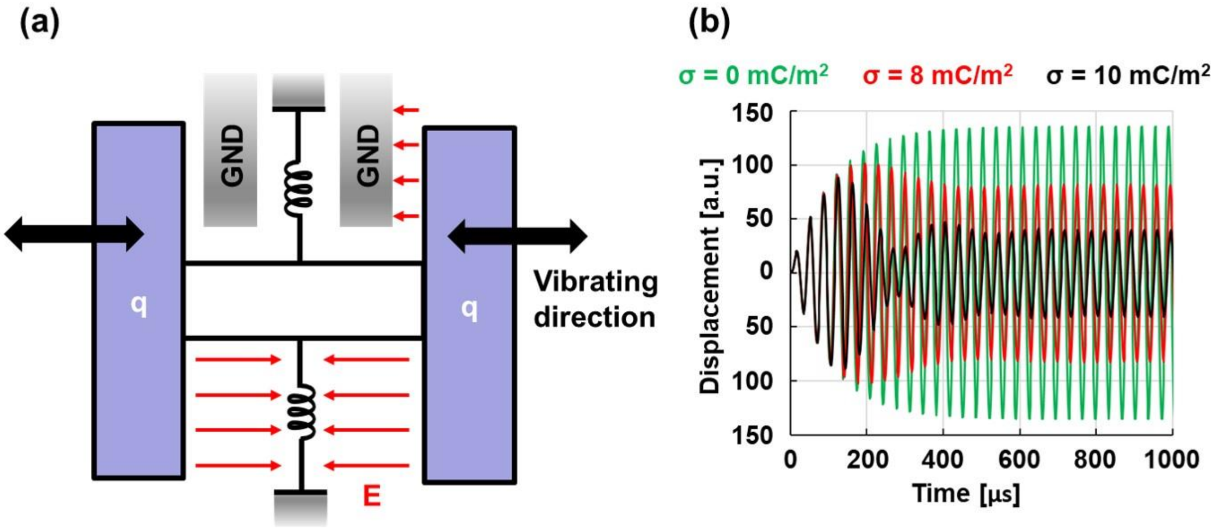

Fig. 2.6. Effect of increasing electret area. (a) Mock-up of an example electret configuration to increase total charge and effective charge density. The static fields produced by the electret induce structural deformation and internal feedback due to the stress generated in the piezoelectric actuators by the static field. (b) The tradeoff between increased charge density and diminished electret displacement due to the feedback phenomena. Adding grounds between the actuators and electrets can limit the feedback but results in a decrease in effective charge density due to pull-in considerations.

A mock-up for an electret configuration with a greater electret footprint, and thus relative efficiency since the maximum resonator dimensions are maintained, compared to the design in Fig. 2.4 is shown in Fig. 2.6a. The resonator effective spring constant is scaled with the increased mass from the larger electret to maintain the desired frequency. However, while increasing the electret footprint can result in greater effective volumetric charge density (inside the bounding sphere) and thus greater radiation efficiency, interference between the large static fields generated by the bound charges and the piezoelectric actuators caps the maximum volumetric charge density that can be achieved. The electrostatic field interferes with the driving electric field applied inside the piezoelectric material between the metallic electrodes, resulting in phenomena such as internal feedback which limit the performance of the mechanical antenna. The feedback effect is demonstrated in Fig. 2.6b, where for constant input power, the mechanical displacement, and thus radiation efficiency, is diminished due to feedback from the electrostatic fields produced by various charge densities acting on the piezoelectric transducers. The exact tradeoff between increased efficiency due to greater electret charge vs. diminished radiation efficiency from feedback effects is dependent on the electret implementation. One way to limit the feedback effect is to surround the actuator with grounds to shield the interfering electrostatic field as shown in Fig. 5a. However, this complicates the fabrication process and lowers the volumetric charge density of the mechanical antenna as additional spacing between the grounds and electret must be added to avoid pull-in.

2.2.2 Capacitive Actuation

In addition to the piezoelectricity, capacitive transduction is widely used in MEMS devices. Such a transduction mechanism does not require a functional material and can produce significant electrostatic forces at micro-scale. For a one-dimensional case, the electrostatic force F_e is determined by the derivative of the electrical potential energy U_e:

$$F_e = -\frac{\partial U_e}{\partial x} = -\frac{\partial}{\partial x}\left(\frac{1}{2} q V_S\right) = -\frac{\partial}{\partial x}\left(\frac{1}{2} C_d V_S^2\right) \tag{2.8}$$

where $q = C_d V_S$ is the amount of charge carried by the electret, V_S is the surface potential referenced to ground, and the C_d is the equivalent capacitance formed by the electret and the ground, respectively. The unipolar charge loaded on the electret provides a potential for generating large electrostatic force ($F_e \propto q$). However, unlike the traditional electrostatic actuators [78], charge-biased electrets can only be actuated under a specific electrode arrangement using a time-varying electrostatic force.

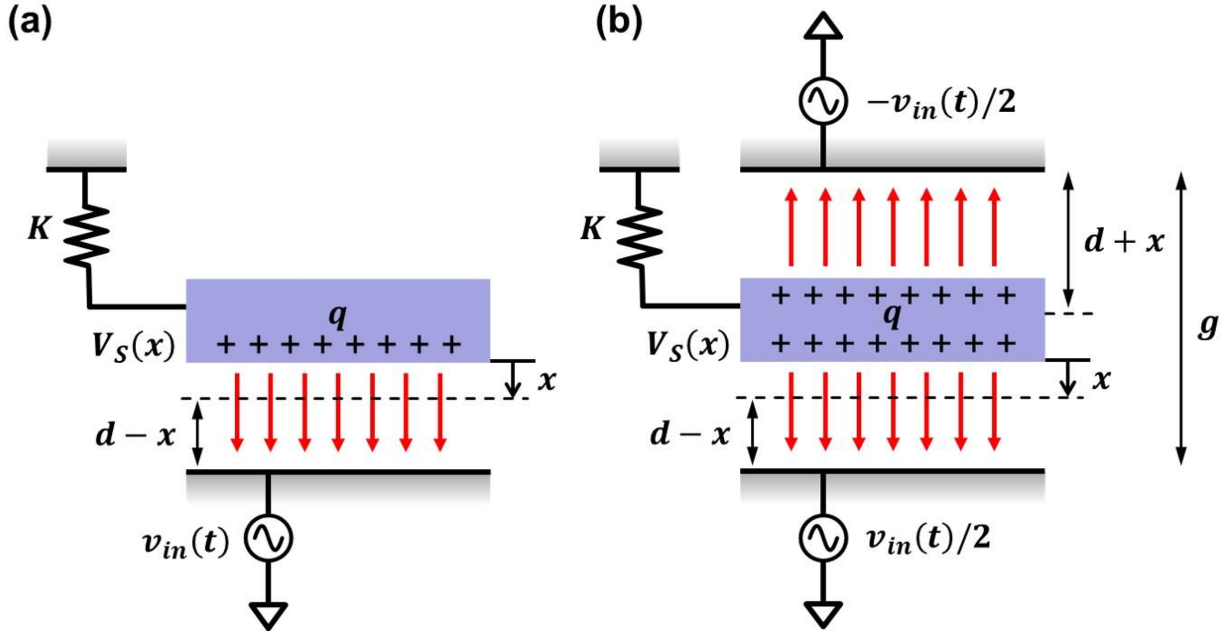

Fig. 2.7. Capacitive actuation mechanism for linearly moving charges. (a) Typical capacitive actuation technique for fixed voltage case which does not apply to electrets with fixed charges. (b) Differential capacitive actuation used to drive an electret into linear motion.

Consider the two parallel-electrode arrangements illustrated in Fig. 2.7 for the charge-biased electret with mass M suspended by a lumped spring K such that the natural frequency of the system is $\omega_r = \sqrt{K/m}$. Since q is a constant, for a single capacitor system in Fig. 2.7a, the surface potential is a function of displacement q, given by:

$$V_S(x) = \frac{d-x}{d} V_{S0} \tag{2.9}$$

where V_{S0} is the surface potential at $x = 0$ and d is the initial gap spacing. Then the actuation force under a time-varying input signal $v_{in}(t) = V_{in}\sin(\omega t)$ can be solved as follows:

$$F_{e,DC} \approx \frac{1}{2}\frac{q}{d}V_{s0}, \quad F_{e,\omega} \approx 0 \tag{2.10}$$

where $F_{e,DC}$ and $F_{e,\omega}$ denote the electrostatic force at dc and frequency ω, respectively. Unlike the voltage-biased electrostatic actuators in the literature [79], there will be no pull-in instability effect at DC since the force is proportional to q (assuming the fringing field is negligible). However, such a single capacitor system *cannot* be actuated by the time-varying signal for the same reason. To overcome this limitation, a dual-capacitor system (Fig. 2.6b) with differential actuation can be utilized, where the time-varying electrostatic force for the dual-capacitor system can be found as:

$$F_{e,Diff,\omega} = \frac{q}{g} V_{in} \tag{2.11}$$

where $F_{e,Diff,\omega}$ denotes the differential electrostatic force at ω and $g = 2d$.

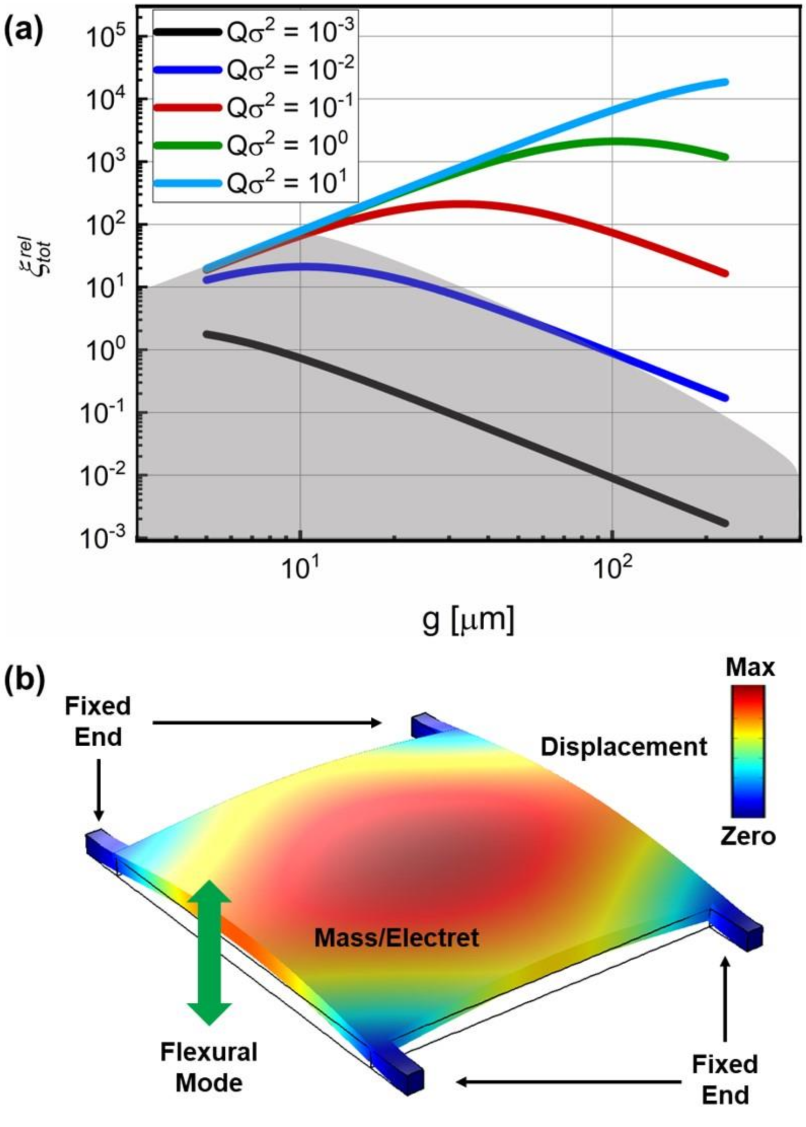

Fig. 2.8. Design space for capacitively actuated mechanical antennas. (a) Relative efficiency of silicon capacitive antenna compared to ESA as a function of gap size. (b) Reference antenna for the relative efficiency calculation with electret area of 4.6 mm × 4.6 mm.

The MBVD model for the electrically-driven mechanical antenna can be expressed as follows [55]:

$$R_m = \frac{k}{\omega_r Q}\left(\frac{g}{\sigma A}\right)^2, \quad C_{rad} = 80\pi^2\left(\frac{\sigma A}{\lambda}\right)^2, \eta^2 = \left(\frac{\sigma A}{g}\right)^2 \tag{2.12}$$

where $R_{rad} = C_{rad}/\eta^2 = 80\pi^2(g/\lambda)^2$. The MBVD parameters are similar to the piezoelectric actuation discussed in the previous section. Unlike the piezoelectric case demonstrated in Fig. 2.4, where relatively long (compared to the electret-loaded proof mass) actuators are needed to achieve large displacements, the capacitively driven antenna can employ a much larger electret footprint relative to total antenna size. An example of a capacitively actuated antenna is shown in Fig. 2.8b. The electret is driven in a flexural resonance mode back and forth between the two grounds used to excite it with the differential drive depicted in Fig. 2.7. Note that the maximum charge density is still limited by the electret material for the electrostatic case. The differential electrostatic driving scheme solves the feedback problem from the previous approach caused by the interference between piezoelectric material and strong electrical field from electret since the electret can be compactly sealed by the electrodes. However, to avoid the electrical breakdown in small actuation gaps, the systems must be properly packaged in high vacuum.

Studies have shown that at low pressure ($< 10^{-4}$ Pa), small gap sizes (< 10 µm) can increase the breakdown field limit by orders of magnitude [80]. The increased breakdown limit could enable charge densities significantly larger than 1 mC/m^2. However, as shown in Fig. 2.8a, for small gap sizes there is a negligible increase in relative efficiency. The relative efficiency of a capacitive unipolar antenna is shown in Fig. 2.8a as a function of gap size. The anticipated achievable design space for a VLF capacitive antenna similar to the one shown in Fig. 2.7b is shaded in Fig. 2.7a where the total efficiency is limited by gap size. From (2.2) and (2.12), relative efficiency is maximized with a large gap size, provided that $R_m = R_s$ and the gap size does not become so large that fringing fields can no longer be neglected**.** For a resonant system with fixed stiffness and mass, impedance matching can be achieved with larger gap sizes by increasing Q and σ**.** Gap design for maximum efficiency must be balanced between a large gap size for increased radiation efficiency vs. a small gap size to increase achievable charge density in vacuum to match the source impedance.

2.3 Antennas Based on Rotating Dipolar Charges

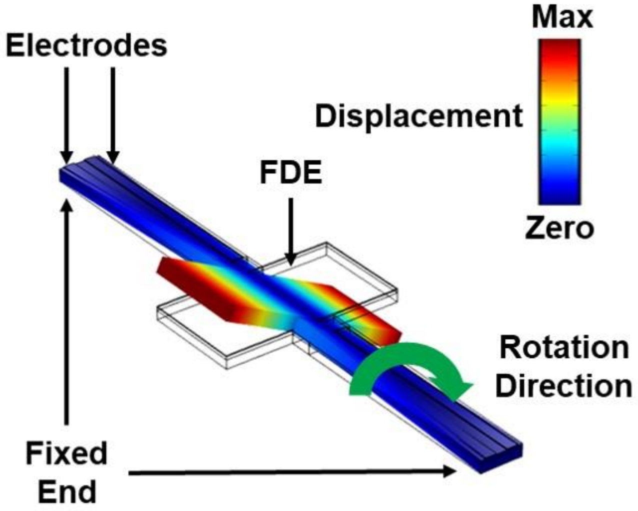

Fig. 2.9. Piezoelectric actuation mechanism for rotating bipolar charges. A piezoelectric material poled and tethered to the fixed ends by two composite beams made of a piezoelectric material on top of a passive material (bimorph) that generates the rotational movement upon the excitation of the piezoelectric material [81].

Dipole electrets can only radiate with rotational motion because, in linear translational motion, both positive and negative charges have the same acceleration magnitude and direction, consequently canceling the net radiation. A dipole electret undergoing rotational motion while accelerating/decelerating, as shown in Fig. 2.9, can radiate EM energy and the resulting peak magnetic field in the case of sinusoidal motion can be formulated as:

$$|B| \approx \frac{q}{4\pi\varepsilon_o}\frac{\omega^2 h\varphi_{pk}}{c^3 R} \tag{2.13}$$

where h is the thickness of the dipole electret and φ_{pk} is the peak deflection angle. Equation (2.13) is an approximation that is only valid if $\varphi_{pk} < 10^o$. As previously shown in the unipolar electrets, the charge density is the most essential parameter to determine the efficiency of mechanically driven antennas. Piezoelectric actuation can be used to generate such a torsional/rotational motion [81], where R_m and R_{rad} can be calculated similar to the case of linearly moving charges using (2.5-2.7). The only difference is that stiffness (K) is defined as the ratio between the torsional stiffness and the thickness of the actuator.

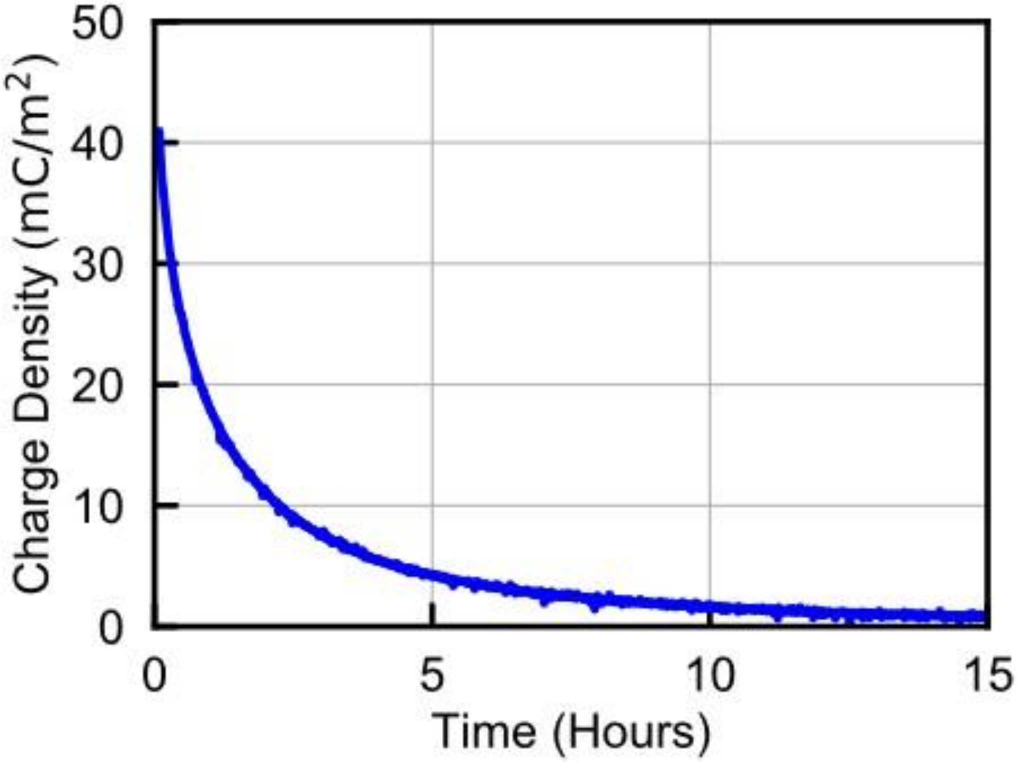

Fig. 2.10. Measured decay of the measured surface charge density of a PZT FDE over time.

Dipole electrets can be made of ferroelectric materials by utilizing the polarization hysteresis behavior. A ferroelectric material can have a remnant polarization if an electric field that exceeds the coercive field is applied to it for a specific amount of time and then removed. This process will result in the alignment of all randomly directed dipoles inside the material in the same direction as the applied electric field. The preparation of FDEs requires the application of a very high voltage in the direction of polarization which is one of the complications to implementing FDEs [82]. FDEs can theoretically possess a very high charge density (polarization) compared with unipolar electrets [83]. For example, PZT FDEs can reach up to 300 mC/m^2 of remnant polarization [61] and $LiNbO_3$ FDE can reach 700 mC/m^2 [84], in comparison to 30 mC/m^2 for unipolar electrets. Another advantage of FDEs, in addition to the much larger charge density, is the tight confinement of electrostatic fields arising from the fact that both positive and negative charges exist on the electret. Thus, in comparison with unipolar electrets, the dipole configuration results in less interference between the electrostatic field and the driving field for the same charge density.

Unfortunately, the FDE concept is not yet well understood. Existing FDEs have charge densities much lower than the theoretically predicted values with very short retention time in the range of

1-30 hours depending on the FDE type [61], [85] as shown in Fig. 2.10 for a PZT FDE. The diminished charge density and retention is likely due to the natural tendency for systems to tend toward higher states of entropy. Since the confinement of charge results in a decrease in entropy, the natural response of the system is to increase entropy by mitigating the large electric field produced by the electret charge [86]. Although the exact reason for the diminished charge density and retention time is still under investigations, possible causes include the interaction of gas ions with the surface of the FDE resulting in the exchange of charge or the migration of charge within the FDE itself due to the large electric force and domain wall motion due to the defect dipole pinning [61].

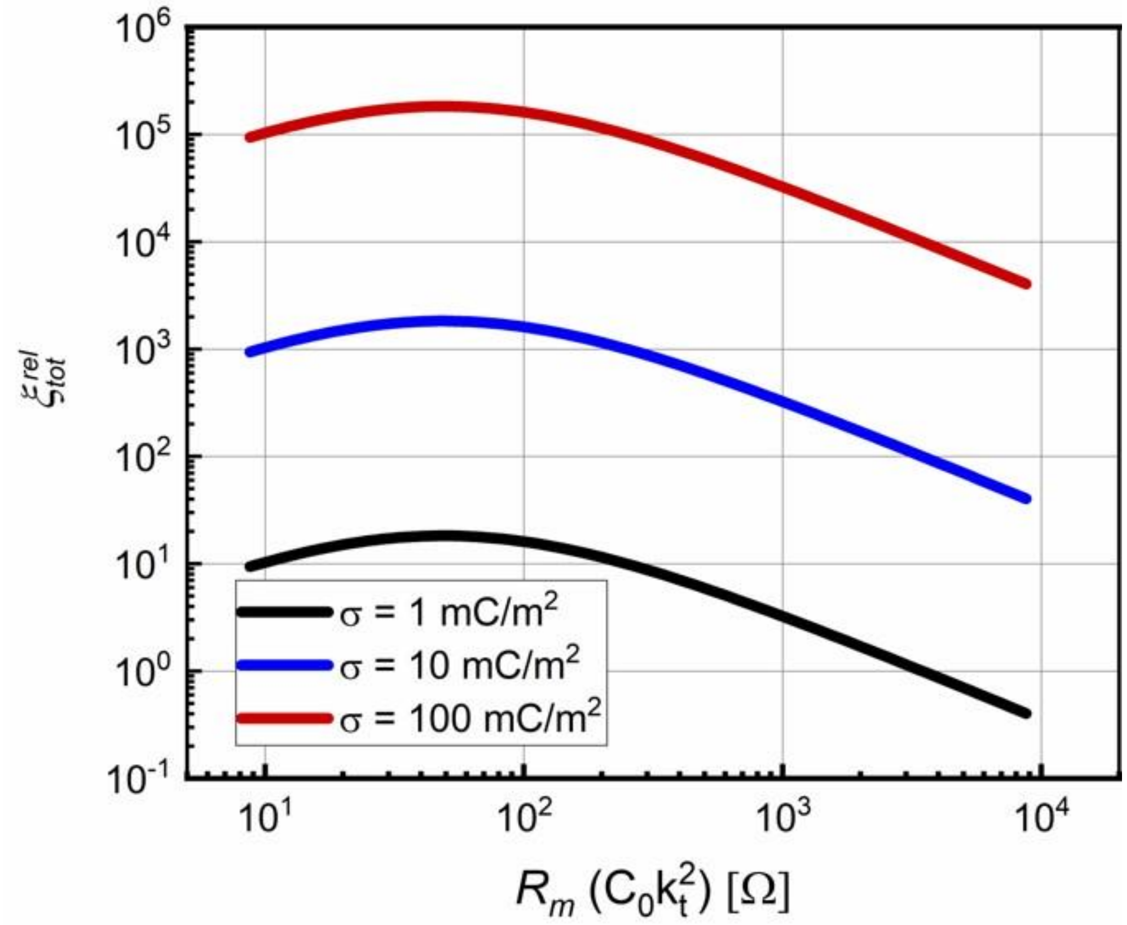

Fig. 2.11. Relative efficiency of a torsionally actuated FDE antenna compared to ESA as a function of motional resistance with Q = 10,000 and $C_0k_t^2$ swept to account for various resonator materials and designs.

As shown in Fig. 2.11, the peak efficiency attainable by FDE antennas surpasses unipolar mechanical antennas by orders of magnitude. However, due to the decay of charge density over time, and therefore the radiation that the FDE can generate, FDE antenna efficiencies can decrease by more than 1000x over the course of a single day, as shown by Fig. 2.11 in conjunction with Fig. 2.10. Viability of FDE antennas, therefore, requires both improved charge retention as well daily, or even hourly, repolarization before use. However, enabling repolarization of the ferroelectric dipole would require additional packaging complexity and power consumption not related to radiation which could be prohibitive for applications where long operating lifetimes are required.

2.4 Antennas Based on Linearly Flipping Dipolar Charges

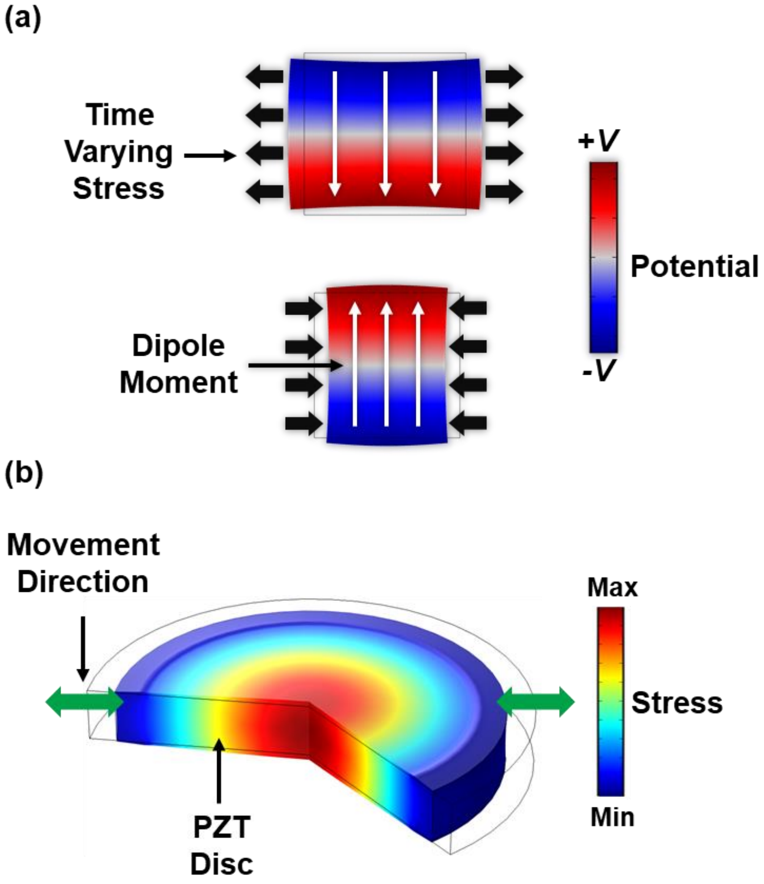

Fig. 2.12. Alternating dipole mechanical antenna. (a) Conceptual diagram of the alternating dipole. Time-varying stress induced by the driving signal results in a time-varying dipole moment which acts as an effective linear current element. (b) PZT disk resonating in the radial breathing mode to accomplish the mechanical antenna realization [87].

The charge density of electrets is an immense obstacle against accomplishing practical and efficient mechanically driven antennas. As previously discussed, implementing an electret with a meaningful charge density, whether it is unipolar or bipolar, is very challenging. Instead, the dipole movement can be attained by applying time-varying stress on a piezoelectric material. The resulting deformation of the non-centrosymmetric crystal leads to a change in the magnitude of the internal polarization, generating a time-varying dipole moment. Although a high charge density is still required for an efficient mechanical antenna, this charge density exists only dynamically during the application of mechanical stress. Otherwise, the material is neutral, which can be thought of as a dynamic electret. The concept of an alternating dipole resonator is depicted in Fig. 2.12.

Alternating dipoles inside a piezoelectric material avoids static electrets challenges. First, the radiation relies on the dynamic movement of bound charges inside the piezoelectric material, instead of unbounded static charges, therefore circumventing the retention time limitation. Moreover, there is no electrostatic field which mitigates the electric field interference problem. Second, the required dipole moment for an efficient mechanical antenna can be easily achieved by careful selection of the piezoelectric material and its dimensions. Using the piezoelectric constitutive equations, which will be discussed in depth in Chapter 3, the charge density resulting from an applied stress field on the surface of a piezoelectric material can be expressed as [55]:

$$\sigma = dT = dC^E S \tag{2.14}$$

where d is the piezoelectric coupling matrix for the strain-charge formulation, T is the applied stress, C^E is the stiffness at constant electric field and S is the resulting strain. R_m and η^2 for alternating dipoles can be calculated from Equations (2.5) and (2.7), respectively. The radiation damping coefficient C_{rad} can be expressed as follows:

$$C_{rad} = 80\pi^2 \left(\frac{2d_{ij}C_{jj}^E A}{\lambda}\right)^2 \tag{2.15}$$

where d_{ij} is the piezoelectric coupling coefficient in the strain-charge form with the stress applied in the j-direction and the dipole is in the i-direction, and C_{jj}^E is the mechanical stiffness at a constant electric field. Combining (2.5), (2.7), and (2.15) the radiation efficiency of a PADA can be written [55]:

$$\xi_{rad}^{ADMIRE} = \frac{P_{rad}}{P_{del}} = \frac{P_{rad}}{P_{rad} + P_{damp}} = \frac{C_{rad}}{C_{rad} + C_m} \approx \frac{16T\eta_0 d^2 C^E A\omega Q}{3\pi\lambda^2} \propto d^2 C^E V Q \omega^3 \tag{2.16}$$

where

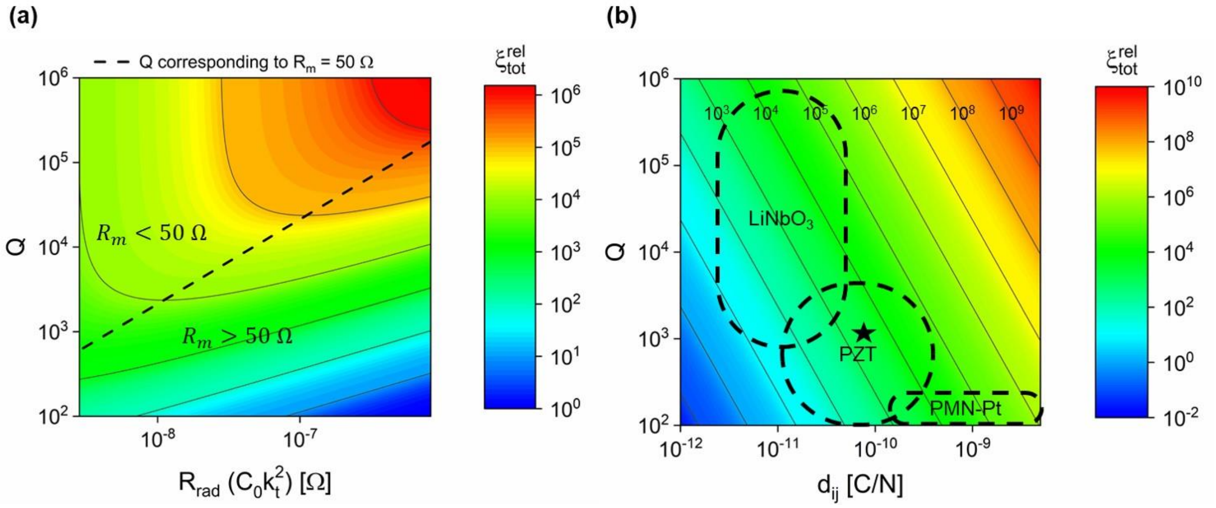

Fig. 2.13. Design space for PADAs. (a) Relative efficiency of a piezoelectric flipping dipole antenna similar to the one reported in [87] relative to a similarly sized ESA with length L = 8.1 cm as a function of the radiation resistance with d = 100 pC/N and $C_o k_t^2$ varied to simulate a variety of resonator materials and designs. (b) Relative efficiency of a piezoelectric flipping dipole antenna as a function of Q and d. Parameters such as C_o, k_t^2 and C_{jj}^E varied to account for a range of designs in different materials.

$$C_m = \frac{\pi^2}{2T} C^E A \tag{2.17}$$

is the motional damping and V is the volume of the antenna. The relative efficiency of an 8 cm diameter, 1 cm thick PADA compared to an 8.1 cm dipole antenna is shown in Fig. 2.14. Similarly to the other mechanical antennas, when $R_m < R_s$, relative efficiency is dominated by $C_o k_t^2$, while for $R_m > R_s$ relative efficiency scales with Q as shown in Fig. 2.14a. The relative efficiencies for various common piezoelectric materials are given in Fig. 2.14b as a function of Q and d_{ij}. Since generally $f \propto 1/(2L) \times \sqrt{C/\rho}$ where L is the dimension of the resonator along the axis of vibration and ρ is the material density, changes in material stiffness or density will result in a frequency change if dimensions are held constant. However, from (2.16) it can be seen that $R_{rad} \propto f^2$ for both the flipping piezoelectric and infinitesimal electric dipoles. Similarly, both R_m, $R_{match} \propto f$. Therefore, the ratio of the two efficiencies is constant with respect to frequency as long as $L \ll \lambda$ and physical dimensions are constant. A general range of the relative efficiencies for various materials is plotted as a function of C, Q, d, C_0, k_t^2 and ε to account for a range of resonator materials and designs. It is further assumed that R_m is kept constant at $R_s = 50\ \Omega$ such that $C_0 k_t^2$ is scaled with Q.

Table 2.2. Comparison of Acoustic Antenna Approaches

Acoustic Implementation	Key Parameters	Advantages	Drawbacks	Anticipated ξ_{tot}^{rel}
Piezoelectric Unipolar	$\sigma, Q, A/V$	Q Scaling	Feedback, Breakdown, Low Fill Factor	> 100
Capacitive Unipolar	σ, Q, g	High fill Factor, Negligible Feedback	Gap Tradeoff Between σ and R_m	> 10
Piezoelectric FDE	$\sigma, \tau, A/V$	Q Scaling, Large σ	FDE σ Decays Rapidly	> 10
Piezoelectric Alternating Dipole	d, Q	High Fill Factor, Large Charge Density, No Charge Decay	Intrinsic Tradeoff Between d and Q	$> 10^6$

Unlike the other types of mechanical antenna that rely on large Q to surpass the efficiency of an infinitesimal dipole, the large coupling coefficients of piezoelectric materials such as lead zirconate titanate (PZT) [88] and lead magnesium niobate-lead titanate (PMN-PT) [89] with antenna Q less than 1000 can result in efficiencies more than one million times greater than a comparably sized dipole. Such low-quality factors are many orders of magnitude lower than the Chu limit for electrical antennas and can potentially enable much larger bandwidths and faster data rates. Since the fields generated by the alternating dipoles are generally confined in the large permittivity piezoelectric material, breakdown and feedback concerns are negligible compared to the other mechanical antenna methods.

A summary of the key parameters, including their relative advantages and drawbacks as well as anticipated efficiency limits relative to ESAs is presented in Table 2.2. Reaching, and ultimately surpassing the anticipated limits will require breakthroughs in electret material research in order to maximize the achievable charge density. Acoustic antennas implemented using a unipolar charge are fundamentally limited by the large electrostatic fields produced by the unipolar charge which electric-field breakdown at much lower charge densities than dipole alternatives. For piezoelectrically actuated linear movement of unipolar charge, the breakdown limit, and thus achievable charge density can be increased packaging the resonator in an insulating gas environment such as SF_6. However, while packaging with insulating gases at higher than atmospheric pressures can increase the achievable charge density, the higher pressure increases resonator damping and results in diminished quality factor. Similarly, for capacitive actuation the charge density can be increased by decreasing the gap between the electret and grounds to a few microns; however, the small gap limits the maximum displacement of the charge and thus radiation power. Due to the fundamental tradeoffs necessary to increase the charge density, there is limited room for further enhancement of unipolar acoustic antennas compared to dipole-based acoustic antennas. Ferroelectric dipole electrets sustain much greater charge densities without experiencing breakdown due to better confinement of the electrostatic field between the opposite polarity charges. However, the large charge densities are susceptible to charge neutralization over time which limits the long-term charge density of FDEs and thus their radiation efficiency to orders of magnitude below the theoretical limit. For acoustic antennas based on torsionally driven FDEs to become viable, methods for repeatedly polling the FDE must be implemented. Piezoelectric alternating dipole antennas (PADAs) provide the most promise for further surpassing the SoA of VLF antennas. The time-varying dipoles inside of the piezoelectric provide confinement of large reactive field generated by the flipping dipole, enabling charge densities similar to FDEs. However, due to the alternating nature of the dipoles, the neutralizing charge does not build up on the surface of the antenna, allowing long-term use without a degradation of performance.

Therefore, PADAs offer the most potential for portable, low-frequency applications and have been demonstrated to surpass equivalent ESA efficiency by more than three orders of magnitude. Orders of magnitude further enhancement of PADAs are projected with further material and resonator optimization. Materials with a large d_{ij}^2Q product such as $LiNbO_3$ (high Q, moderate d_{ij}) and PMN-PT (moderate Q, high d_{ij}) offer the potential for high radiation efficiency. In general, for materials exhibiting the same d_{ij}^2Q product, the material exhibiting the lower Q is preferred due to its larger bandwidth for faster data rates and simpler frequency synchronization for implementation of arrays driven in parallel. In particular, relaxor-type ferroelectrics such as PMN-PT with high coupling coefficients ($d_{ij} > 1000$) and moderate quality factors ($Q < 1000$) exhibit great potential as high efficiency and low-frequency transmitters. The following chapters in this thesis will investigate in depth the theory, design, and characterization of PADAs to demonstrate their practical potential as VLF and LF transmitters.

Chapter 3: Piezoelectric Alternating Dipole Transmitters

3.1 Fundamentals of Piezoelectric Resonators

Piezoelectric materials are materials that transduce energy between the electrical and mechanical domains via the direct and indirect piezoelectric effect. Mechanical energy is converted into electrical energy through the direct piezoelectric effect when a mechanical force on the piezoelectric material leads to the redistribution of internal charges. The opposite energy conversion occurs through the indirect piezoelectric effect when an applied electric field acting on the internal charges results in mechanical strain. For materials to exhibit piezoelectricity, they must exhibit asymmetrical lattice structures as shown in Fig. 3.1, such that redistribution of the lattice results in a change in the polarization of the internal charges.

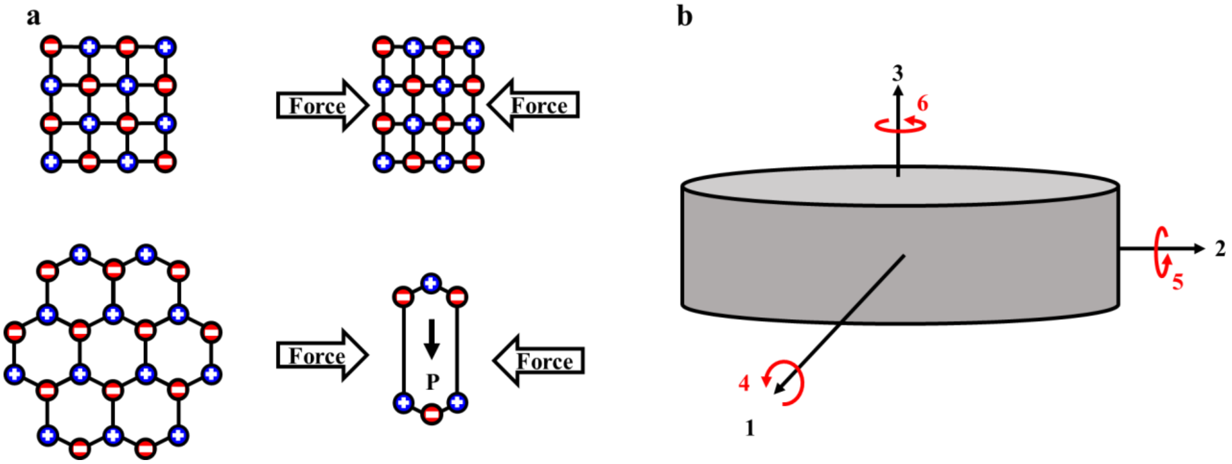

Fig 3.1. (a) The relationship between lattice symmetry and piezoelectricity. (b) Standard piezoelectric axes with the 3-axis in the direction material polarization by convention.

The asymmetry in piezoelectric materials results in differing electromechanical responses depending on how external electric or mechanical forces are applied relative to the lattice. The orientation of the piezoelectric lattice is determined during manufacture by the application of a DC “poling” field which orients the lattice in a specific direction. By convention, the axis along which the material is poled is numbered 3, and the orthogonal axes 1 and 2 as shown in Fig. 3.1b along with the shear directions around the principle axes.

Table 3.1. Piezoelectric Parameters

Parameter	**Symbol**	**Material Parameter**	**Symbol**
Strain [m/m]	S	Elastic compliance [m^2/N]	s
Stress [N/m^2]	T	Elastic stiffness [N/m^2]	c
Polarization [C/m^2]	P	Permittivity [F/m]	ε
Electric field [V/m]	E	Piezoelectric strain constant [C/N]	d
Electric displacement [C/m^2]	D	Piezoelectric stress constant [C/m^2]	e

Piezoelectric materials operating at low levels of mechanical stress and under small electric fields exhibit linear behavior. As the devices described in this manuscript exhibit linear piezoelectric behavior, subsequent discuss of piezoelectric properties will only consider the linear regime. The decoupled direct and indirect linear piezoelectric effects are described in (3.1) and (3.2) respectively

$$P_{pze} = dT_{ext} = dcS_{ext} = eS_{ext} \tag{3.1}$$

$$T_{pze} = cS_{pze} = cdE_{ext} = eE_{ext} \tag{3.2}$$

where all terms and material properties along with their units are provided for reference in Table 3.1. The subscript "pze" denotes a term generated through the direct/indirect piezoelectric effect, while the "ext" subscript denotes externally applied terms. Cross-coupling of the direct and indirect piezoelectric effects is described by the constitutive relations given in (3.3) and (3.4) which couple mechanical stress and strain with electric field and displacement. The coupled equations can be expressed in multiple ways, with two of the most common being the strain-charge form:

$$S_i = s_{ij}^{E} T_j + d_{ik} E_k \tag{3.3}$$

$$D_i = d_{ij} T_j + \varepsilon_{ik}^{T} E_k \tag{3.4}$$

and the stress-charge form:

$$T_i = c_{ij}^{E} S_j - e_{ik}^{t} E_k \tag{3.5}$$

$$D_i = e_{ij} S_j + \varepsilon_{ik}^{s} E_k \tag{3.6}$$

The subscripts denote the direction or pair of directions as defined in Fig. 3.1b and the superscripts *E* and *T* denote whether the quantity is defined under constant electric field or stress respectively while the superscript *t* denotes the matrix transpose. Both sets of equations are fully coupled, and therefore the displacement field *D* given in (3.4) and (3.6) is the same. Since both sets of equations can fully model the behavior of the piezoelectric material provided the appropriate material properties are known, the discussion will be primarily limited to the strain-charge equations for brevity. Equations (3.3) and (3.4) can be expanded into matrix form as:

$$\begin{bmatrix} S_1 \\ S_2 \\ S_3 \\ S_4 \\ S_5 \\ S_6 \end{bmatrix} = \begin{bmatrix} s_{11}^E & s_{12}^E & s_{13}^E & s_{14}^E & s_{15}^E & s_{16}^E \\ s_{21}^E & s_{22}^E & s_{23}^E & s_{24}^E & s_{25}^E & s_{26}^E \\ s_{31}^E & s_{32}^E & s_{33}^E & s_{34}^E & s_{35}^E & s_{36}^E \\ s_{41}^E & s_{42}^E & s_{43}^E & s_{44}^E & s_{45}^E & s_{46}^E \\ s_{51}^E & s_{52}^E & s_{53}^E & s_{54}^E & s_{55}^E & s_{56}^E \\ s_{61}^E & s_{62}^E & s_{63}^E & s_{64}^E & s_{65}^E & s_{66}^E \end{bmatrix} \begin{bmatrix} T_1 \\ T_2 \\ T_3 \\ T_4 \\ T_5 \\ T_6 \end{bmatrix} + \begin{bmatrix} d_{11} & d_{12} & d_{13} \\ d_{21} & d_{22} & d_{23} \\ d_{31} & d_{32} & d_{33} \\ d_{41} & d_{42} & d_{43} \\ d_{51} & d_{52} & d_{53} \\ d_{61} & d_{62} & d_{63} \end{bmatrix} \begin{bmatrix} E_1 \\ E_2 \\ E_3 \end{bmatrix} \tag{3.7}$$

$$\begin{bmatrix} D_1 \\ D_2 \\ D_3 \end{bmatrix} = \begin{bmatrix} d_{11} & d_{12} & d_{13} & d_{14} & d_{15} & d_{16} \\ d_{21} & d_{22} & d_{23} & d_{24} & d_{25} & d_{26} \\ d_{31} & d_{32} & d_{33} & d_{34} & d_{35} & d_{36} \end{bmatrix} \begin{bmatrix} T_1 \\ T_2 \\ T_3 \\ T_4 \\ T_5 \\ T_6 \end{bmatrix} + \begin{bmatrix} \varepsilon_{11}^T & \varepsilon_{12}^T & \varepsilon_{13}^T \\ \varepsilon_{21}^T & \varepsilon_{22}^T & \varepsilon_{23}^T \\ \varepsilon_{31}^T & \varepsilon_{32}^T & \varepsilon_{33}^T \end{bmatrix} \begin{bmatrix} E_1 \\ E_2 \\ E_3 \end{bmatrix} \tag{3.8}$$

3.1.1 MEMS Resonators

In addition to the constitutive equations, another key characteristic of piezoelectric materials is the piezoelectric coupling factor K^2 which characterizes how well energy is converted between the electrical and mechanical domains for a given set of electrical and mechanical boundary conditions.

$$K^2 = \frac{\text{Converted Electrical Energy}}{\text{Input Mechanical Energy}} = \frac{\text{Converted Mechanical Energy}}{\text{Input Electrical Energy}} \tag{3.9}$$

For a thin, piezoelectric disk operating in a dilatational mode such as the one shown in Fig. 2.12 the coupling is defined as:

$$K^2 = \frac{\left(e_{31}^{p}\right)^2}{c_{11}^{p}\varepsilon_{33}^{p}} \tag{3.10}$$

where

$$e_{31}^{p} = \frac{d_{31}}{s_{11}^{E} + s_{12}^{E}} \tag{3.11}$$

$$c_{11}^{p} = \frac{s_{11}^{E}}{(s_{11}^{E})^2 - (s_{12}^{E})^2} \tag{3.12}$$

$$\varepsilon_{33}^{p} = \frac{-2d_{31}^{2}}{s_{11}^{E} + s_{12}^{E}} + \varepsilon_{33}^{T} \tag{3.13}$$

K^2 represents the maximum transduction efficiency for a piezoelectric material and a set of boundary conditions.

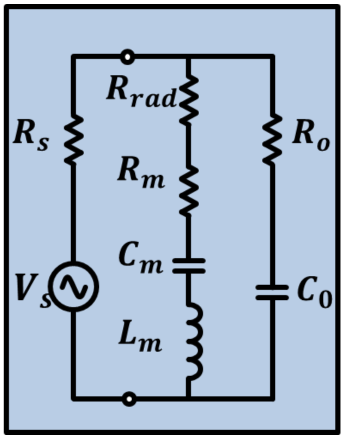

Fig. 3.2. Modified Butterworth-Van Dyke model of piezoelectric resonator.

The equivalent electrical circuit model of the piezoelectric resonator is shown by the modified Butterworth-Van Dyke (MBVD) model in Fig. 3.2 and consists of a motional branch representing the mechanical variables in the resonator in parallel with a static branch representing the electrical variables [90]. The static branch consists of the static capacitance of the resonator (C_0) and the dielectric substrate loss (R_o), while R_s represents the series resistance due to the resonator electrodes. The motional branch consists of a motional resistance (R_m), motional capacitance (C_m)

and motional inductance (L_m) which are analogous to the mechanical damping, compliance and mass coefficients and are defined as:

$$R_m = \frac{\pi^2}{8Q\omega_0^2 C_0 k_t^2} \tag{3.14}$$

$$C_m = \frac{8}{\pi^2} C_0 k_t^2 \tag{3.15}$$

$$L_m = \frac{\pi^2}{8\omega_0^2 C_0 k_t^2} \tag{3.16}$$

where ω_0 is the angular resonant frequency. k_t^2 is a design dependent, effective electromechanical coupling factor defined as:

$$k_t^2 = \frac{\pi^2}{8}\left(\frac{f_s^2}{f_p^2} - 1\right) \tag{3.17}$$

where f_s is the series resonant frequency of the motional branch and f_p is the resonant frequency of the two parallel branches. The motional branch describes the motion in a single resonant mode. If other spurious resonant modes exist within the frequency band of interest, they can be modeled as a parallel branch of motional parameters.

3.2 Fundamentals of Piezoelectric Alternating Dipole Antennas

The efficiency of PADAs discussed in Section 2.4 provides a theoretical discussion of how time-varying mechanical strain in piezoelectric can be leveraged to produce electromagnetic radiation and the material properties that can lead to increased efficiency. The theoretical efficiency limit is based on the assumption that all energy dissipation in a piezoelectric material can be associated either with radiation losses or mechanical losses and that therefore the efficiency with which the piezoelectric resonator radiates is the ratio of the energy lost through radiation to the total energy lost. This assumption only holds true for a resonating piezoelectric in the presence of no external field, such that any dipole moment generated by time-varying strain contributes to radiation. However, in order to excite the piezoelectric into resonance, either an external mechanical force or electric field is necessary. An external mechanical force will not interfere with the radiation from the generated alternating dipoles, however, to generate that force, additional volume is needed for the external actuator, reducing the amount of volume devoted to radiation. Alternatively, thin electrodes can generate an electric field to excite the piezoelectric field into resonance without significantly changing the size of the antenna. However, the electrodes generate a displacement current which partially cancels the radiating piezoelectric current, resulting in diminished efficiency compared to (2.15). In order to maximize the radiation efficiency of a PADA, the maximum radiating current must be excited within the piezoelectric.

3.2.1 PADA Current Elements

Piezoelectric alternating dipole transmitters rely on the piezoelectric effect to generate a time-varying dipole moment that radiates like a current element. To understand the generated dipole moment, it is instructive to first consider the simplified case of a uniform piezoelectric material covered with electrodes on the top and bottom surface. Without loss of generality, a current directed in the z-direction (along the 3-axis) is considered. Currents directed along other directions can be excited by choosing the appropriate piezoelectric geometry and boundary conditions. A DC bias applied to the electrodes results in a static uniform electric field aligned vertically in the z-direction with no fringing components. As with any dielectric material, the applied electric field results in an electric displacement between the electrodes:

$$D_z = \varepsilon E_z = \varepsilon_0 E_z + P_z^{die} \tag{3.18}$$

where ε is the permittivity of the piezoelectric material and P_z^{die} is the dielectric polarization caused by the redistribution of bound charges due to the electric field. Free charge builds up on the electrode which can be broken into two components: σ_0, the charge density required to achieve the bias voltage in the absence of dielectric polarization (i.e. vacuum), and σ_{die}, the charge density required to neutralize the induced polarization inside of the dielectric. When the dielectric material is also piezoelectric, there is an additional polarization term due to the inverse piezoelectric effect. From (3.2) the external electric field results in stress (either tensile or compressive depending on the sign of the piezoelectric coefficient d) which in turn results in a piezoelectric polarization as shown in (3.4). Note that when defining the piezoelectric polarization using (3.4) that the polarization is due the stress both from the external electric field, as well as the stress generated by the internal electric field caused by the redistribution of charges inside the piezoelectric due to the changing strain as shown in (3.5). The piezoelectric polarization results in a third component of free charge σ_{pze} on the electrode in order to maintain the applied potential. Figure 3.3 depicts the internal polarization and corresponding surface charges for a biased piezoelectric with no fringing fields. Both the dielectric and piezoelectric polarizations inside the piezoelectric are in the same direction as the applied electric field. Alignment of the polarization and the external electric field is maintained regardless of piezoelectric polarization, as the internal charges will always move toward a lower potential. The direction of the polarization is shown in (3.1), since reversing the poling of a material reverses the sign of the coupling matrix d, and thus also the sign of the stress if the electric field is constant as shown in (3.2). Adjacent charges of opposite polarity will cancel, such that the effective surface charge on the electrodes is determined only by σ_0 as shown in Fig. 3.2b.

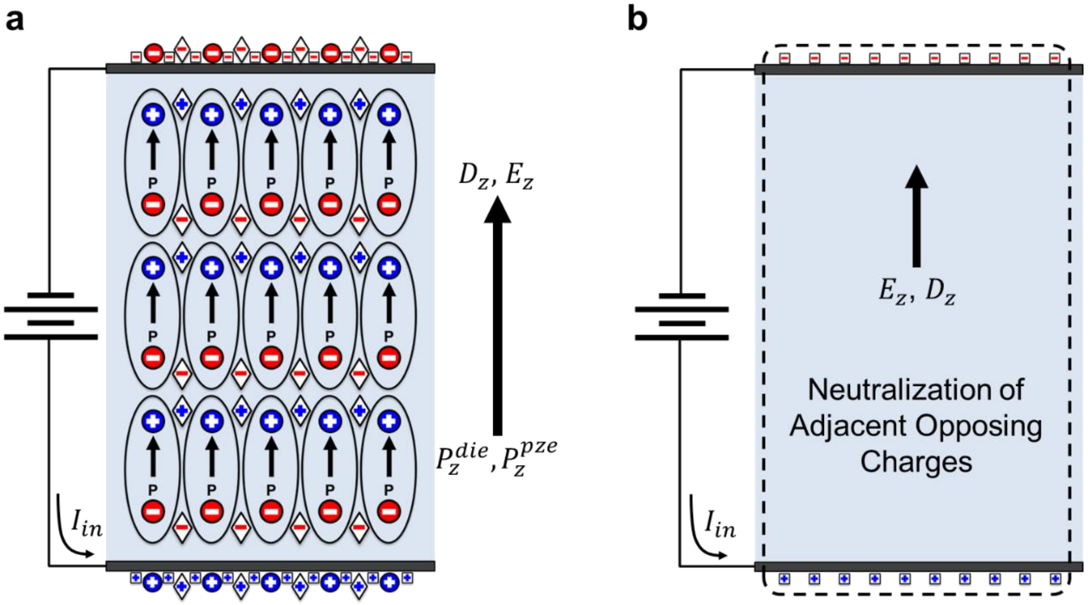

Fig. 3.3. Currents inside fully piezoelectric material with electrodes completely covering the top and bottom surface. (a) All generated charge components. (b) Net charge and fields after the cancellation of opposing charges.

If a time-varying voltage is applied to the electrodes, a displacement current will be formed between the electrodes, where the displacement current density is $J_z = dD_z/dt$. Therefore, regardless of the permittivity or coupling coefficient of the piezoelectric, the effective current inside the piezoelectric will be approximately equal to the input current

($I_{in} \approx \int_{electrode\ area} J_z\, dA$) assuming the amount of fringing field is small. While the displacement current will contribute to radiation, it is diminished due to the neutralizing charges and results in decreased efficiency. In order to avoid cancelation of the strain-induced piezoelectric polarization, the size of the electrode may be diminished such that only a portion of the piezoelectric surface is covered as shown in Fig. 3.4. Under the assumption that the external electric field from the applied voltage is confined purely between the electrodes, then the portion of the piezoelectric covered by electrodes still experiences charge neutralization. However, in the regions with no electrode, there is no free charge on the surface to neutralize the piezoelectric polarization which results in an effective piezoelectric charge density on the surface as shown in Fig. 3.4b. In the regions where the fringing fields are small, the electric displacement field is negligible and $d_{ij}T_j \approx \varepsilon_{ik}^{T} E_k$.

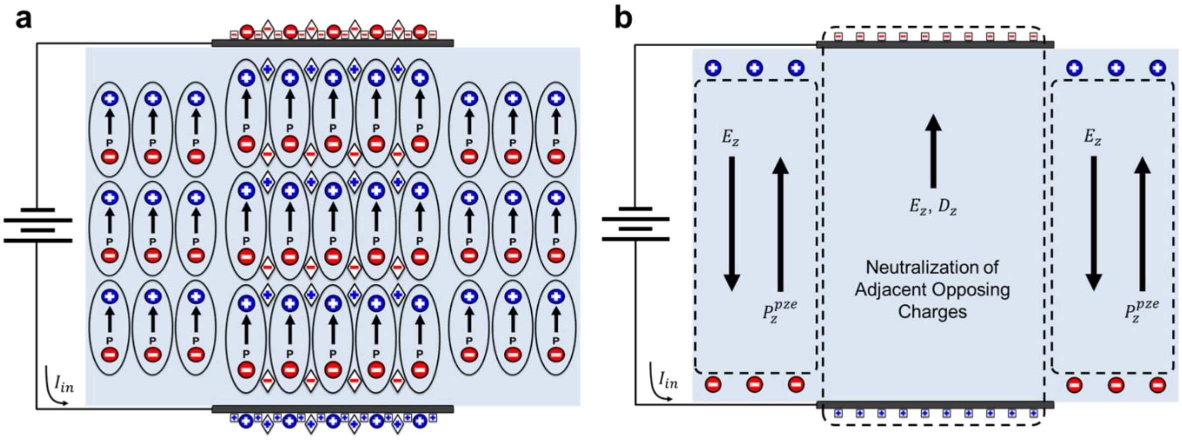

Fig. 3.4. Charge generation in a piezoelectric material partially covered by electrodes if there is no fringing component of the external electric field outside of the area covered by electrodes. (a) All generated charge components. (b) Net charge and fields after the cancellation of opposing charges.

Depending on the geometry of piezoelectric material and the electrodes, it is not necessarily reasonable to assume that fringing fields are negligible as is done in Fig. 3.4. If the fringing fields are significant, in addition to the cancellation of the piezoelectric charge in the area between the electrodes, there may also be some cancellation area close to the electrode as shown in Fig. 3.5. The semi-transparent electrodes and charges represent the fringing field, which behaves serves to effectively increase the area of the electrode. Although the free charge density σ_0 does not change, the fringing fields cause an increase in both the piezoelectric and dielectric polarization and a corresponding increase in free charge which neutralize those. Consequently, only a portion of exposed piezoelectric material contributes to the piezoelectric charge density. Therefore, in general, increasing the volume of the piezoelectric through which negligible fringing fields pass results in an increase in radiation efficiency.

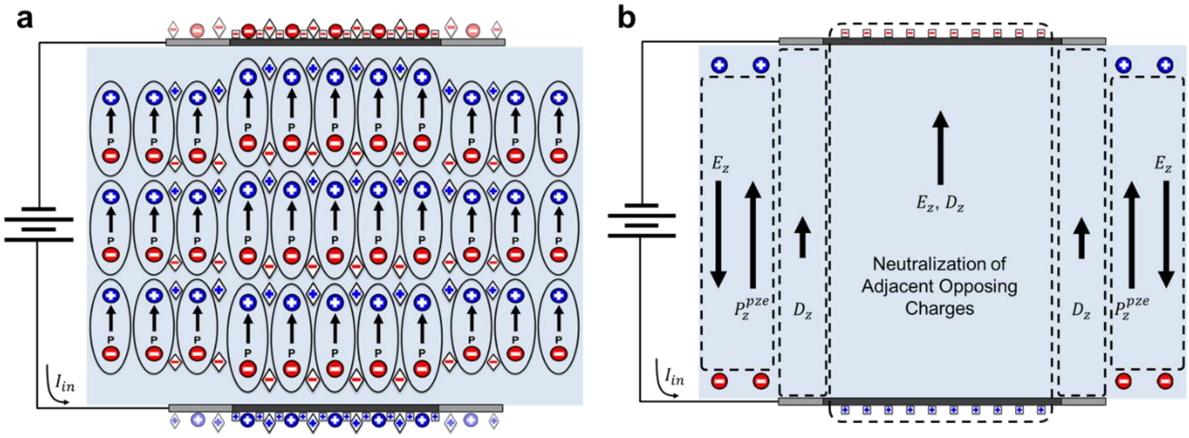

Fig. 3.5. Charge generation in a piezoelectric material partially covered by electrodes if there is some fringing component of the external electric field outside of the area covered by electrodes. (a) All generated charge components. (b) Net charge and fields after the cancellation of opposing charges.

In order to turn the effective piezoelectric charge density into a radiating current, a time-varying electric field is applied to the electrodes, resulting in a time-varying stress field in the piezoelectric. If the boundary conditions of the piezoelectric material are mechanically free to move, then the applied stress results in a time-varying strain as shown in (3.3). The time-varying strain results in an effective current as the piezoelectric dipoles in the unexposed region alternate back and forth. Near the resonant frequency, the Q of the resonators results in the amplification of the mechanical and electrical energy. The increased energy results in greater time-varying stress and thus flipping dipole moment from (3.5). The relation between time-varying strain and the generated piezoelectric polarization in the 3-direction is shown in Fig. 3.6 for a resonator operating in its fundamental extensional mode. In the fundamental extensional mode, the stress in a single direction is unidirectional at a single instance of time, resulting in a unidirectional piezoelectric dipole moment. Therefore, all the piezoelectric dipoles are aligned and add constructively. If the piezoelectric is driven in a higher-order mode, such as shown in Fig. 3.7, then the stress components in the 3-direction are no longer unidirectional, as a portion of the piezoelectric experiences compressive stress, while another portion experiences tensile stress. Consequently, the induced piezoelectric dipoles are oriented in opposite directions in the regions with opposite stresses, resulting in the partial cancelation of the piezoelectric polarization and thus the radiating piezoelectric current. Due to the internal cancelation of higher-order modes, resonators operating in the fundamental mode generally yield the greatest efficiency.

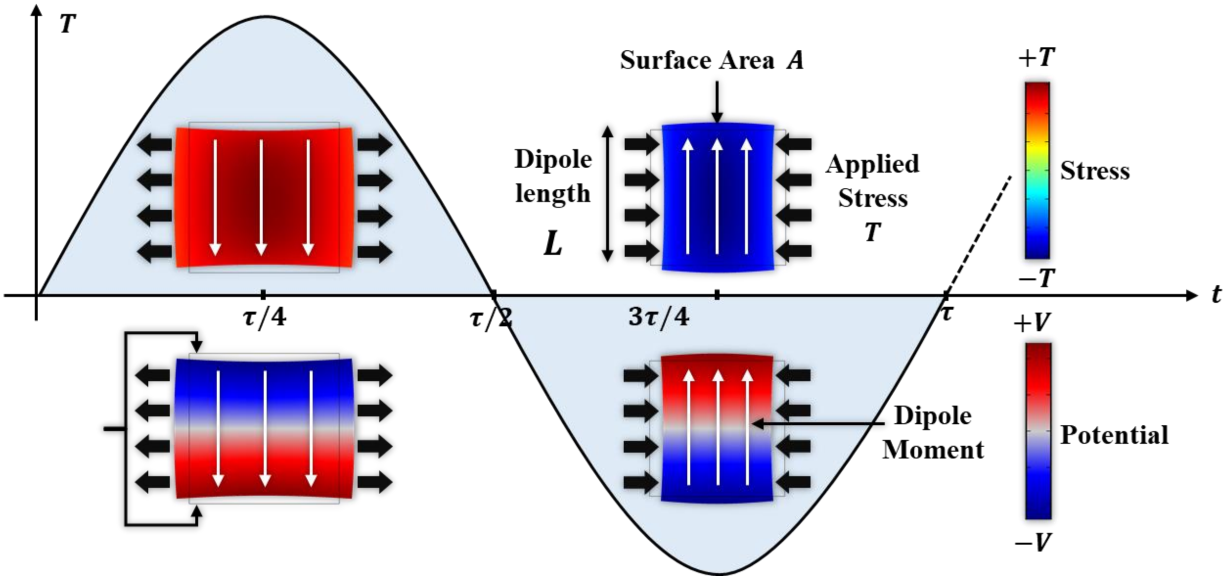

Fig. 3.6. Conceptual illustration of the piezoelectric transduction between mechanical (stress) energy and electrical (potential) energy.

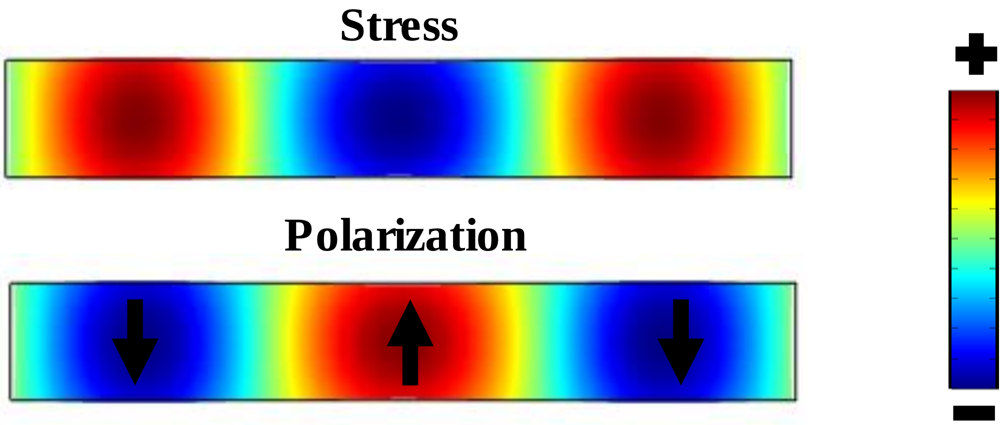

Fig. 3.7. Dipole moment cancelation in higher-order modes.

While the stress in Figs. 3.6 and 3.7 has been considered to be one-dimensional for simplicity, in reality, the stress in all directions contributes to the polarization. From (3.5), the piezoelectric polarization can be expanded as $P_3^{pze} = \sum d_{ij} T_j$, where the polarization in the 3-direction is due to the stress in the 1, 2, and 3 directions. For a resonator in the fundamental extensional mode (3-

direction), as the piezoelectric expands in the 3-direction due to tensile strain, the material will also contract in the transverse direction along the 1, 2 axes as defined by the Poisson ratio, resulting in compressive (negative) stress. In general, d_{31}, d_{32}, have the opposite sign as d_{33} and therefore $d_{31}T_1 + d_{32}T_2 + d_{33}T_3$ will add constructively, while the shear stress components are negligible in magnitude and can be neglected. The current in the z-direction can then be written as:

$$I_z = \omega A P_z = \omega A d c^E S \tag{3.19}$$

where A is the unmetallized surface area of the resonator as shown in Fig. 3.5, and P_z is the total piezoelectric polarization in the z-direction. Then the far-field magnetic field generated by this strain induced current is formulated as [46]:

$$\left|B_{far}\right| = \frac{PA}{4\pi\varepsilon_o}\frac{L\omega^2}{c^3 R} \tag{3.20}$$

where L is the dipole moment length, ε_o is the permittivity of the free space, and c is the speed of light. The corresponding far-field electric field is defined as $\left|E_{far}\right| = c\left|B_{far}\right|$. The field generated in (3.18) is identical to the radiation from an ideal dipole with current $I = j\omega PA$, and thus it is reasonable to treat the radiation from the piezoelectric current in (3.19) similarly to the radiation from an ideal dipole with an equivalent current. In addition to the currents in the z-direction. there is also a radial component to the displacement current as shown in Fig. 3.8 due to the fringing fields. Due to symmetry in the piezoelectric resonator around the z-axis, an axisymmetric simulation is used to reduce simulation time. The radial currents are in opposite directions on the top and bottom surfaces of the piezoelectric, and therefore cancel each other out such the currents generated by a fundamental thickness extensional or dilatational mode rod are purely in the z-direction.

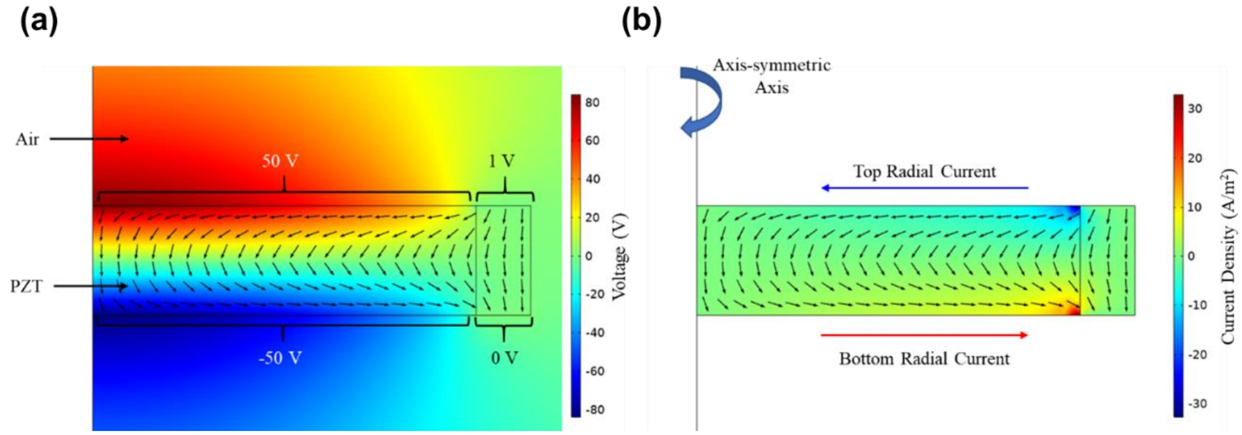

Fig. 3.8. Radial currents within a disk or rod resonator. (a) The voltage generated by the piezoelectric polarization in the portion of the piezoelectric with no electrodes. The voltage between the electrodes is defined solely by the voltage applied to the electrodes, while the voltage on the exposed portion of the piezoelectric is greatest far from the electrodes where the fringing fields are smallest. (b) The radial current in the piezoelectric. The arrows denote the direction of the current while the color bar gives the magnitude.

3.2.2 PADA Field Confinement

In addition to the currents inside the PADA, the behavior of electric fields in and around a PADA is very important for efficient operation. As discussed in Chapter 2, piezoelectric materials with large permittivity confine the reactive near-fields generated by both the applied external field and the field-induced internal dipole generation inside the piezoelectric. As the bound charge densities on the top and bottom surfaces of a PADA are flipped to induce the dipole current for radiation, an electric field E_{ext} is produced outside of the piezoelectric. This electric field is inversely proportional to the relative permittivity ε_r is the relative permittivity of the piezoelectric material:

$$E_{ext} \propto \frac{P}{\varepsilon_r \varepsilon_o} \tag{3.21}$$

The radiated field strength for an antenna is determined by the maximum achievable current on the antenna and its distribution. In the case of PADAs, where the current is determined by the polarization, the maximum current limit is determined by the charge density that results in electric near-fields just below the breakdown limit of the surrounding environment.

$$E_{breakdown} \propto \frac{P_{max}}{\varepsilon_r \varepsilon_o} \tag{3.22}$$

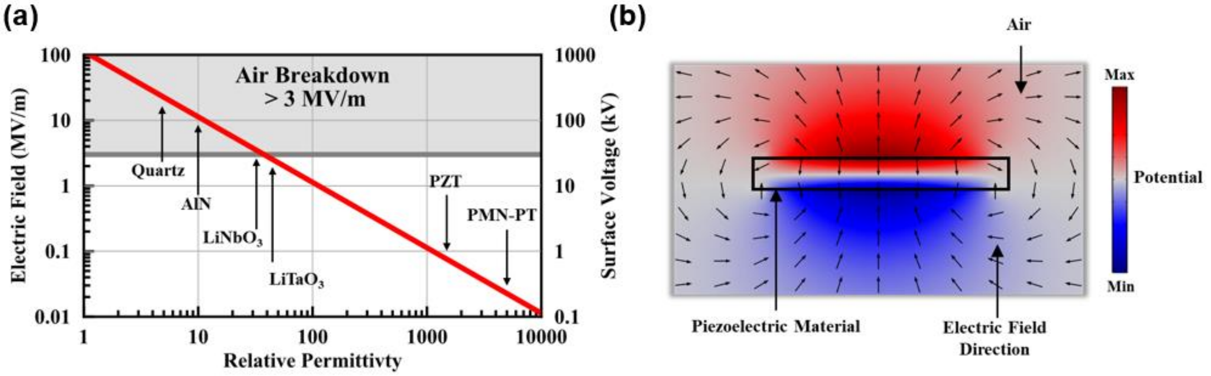

Fig. 3.9. Comparison of electrical polarization response for different piezoelectric materials. All materials are assumed to have a charge density of ±1 mC/m^2 on the top and bottom surfaces with a thickness (distance between surfaces) of 1 cm. (a) The electric field and the corresponding surface voltage versus the piezoelectric material relative permittivity. The top gray region is the air breakdown region where the electric field exceeds 3 MV/m. (b) The voltage distribution due to the electric polarization and the electric field direction represented by the black arrows.

Therefore, the maximum radiated field strength is directly proportional to the relative permittivity of PADA. Higher permittivity materials result in better confinement of the fringing electric near-field generated by the induced polarization. Figure 3.9a compares a few commonly used piezoelectric materials with different values of relative permittivity. The same charge density of 1 mC/m^2 is assumed on the top and bottom surfaces while the generated electric field and the corresponding surface potential are calculated for a piezoelectric material with a thickness of 1 cm. Figure 3.9b shows a piezoelectric material at resonance surrounded by air and its corresponding voltage distribution, where the fringing electric field is represented by the black arrows.

In addition to enabling greater piezoelectric far-field radiation, confinement of the near-fields inside the high permittivity material reduces the near-field regime of PADAs compared to metal ESAs. As discussed in Chapter 1, the cross-over point for an electrical antenna in air occurs at a distance $\lambda/2\pi$ and is the point where the radiating electromagnetic fields generated by the accelerating charges become larger in magnitude than the near-fields caused by the reactive fields. The relative cross-over distances for PADAs comprised of three different permittivity materials are shown in Fig. 3.10b. The fields are simulated using the same setup described in Fig. 3.9b. Since the magnitude of the near-field components of an antenna is due to time-varying electrostatic fields, the magnitude of the near-fields of different permittivity antennas can be extrapolated as shown in the figure below. Thus, as the permittivity increases, the reactive field is better confined within the high permittivity material as shown in Fig. 3.10a. This makes sense when considered from the standpoint of Gauss's law, which tells us that since the total charge in each case is constant, the electric flux generated by that charge is constant too. As permittivity, and thus capacitance increases, the amount of energy stored inside the dielectric capacitor increases, and thus the energy (magnitude of the fields outside the piezoelectric antenna) must decrease by a corresponding amount.

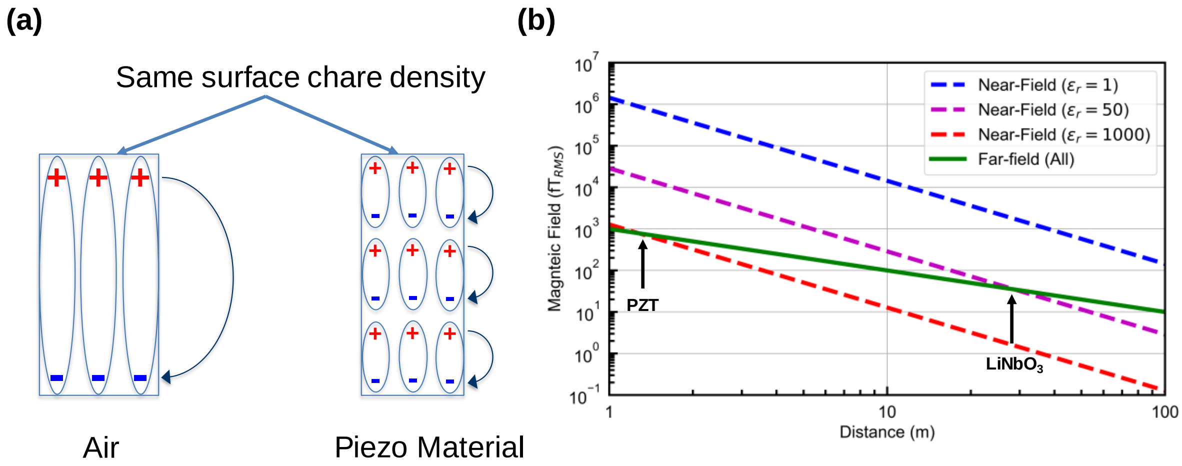

Fig. 3.10. Redefinition of traditional near- and far-field regimes. (a) Confinement of the reactive fields in high permittivity materials due to the alignment of internal dipoles results in a smaller near-field magnitude and thus shorter cross-over distance since the radiated far-field is independent of antenna permittivity. (b) Simulated cross-over distance for a PADA antenna comprised of three different permittivity materials ($\varepsilon_r = 1$ case approximates an equivalent infinitesimal dipole).

While the radiated fields corresponding to these near-fields cannot be simulated simultaneously, the radiation is due to the acceleration of the charges in the piezoelectric and such radiation of accelerating charge has been extensively described in the literature. The radiated power from any accelerating charge (including those in a dielectric) is given by Larmor's formula and is a function of the rate of acceleration. It should be noted that moving charges in dielectrics can also radiate due to moving faster than light in the material (Cherenkov radiation) or from transitioning between two dielectric medium, however, neither of these occurs in the PADA antenna and thus radiated power can be determined solely from Larmor's formula. Therefore, while the total reactive and radiated energy is maintained assuming the charge distribution is constant, the ratio of the reactive to radiated fields antenna decreases with increasing permittivity since a larger amount of the reactive field is stored inside the piezoelectric.

The distance at which the cross-over occurs is dependent on both the permittivity of the PADA as well as its geometry. In general, decreasing the aspect ratio of the antenna or increasing the permittivity of the PADA results in greater confinement of the near-field energy inside of the piezoelectric, and therefore a closer cross-over point. The cross-over point for a rod-shaped PADA as a function of permittivity and aspect ratio is simulated in Fig. 3.11. The PADA consists of a piezoelectric rod with a 1 cm radius covered by an electrode of a radius of 1.5 mm is shown in Fig. 3.11a. The cross-over reduction of the PADA for different values of permittivity and thickness is shown in Fig. 3.11b under the assumption that the antenna radiates at 70 kHz. While the permittivity of the piezoelectric is the largest contributor to field confinement inside the PADA, the geometry of the PADA can also cause the cross-over distance to change by a factor of more than 4.

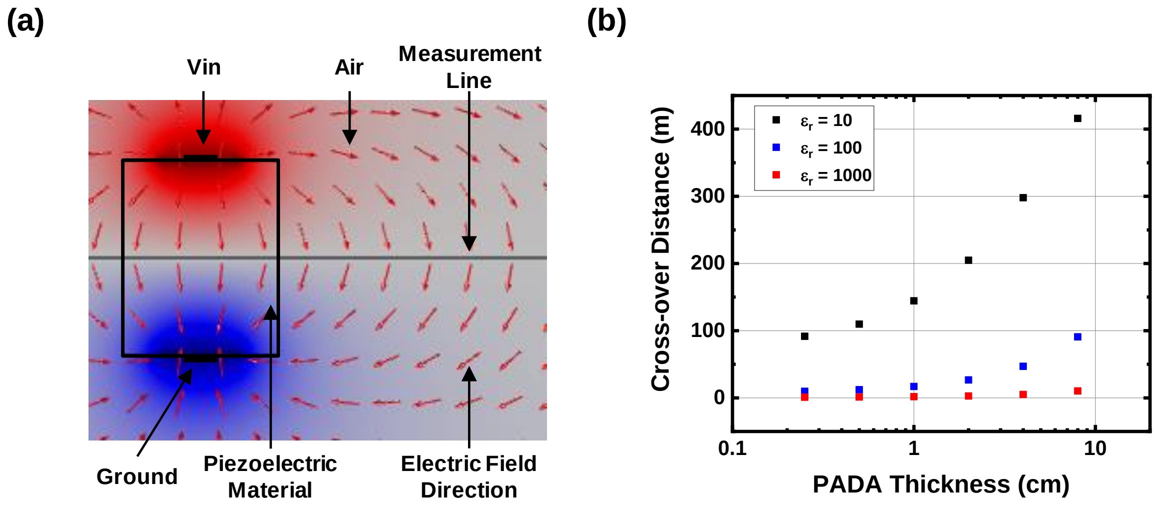

Fig. 3.11. Redefinition of traditional near- and far-field regimes. (a) Confinement of the reactive fields in high permittivity materials due to the alignment of internal dipoles results in a smaller near-field magnitude and thus shorter cross-over distance since the radiated far-field is independent of antenna permittivity. (b) Simulated cross-over distance for a PADA antenna comprised of three different permittivity materials ($\varepsilon_r = 1$ case approximates an equivalent infinitesimal dipole).

3.3 PADA Material Considerations

3.3.1 High Efficiency FoM

Since a high matching efficiency is easily obtainable for most piezoelectric antennas through geometric design choices, material choices are primarily focused on improving radiation efficiency as governed by (2.15). For fundamental resonant antennas, the dimensions, and thus volume, are set by the operating frequency and acoustic phase velocity. Additional volume scaling can be done by driving multiple PADAs simultaneously, and thus resonator volume is generally independent of material choice as it can be arbitrarily increased regardless of design. Therefore, high radiation efficiency materials are determined by their $d^2 C^E Q$ product and a new FoM is introduced to enable higher maximum radiation.

$$FoM = d^2 C^E \varepsilon_r Q \tag{3.23}$$

Table 3.2 provides a list of the FoM for several common piezoelectric materials [77], [91]. It should be noted that the FoM reported in Table 3.2 are general for the materials and change based material orientation and resonator design. Due to the limited reports of piezoelectric antennas at the time of writing [48], the recorded FoMs do not represent a true state of the art for the field of piezoelectric antennas but rather an approximation based on sampling reported parameters for common piezoelectric materials.

Table 3.2 Piezoelectric Material FoM

Material	Q	c^e **[GPa]**	d **[10^{-12} C/N]**	ε_r	**FoM**
Quartz [76]	$> 10^6$	~100	1−2	4	$\sim 10^{-6}$
AlN [63]	> 5000	~400	1−5	10	$\sim 5\times10^{-6}$
LN [48]	$> 10^5$	~200	6−70	30	2×10^{-6}−3×10^{-4}
PZT [131]	> 2000	~200	100−400	600-1000	0.004−0.06
PMN-PT [89]	< 100	~100	1500−4000	800-1500	0.03−1
PMN-PZT [110]	100	c_{33} = 107	d_{33} = 1530	4850	0.12
PMN-PZT-Mn [110]	1050	c_{33} = 120	d_{33} = 1140	3410	0.55
PIC-181 PZT [131]	2200	c_{11} = 152	d_{31} = -108	1135	0.004
		c_{33} = 134	d_{33} = 253		0.022
		c_{55} = 28	d_{15} = 389		0.0013

In general, high FoM is constrained by the intrinsic tradeoff between a high quality factor and large piezoelectric coupling. Quality factor is a measure of energy loss within the resonant system, and therefore Q is maximized when sources of loss are minimized. Losses in a PADA can be divided into intrinsic sources of loss within the piezoelectric material, and external sources of loss that occur when implementing the resonator system. Here, discussion of loss is limited to intrinsic sources of loss, since external sources of loss such as anchor loss [92], [93], damping loss [94] and ohmic loss in metal electrodes are generally independent of piezoelectric material choice and instead are a function of resonator design. Intrinsic sources of loss include phonon-phonon loss [95], phonon-electron loss [96], Akheiser damping [97], piezoelectric loss [98], and dielectric loss [99].

Of particular interest for high FoM PADA materials are the piezoelectric and dielectric losses, which are generally negligible for low coupling materials such as quartz or AlN [100] but increase significantly for higher piezoelectric coupling ferroelectrics [101] and therefore can be the limiting source of loss in PADAs comprised of relaxor ferroelectrics like PMN-PT. Dielectric loss is caused by the movement of charges inside a material in the presence of an electric field and the corresponding thermal dissipation associated with that charge displacement [102]. Dielectric loss is characterized by the loss tangent of the material which is defined as the ratio of the imaginary and real components of permittivity ($\tan\delta = \epsilon''/\epsilon'$) and generally a function of the frequency of the applied electric field [103].

Debate is ongoing as to the exact nature of piezoelectric loss [104], [105] but it has been observed that materials such as PMN-PT and PZN-PT which exhibit loss tangents similar to hard PZT piezoelectrics ($\tan\delta < 0.004$) exhibit lower mechanical Q's close to 100 which are more in line with soft PZT [106]. The disparity between the mechanical Q and loss tangent is indicative of another loss mechanism, which has been attributed to the influence of damping in the moving piezoelectric domain walls [107]. Recently, efforts to minimize damping from spontaneous polarization due to an external field via acceptor ion doping have shown promise for enhancing mechanical Q [108], [109], however the exact cause of loss reduction remains uncertain. Increasing the mechanical Q of the doped ferroelectrics comes at the expense of decreased piezoelectric coupling, however, as shown in Table 3.2, manganese ion doping can still lead to a more than 4x increase in FoM [110]. Efforts to improve the d^2Q material FoM are ongoing, but materials such as PMN-PZT-Mn already show the potential to further exceed the material efficiency of the PZT reported here by more than 10x.

Although maximizing radiation efficiency is essential for increased battery life in portable transmitters, the presented FoM only holds for PADAs operated in the linear regime. At elevated input powers, PADA radiation efficiency can be limited by the intrinsic thermal and mechanical nonlinearity of the acoustic resonators, as well as the maximum achievable surface charge density without breaking down the surrounding medium. Therefore, in addition to (3.23), maximum achievable radiated power must also be considered when choosing PADA materials.

High *Q* PADAs exhibit a greater ratio of power dissipated via radiation to power dissipated via heat, and therefore are less susceptible to thermal limitations and instead limited by maximum achievable charge density. Insulating gases have been shown to increase the breakdown field strength of the surroundings of the piezoelectric antennas but at the cost of increased cost and packaging complexity and diminished *Q* [48]. Conversely, high coupling relaxor ferroelectrics exhibiting similar charge densities are well below the breakdown threshold as shown in Fig. 3.9, and are therefore generally not limited by surface charge density. However, the lower *Q* results in increased heat dissipation in the resonator and a corresponding temperature increase.

The temperature rise from joule heating in the electrodes and mechanical energy dissipation causes a change in the stiffness of the resonator as governed by the temperature coefficient of elasticity. The thermal change in elasticity results in a corresponding change in the resonant frequency determined by the resonator’s thermal coefficient of frequency (TCF). As temperature increases, the resonant frequency decreases due to the negative TCF of PZT and the resonator admittance increases, resulting in more power absorption and greater heating and thus a nonlinear feedback loop. Due to the feedback loop, in the nonlinear regime the resonant frequency shifts away from the input signal, resulting in off-resonant driving and diminished radiation efficiency. Thermal nonlinearity is primarily governed by the thermal conductivity of the resonator [111], [112], which for high coupling ferroelectrics such as PZT and PMN-PT is generally < 2 W/m-K [113]–[115] compared to $LiNbO_3$ which is near 5 W/m-K [116]. Further investigation on the improvement of thermal conductivity of potential ferroelectric PADA materials is needed, and improvements in power handling via increased *Q* or thermal conductivity must be balanced with decreased coupling as material stoichiometry and doping is investigated [115].

Ultimately, while relaxor ferroelectrics show great promise as highly efficient PADA materials, significant further research is needed for practical implementation. PADAs operating in the VLF and LF regimes require materials that can be fabricated with minimum dimensions of 1 cm or greater, significantly larger than the thin films typically reported in literature. While $LiNbO_3$ PADAs with dimensions greater than 10 cm and Q of 600,000 have been reported [48], reports in literature for PZT and other perovskite ferroelectric based materials such as PMN-PT with $d_{ij} > 1000$ pC/N are generally for thin films (< 1 mm). The high coupling in perovskite ferroelectrics is enhanced near the morphotropic phase boundary (MPB) from rhombohedral geometry to a tetrahedral geometry based on material composition or stress [117]–[119]. Near the MPB, material properties such as loss tangent, permittivity and coupling can vary greatly due to small changes in stoichiometry, stress or temperature [120] and is therefore sensitive to fabrication and environment. Common growth techniques such as the flux method [121], Bridgman method [122] or gradient freeze method [123] can be used to achieve the desired stoichiometric composition, but can exhibit significant variance in coupling and permittivity in cm scale crystals. Therefore, although high Q materials such as $LiNbO_3$ and high coupling materials such as PZT and PMN-PT show promise for improved PADA performance, significant work is required to improve the FoM, manufacturability and repeatability of PADA materials.

3.3.2. High Modulation Rate

In addition to efficient radiation with large radiated power, passband transmission requires a modulation technique to send information. Simple and common digital modulation schemes can be utilized such as binary amplitude, frequency, and phase-shift keying (BASK, BFSK, BPSK) to directly modulate the PADA (carrier) amplitude, frequency or phase with a modulating bit stream [124]. A mechanical antenna such as the PADA has a settling time that is directly proportional to its quality factor and limits the BASK (on-off keying) rate since the mechanical system must be switched on and off corresponding to bit 1 and bit 0, respectively. The same applies to BPSK due to the phase discontinuity that requires the system to resettle and synchronize with the driving signal every time the phase changes. This presents a tradeoff between the material quality factor, which is required for efficient antenna operation, and the maximum achievable data rate, which is required for bandwidth efficiency [124]. On the other hand, BFSK can be designed to have a fixed amplitude and continuous phase, sometimes referred to as continuous phase FSK (CPFSK), or minimum-shift keying (MSK), which mitigates the amplitude settling limitation and dramatically improves the achievable data rates. An FoM presenting the characteristics of a BFSK modulator can be expressed as follows:

$$FoM_{Mod} = \Delta f \times FSK_{Rate} \tag{3.24}$$

where Δf is the separation between the two frequencies representing the binary message ($\Delta f = f_2 - f_1$) and FSK_{Rate} is the maximum achievable FSK rate for switching between the two frequencies. For practical systems, Δf must be as large as possible to allow for larger separation between the band-pass filters (BPF) in the receiver, which relaxes the BPF design specifications and reduces the bit error rate (BER), while higher FSK_{Rate} enables higher bit rates (for BFSK $Bit_{Rate} = 2 \times FSK_{Rate}$). The maximum frequency separation is generally set by the 3-dB bandwidth of the transmission system, which is inversely proportional to the PADA Q. Thus, there is a tradeoff between high Q for efficient radiation and low Q for large bandwidth and fast settling times. High radiation FoM materials that do not rely on a high Q such as PZT and PMN-PT are thus preferable for high efficiency and data rate.

Although ferroelectric relaxor materials like PMN-PT can yield a high FoM despite a moderate Q, maximizing the FoM of any PADA material will require achieving the highest possible Q either through material fabrication or resonator design. Since data rate is dependent on both bandwidth and the signal to noise ratio (1.12), increasing bandwidth at the expense of efficiency does not necessarily yield faster communication speeds. Modulation schemes such as direct antenna modulation (DAM) that are able to decouple modulation rate from antenna bandwidth have been demonstrated to have great promise VLF and LF resonant antennas [125]–[127] including VLF piezoelectric antennas [48]. Soon after the work by Chu and others describing the bandwidth limitations of electrically small antennas, DAM schemes were proposed as a method to overcome the intrinsic high Q, low bandwidth limit [128], [129].

Without DAM, modulation rates are limited by the charging and discharging time between modulated symbols, with the charging time constant limiting the symbol duration and thus data rate. DAM overcomes the charging time constant limitation by actively switching the stored energy between the different modulation states to avoid charging and discharging. For electrical antennas, switching between symbols is synchronized so that during the switching moment, the antenna is either in the minimum magnetic energy (zero current) or electric energy (zero voltage) state. For piezoelectric antennas, switching should occur in either the minimum kinetic energy state (no velocity) or electrical energy state (no acceleration) so that the stored energy switches to the new symbol state as though the piezoelectric resonator is operating at its steady state.

A mock-up of an FSK-DAM scheme for a PADA is shown in Fig. 3.12, where a capacitor C_T is used to tune the resonator impedance to change the resonant frequency between the two switched frequencies with the tuned resonance frequency given by (4.2). At resonance, resonator velocity is in phase with the input voltage, and therefore frequency switching is synchronized to occur when the input voltage and mechanical energy are minimum. As the switch is flipped, the new frequency state simply "resumes" operation by converting its stored potential energy into kinetic energy the same as it would if it had been in steady-state oscillation at that frequency the whole time. Therefore, as long as the tuning capacitor is chosen so that the two resonant frequencies correspond to the two FSK states, charging time between symbols is negligible the data rate can surpass the limit imposed by the charging time-constant. As can be seen in Fig. 3.12b, adding the series tuning element results in a decreased quality factor, and therefore the radiation from the tuned state will be diminished relative to the non-tuned state. Increasing the tuning range further decreases the radiation from the tuned state, and therefore limits the maximum possible tuning range. Additionally, at elevated input powers, the resonant frequency of the PADA at both the tuned and untuned frequencies will shift based on the thermal coefficient of frequency of the resonator, causing the switching to desynchronize with the desired energy state. Since low Q resonators exhibit less stored energy and a less sharp phase transition near resonance, they are less affected by desynchronization than high Q resonators and therefore still offer an advantage even with DAM.

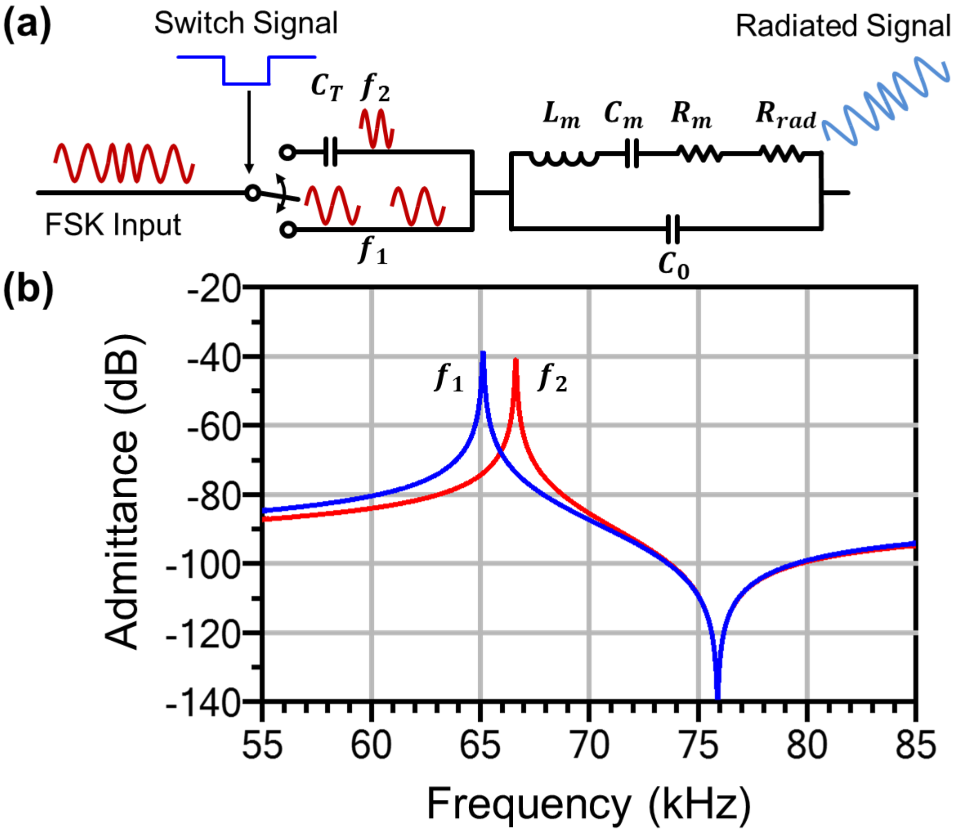

Fig. 3.12. Direct antenna modulation (DAM) of a PADA antenna. (a) Mock-up of a DAM scheme using a capacitive tuning element to tune switch PADA resonance along with an input FSK signal. (b) Shift in PADA resonance frequency from switching to a tuning capacitor in series with the piezoelectric resonator.

Chapter 4: PADA Design and Fabrication

To demonstrate the viability of PADAs for VLF communication, two prototype antennas are designed and fabricated. First, a prototype PADA is to demonstrate the viability of piezoelectric transmitters for compact VLF communication systems, and thus is constrained to a size of 50 cm^3 and to operate in the VLF frequency band. A high FoM, moderate Q material is chosen to balance high efficiency and modulation rate. Second, a PADA utilizing a higher FoM mode is demonstrated to experimentally verify the potential for higher FoM materials and modes to increase the antenna efficiency and extend the communication distance.

4.1 PADA Design

The ideal materials for a piezoelectric antenna exhibit both a high FoM as demonstrated in Table 3.2, as well as a moderate Q to enable higher modulation rates. Multiple materials such as $LiNbO_3$, PZT, and PMN-PT have shown the potential for high FoM, and thus efficiency, as shown in Fig. 2.13. However, of the materials with high PADA FoM, relaxor materials such as PMN-PT and PZN-PT with high coupling and low quality factors exhibit the potential for fastest data rates and therefore are prominent candidates for achieving the state-of-the-art piezoelectric antennas.

4.1.1 Disk PADA Design

In addition to the desirable material properties, manufacturability must also be considered when choosing a PADA material. Research into relaxor materials is ongoing, and many of the reported high FoM compositions are not commercially available. Additionally, since the size of fundamental mode resonators is inversely proportional to frequency, PADAs require piezoelectric resonators with dimensions of approximately 10 cm to operate in the VLF range. Increased fabrication and poling complexity make it difficult to source sufficiently large pieces of PMN-PT for fundamental resonant operation < 30 kHz. Thus, PZT is chosen as the PADA prototype material for its high FoM, sizing availability and consistent material properties. The first PZT PADA is designed from a ceramic PIC181 disk sold by Physik Instrumente which offers both high Q and piezoelectric strain coefficients as shown in Table 3.2. Different resonator geometries can be used to excite different high coupling piezoelectric materials such as the ones in Table 3.2 in optimal resonant modes (such as dilation, thickness extensional or shear) but were not available in sizes that could resonate in the VLF range. Therefore, due to sizing constraints, a lateral mode of vibration is chosen to utilize d_{31}. A dilating disk as shown in Fig. 4.1 is chosen over a rectangular plate to most efficiently excite strain-induced polarization. The frequency of the fundamental dilation mode of a thin plate with thickness much smaller than the diameter can be approximated as [130]:

$$f_0 = \frac{\kappa}{R}\sqrt{\frac{C_{11}}{\rho}} \tag{4.1}$$

where κ is a parameter dependent on Poisson's ratio, R is the radius of the disk and ρ is the density. The lateral vibration of the disc, also known as contour mode or dilation mode, is excited by applying a time-varying voltage on the metalized edges of the PZT disc. Upon excitation, the time-varying electric field introduced by the electrodes (configured as a pair of top and bottom electrodes) excites the piezoelectric disk into vibration via the reverse piezoelectric effect. The excited acoustic wave is reflected by the PZT disk boundaries, resulting in a standing acoustic wave with its maximum stress at the disk center.

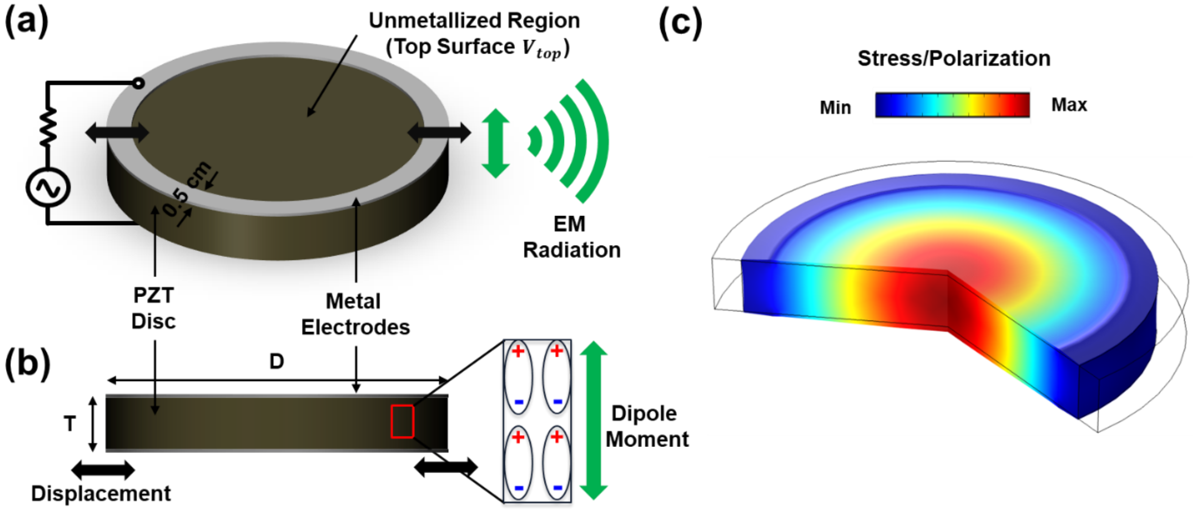

Fig. 4.1. Mock-up of dilation mode piezoelectric antenna. (a, b) The 3D view and the side view of the laterally vibrating piezoelectric disk antenna with the displacement and resulting dipole moment emphasized. (c) Fundamental dilation resonance mode showing the stress distribution at resonance formed by the acoustic standing wave.

PADA modeling requires a multidisciplinary understanding of both piezoelectricity, electromagnetics and coupling between the electrical and the mechanical domains. Modeling of the coupled physics is achieved by using FEM available from COMSOL Multiphysics which couples these domains in the "piezoelectric devices" toolbox. This toolbox solves the piezoelectric constitutive equations either in its stress-charge or strain-charge forms. Such a model can be used to determine the resonance frequency of the structure using eigenfrequency simulations followed by frequency-domain simulations to find out parameters such as induced stress/strain, the velocity at the edge of the disc, internal polarization, surface voltages, and admittance. Two types of boundary conditions (BC) need to be set to run frequency-domain simulations; electrical BC and mechanical BC. Electrically, an arbitrary voltage amplitude is applied to the top electrode while the bottom electrode is grounded (all the parameters scales linearly with voltage) and all other surfaces are electrically floating. On the mechanical side, a free BC is assigned to the whole PZT disk to reduce any anchor damping and a material damping is assigned to PZT. The internal polarization (charge density) can then be used to calculate the polarization current from which the fields and efficiency can be calculated. PZT piezoelectric properties are supplied by the vendor (Appendix A) and input to the FEM model.

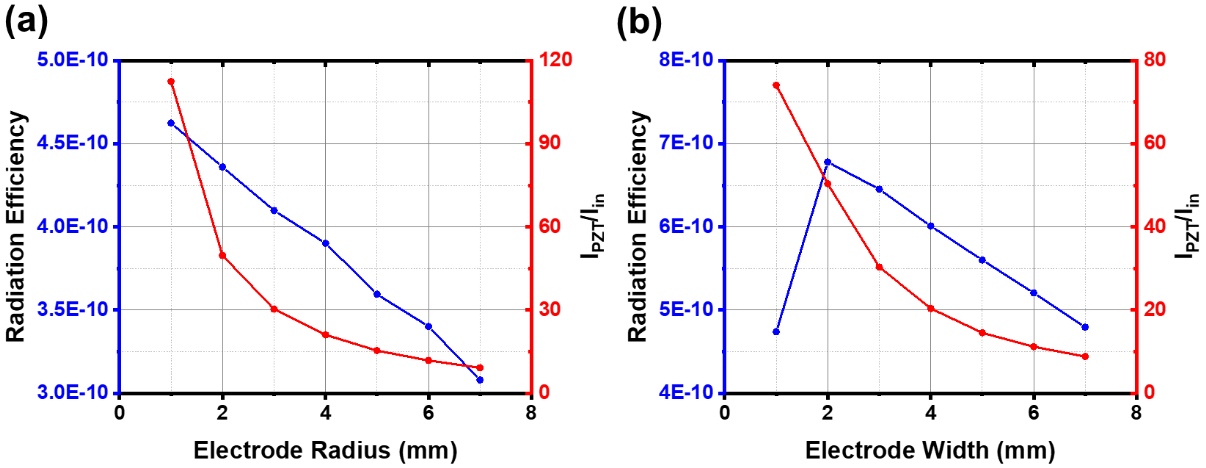

Fig. 4.2. Radiation efficiency and current ratio as a function of electrode size for (a) circular electrodes at the center of the resonator and (b) ring electrodes around the edge of the disk resonator.

Once a material is chosen, the PADA geometry is optimized to maximize efficiency. For the disk PADA prototype, the diameter is set to 8 cm to achieve a resonance frequency near 30 kHz, and then the thickness of the disk is chosen to be 1 cm to maximize the size of the PADA within the volume constraint. The design of the electrodes is then optimized to maximize efficiency using COMSOL Multiphysics.

Although (2.15) and (3.21) provide an FoM for choosing a piezoelectric material for efficient radiation, they are based on the assumption that all of the generated polarization leads to radiation. As discussed in Section 3.2, some amount of the polarization is shielded by the driving electrodes, and therefore careful consideration of the electrode configuration must be made between optimally exciting time-varying strain (high electromechanical coupling) and maximizing the radiation achieved by that strain. Although electromechanical coupling K^2 is defined by the material properties, it relies on an external force or electric field in order to couple energy to the other domain. In general, the electric field from the electrodes is not uniform across the piezoelectric resonator, and therefore the effective coupling from the electrical to the mechanical domain is diminished where the electric field is smallest. Therefore, an effective electromechanical coupling coefficient k_t^2 of a resonator where $k_t^2 \leq K^2$ is defined which is dependent on the electrode boundary conditions. For the disk resonator using the d_{31} coefficient, k_t^2 is maximized by configuring the electrodes to maximize the electric field in the z-direction across the piezoelectric disk. The fields are maximized when the top and bottom surfaces and completely metalized and a time-varying voltage is applied across the electrodes. However, as shown in Fig. 3.3, full metallization completely neutralizes the effective piezoelectric current and radiation, and therefore maximum k_t^2 results in minimum radiation. Maximum radiation requires small electrodes, to minimize the neutralization of the effective piezoelectric current. For a fixed electrode area, maximum k_t^2 is achieved configuring the electrode to apply the external electric field across the highest stress portion of the resonator. As shown in Fig. 4.1, disk resonators operating in the fundamental dilation mode exhibit greatest stress at the center which tapers off to zero at the edges. However, since piezoelectric polarization is proportional to stress (3.1), the effective current is also maximum at the center of the disk and positioning the electrodes there neutralizes the highest piezoelectric current density portion of the resonator. Therefore, the electrodes must be optimized to promote both high electromechanical coupling and efficient radiation.

In order to determine the most efficient electrode configuration, various electrode dimensions on the outer ring (lowest polarization neutralization) and center (highest electromechanical coupling) of the PZT disk were compared. The efficiency and current ratios for different electrode diameters (center electrode) and widths (edge electrode) are shown in Fig. 4.2. The current ratio is dependent solely on electrode size, with smaller electrodes increasing the radiation from PZT relative to the input current and therefore decreasing the noise from the driving circuitry. However, as shown in Fig. 4.2b, if electrodes are too small, the total radiation efficiency is diminished due to the diminished coupling of energy into the electromechanical resonator. Maximum radiation efficiency is achieved with an ~2 mm wide ring electrode around the edge of the disk. Based on the manufacturer's provided Q of 2000, the simulated $R_m \approx 150\ \Omega$. In order to demonstrate the potential to match the disk PADA to a 50 Ω system, the width of the electrode is increased to 5 mm which decreases R_m to ~45 Ω according to (2.3). The increased electrode size results in a 21% decrease in radiation efficiency as shown in Fig. 4.2, but an increased mismatch efficiency of 33% and therefore the total efficiency is ~8% greater with 5 mm electrodes compared to 2 mm electrodes.

4.1.2 Rod PADA Design

The PZT disk resonator represents an initial proof of concept of a VLF PADA and is therefore constrained to operate near 30 kHz in order to maximize the radiation efficiency from (2.15). However, as shown in Table 3.2, other materials and modes present the potential for a higher FoM but were neglected in the proof of concept due to sizing availability. In order to experimentally verify the potential for scaling efficiency using the parameters in (2.15), a second rod PADA is designed using the same PIC181 PZT material to operate in the thickness extensional mode using the d_{33} coupling coefficient. The maximum commercially available thickness for the PIC181 PZT is 2.5 cm, corresponding to a thickness resonance near 70 kHz. Due to the Poisson ratio, both the dilatational mode disk and the thickness extensional rod experience stress in the lateral and thickness directions simultaneously and it depends on the geometry as whether more energy is coupled into the dilatational or thickness mode. Therefore, in order to maximize efficiency, the radius of the disk should be chosen to have the highest possible coupling. The coupling K^2 for different rod radii was simulated using COMSOL Multiphysics as shown in Fig. 4.3. Although a rod radius of 0.8 cm yields the highest coupling, a radius of 1 cm was chosen instead since it results in a negligible decrease in coupling while providing > 50% more volume and therefore efficiency per unit.

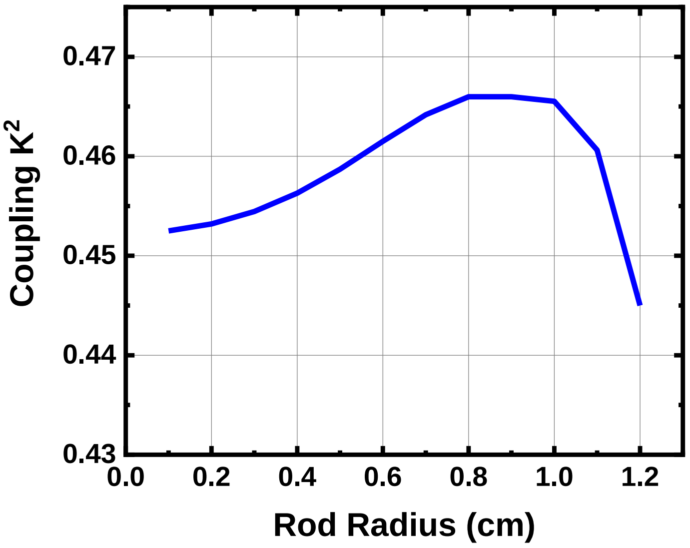

Fig. 4.3. Coupling coefficient as a function of rod radius for a PZT rod with a thickness of 2.5 cm.

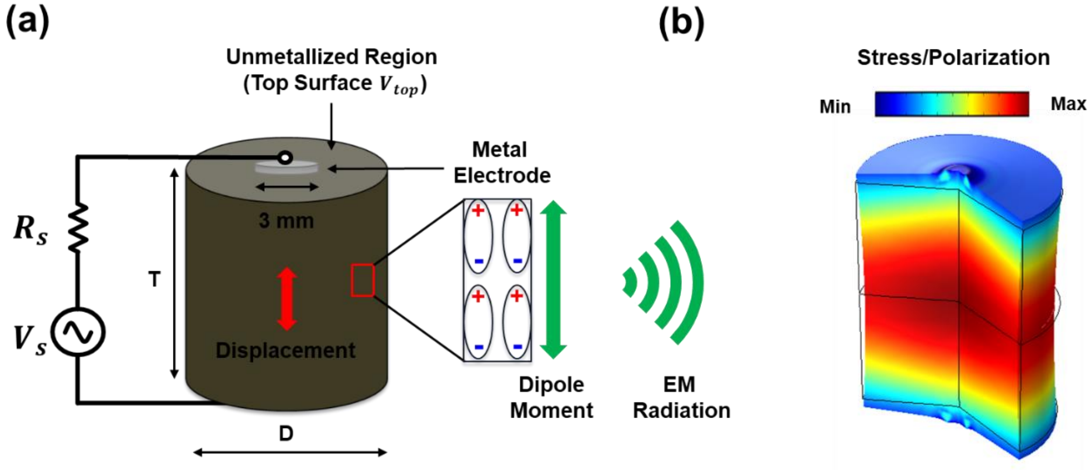

Fig. 4.4. Mock-up of thickness extensional mode piezoelectric antenna. (a) 3D view of the thickness extensional vibrating piezoelectric rod antenna with the displacement and resulting dipole moment emphasized. (b) Fundamental thickness extensional resonance mode showing the stress distribution at resonance formed by the acoustic standing wave.

A mock-up of the thickness extensional mode of the rod resonator is shown in Fig. 4.4a which the stress profile shown in Fig. 4.4b. For the fundamental thickness mode, both stress and polarization are maximum in the center of the disk and taper off toward the top and bottom. Since the stress is nearly constant in the lateral direction, no advantage is gained by placing the electrodes around the edge like with the disk resonator. Instead, the rod exhibits superior efficiency when the electrode

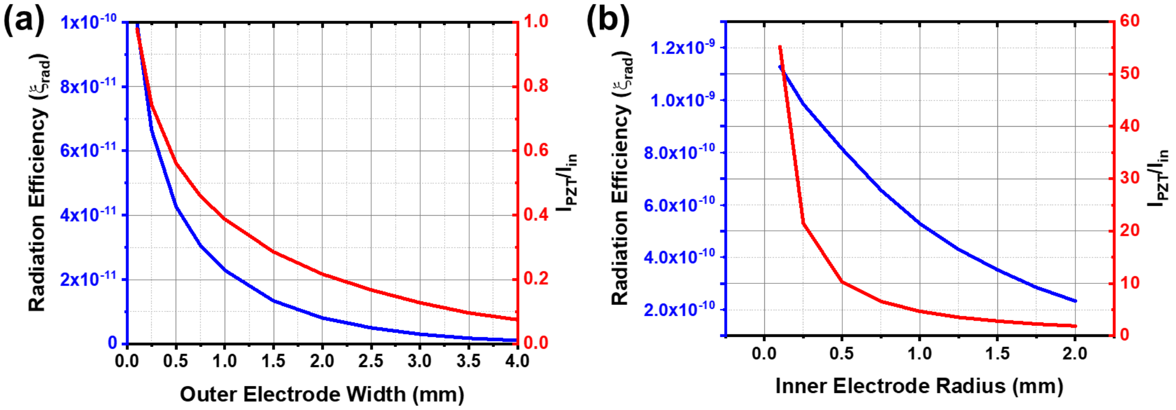

Fig. 4.5. Radiation efficiency and current ratio as a function of electrode size for (a) circular electrodes at the center of the resonator and (b) ring electrodes around the edge of the disk resonator.

is placed at the center of the top and bottom surface, as shown in Fig. 4.5. The increased aspect ratio results in a larger fringing field and therefore the rod exhibits a smaller I_{PZT}/I_{in} ratio than the disk despite having a larger efficiency since the current ratio is dependent on the effective electrode area from fringing relative to the total area.

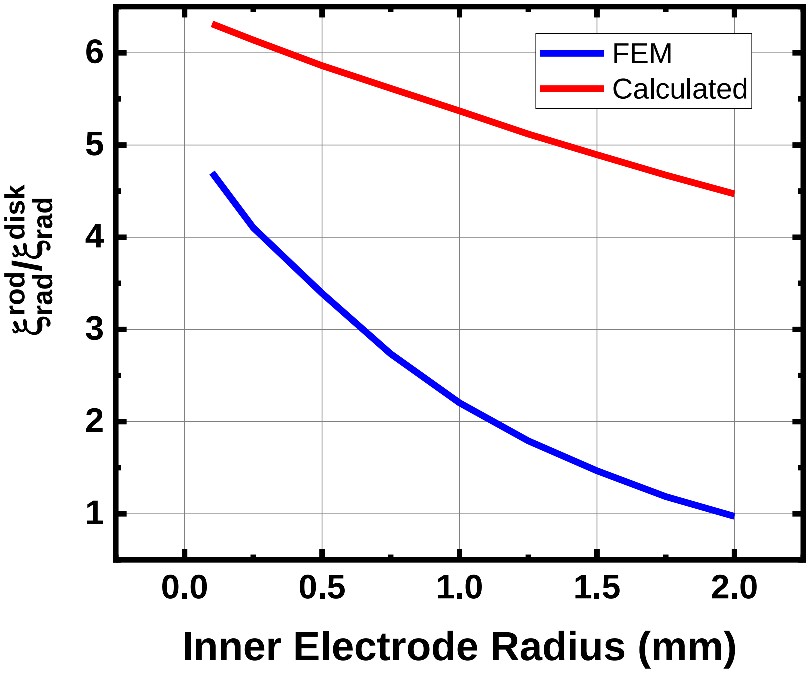

Fig. 4.6. Ratio of the radiation efficiency of the rod PADA compared to the disk PADA as a function of electrode size.

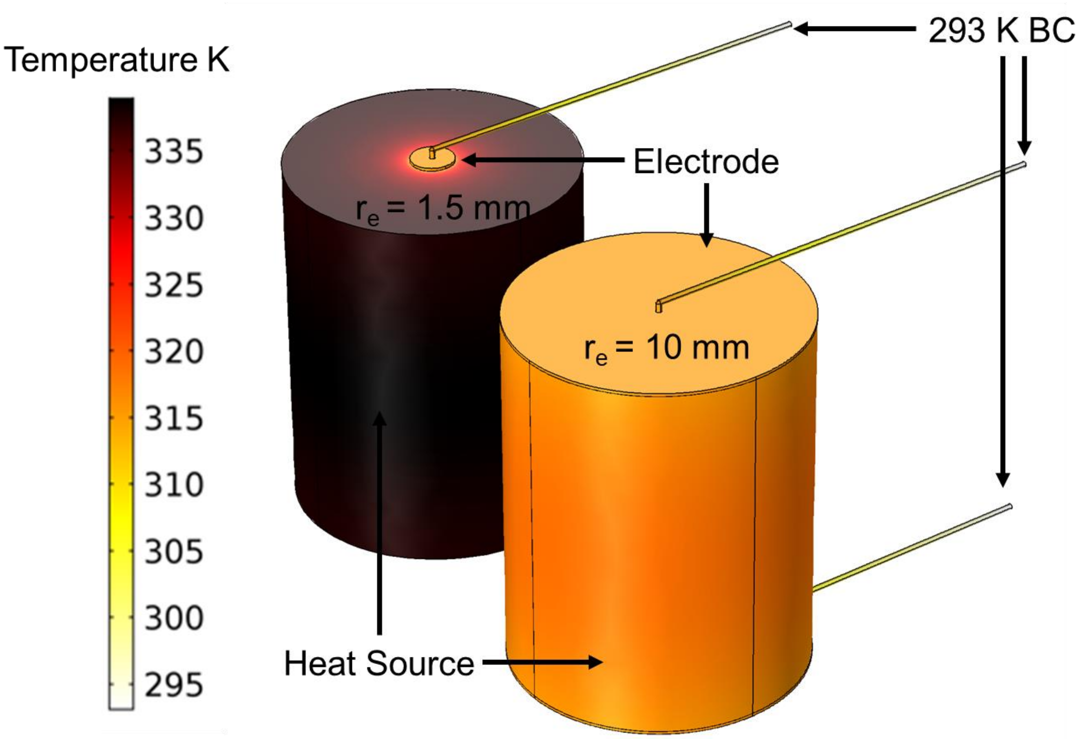

Fig. 4.7. Thermal nonlinearity in the PZT rod PADA with ~ 20 μm thick silver electrodes at different power levels. Forward frequency sweep of (a) rod PADA with full electrode coverage on the top and bottom surface and (b) rod PADA with 8 mm diameter electrodes in the center.

The increased fringing also results in diminished efficiency compared to the efficiency calculated using (2.15) which neglects fringing fields. The ratio of the calculated (no fringing) to simulated (includes fringing) efficiency gain of the rod PADA compared to the disk is plotted in Fig. 4.6 as a function of electrode size. The efficiency values are calculated from the unmetallized volume of PZT, with the coupling and stiffness coefficients provided in Table 3.2, and the quality factors of the disk and rod being 2000 and 1000 respectively. The diminished Q from the rod is based on experimental measurements and is likely due to additional complexity in fabricating and poling the thicker PZT. From Fig. 4.6, fringing fields can significantly decrease the efficiency predicted from the material constants in (2.15) and result in a diminished effective FoM.

In addition to efficiency considerations, the size of the electrode is also important for thermal power handling. As discussed in Section 3.3, piezoelectric resonators can exhibit nonlinear behavior at elevated temperatures which limits the total radiation. Since the metal electrodes made from highly conductive materials like silver or gold can have thermal conductivities of more than 300 W/m-K, increasing the size of the electrode can significantly increase the effective thermal conductivity of the resonator as shown in Fig. 4.7. The increased effective conductivity from larger electrodes allows the PADA to handle more input power as shown in Fig. 4.8, and therefore, potentially radiate greater power despite the loss in efficiency. In order to balance the high efficiency from small electrodes, and the increased power handling of larger electrodes, a 3 mm diameter electrode was chosen for the rod PADA which resulted in a simulated R_m of 340 Ω. Since the purpose of the rod resonator is to experimentally verify PADA design for increased radiation efficiency and to increase the total radiation measurement distance, the R_m of the rod PADA is not optimized to a 50 Ω system. Instead, as will be discussed in Section 4.4, incorporating eight PADA elements in a parallel array configuration results in an effective load resistance of ~50 Ω, resulting in high matching efficiency without sacrificing the radiation efficiency of individual elements.

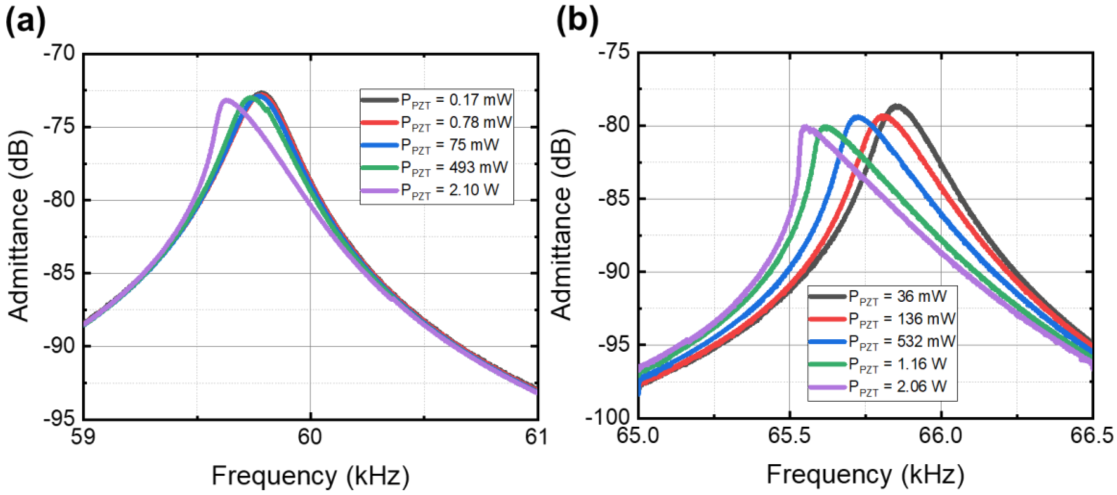

Fig. 4.8. Thermal nonlinearity in the PZT rod PADA with ~ 20 μm thick silver electrodes at different power levels. Forward frequency sweep of (a) rod PADA with full electrode coverage on the top and bottom surface and (b) rod PADA with 8 mm diameter electrodes in the center.

4.2 ADMIRE Efficiency Relative to ESA

Table 4.1 Efficiency Comparison Between PADAs and Equivalent ESA

Disk PADA Parameters

d_{31}	C_{11}^{E}	A_{PZT}	L_{PZT}	Q_{PZT}	k_t^2	C_o
108* pC/N	152.3* GPa	38.5 cm^2	1 cm	1340	3.7 %	1.8 nF

ESA Parameters

L_{ESA}	r_{ESA}	A_{ESA}	σ_c	$Q_{inductor}$	$\xi_{tot,calc}^{rel}$	$\xi_{tot,FEM}^{rel}$
8 cm	0.5 cm	πr_{ESA}^2	5.9×10^7 S/m	200	6700	6600

Rod PADA Parameters

d_{33}	C_{33}^{E}	A_{PZT}	L_{PZT}	Q_{PZT}	k_t^2	C_o
253* pC/N	134.1* GPa	3.1 cm^2	2.5 cm	1120	19 %	21 pF

ESA Parameters

L_{ESA}	r_{ESA}	A_{ESA}	σ_c	$Q_{inductor}$	$\xi_{tot,calc}^{rel}$	$\xi_{tot,FEM}^{rel}$
2.5 cm	1 cm	πr_{ESA}^2	5.9×10^7 S/m	200	930	280

PADA antenna parameters are either characterized by the manufacturer (*) or measured post-fabrication.

The efficiency of the two ADMIRE antennas relative to an ideal dipole is calculated as done in Chapter 2, using the properties shown in Table 3.2. The ESA is assumed to be made from copper with bulk conductivity σ_c and matched with an inductor with a Q of 200 to a source with $R_s = 50\ \Omega$. The piezoelectric coupling and stiffness parameters are provided by the vendor, and are imported into the multiphysics FEM, while Q, k_t^2, and C_0 are determined experimentally. For the rod resonator, the experimental values in Table 4.1 represent the average measured values across eight elements that were subsequently built into an array. Relative efficiency values are provided both from calculations using (2.15) as well as FEM simulation with the simulated value yielding a lower efficiency due to accounting for fringing fields as shown in Fig. 4.6. Despite yielding a greater radiation efficiency than the disk PADA, the rod PADA is less efficient relative to a comparable ESA primarily due to the increased electrical antenna efficiency at higher frequencies and not being geometrically optimized to match to a 50 Ω source.

4.3 Fabrication and Characterization

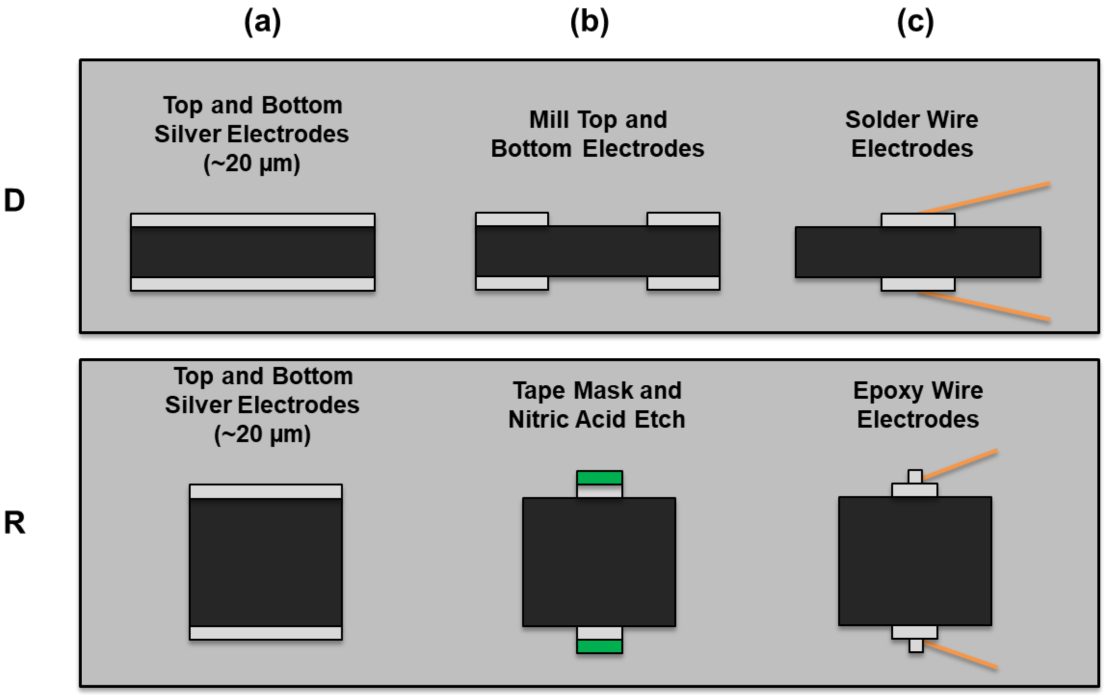

Fig. 4.9. PADA Fabrication. (a) Both the disk (D) and rod (R) geometries come fully plated on the top and bottom surfaces with silver electrodes. (b) The electrode is patterned either via machining with an end mill (D) or etching in nitric acid (R). (c) Finally, wires are either soldered (D) or epoxied (R) to the electrodes to connect to the electrical driving circuitry.

To demonstrate the PADA antennas, prototypes of both the disk and rod resonators are created. The PZT disks and rods are commercially fabricated by Physik Instrumente (PI) and made from their PIC181 material [131]. The commercial disks have an 8 cm diameter and a 1 cm thickness while the rods have a 1 cm diameter and 2.5 cm thickness. Both types of PZT shapes are sold with both the top and bottom surfaces fully metalized with ~20 μm of silver which is used to pole the PZT in the thickness direction. The fabrication process is depicted in Fig. 4.9. Patterning of the silver electrodes for the disk is conducted using an end mill to remove the interior metal until only the desired 0.5 cm ring electrode along the edge remains. Two wire leads are split from a BNC cable and soldered to the top and bottom metal surfaces to provide electrical excitation, with the lead lengths minimized to reduce near-field radiation from the current loop as shown in Fig. 4.10a. For the rod resonators, a 3 mm diameter electrode is etched into the center of the top and bottom surfaces using nitric acid. The electrode is patterned using an acid-resistant tape cut into a 3 mm

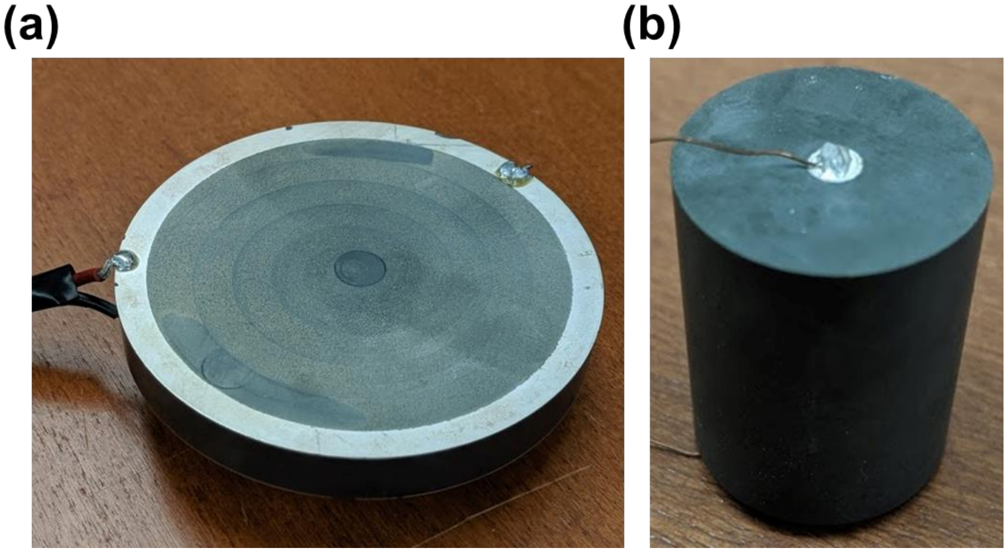

Fig 4.10. Fabricated PZT PADA (a) disk and (b) rod.

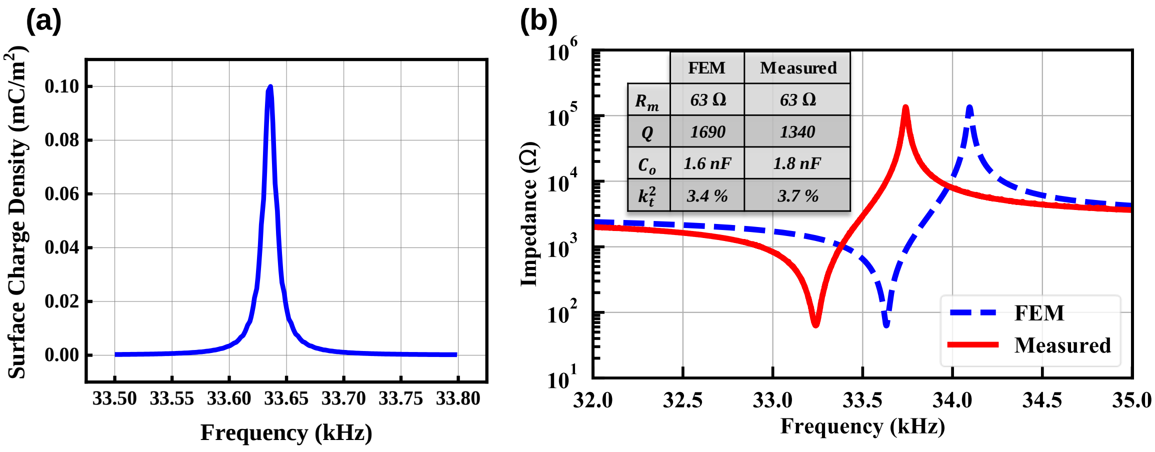

Fig. 4.11. Electrical response of the PZT ADMIRE. (a) Simulated surface charge density from the strain generated dipole moment of the PZT with an applied voltage amplitude of 1 V. Charge density and surface voltage are amplified at resonance due to the high Q of the ADMIRE resonator. (b) Simulated and measured impedances at the input terminals (electrodes) of the PZT disc.

circle, which is positioned by hand in the center of the electrode. Although a smaller diameter electrode yields more efficient radiation, electrodes smaller than 3 mm in diameter were prone to delamination during the fabrication and assembly process. Wires were soldered to the disk electrodes in order to connect to the driving circuitry. For the smaller 3 mm diameter electrodes, the heat in the soldering process sometimes led to the delamination of the electrodes, and so a

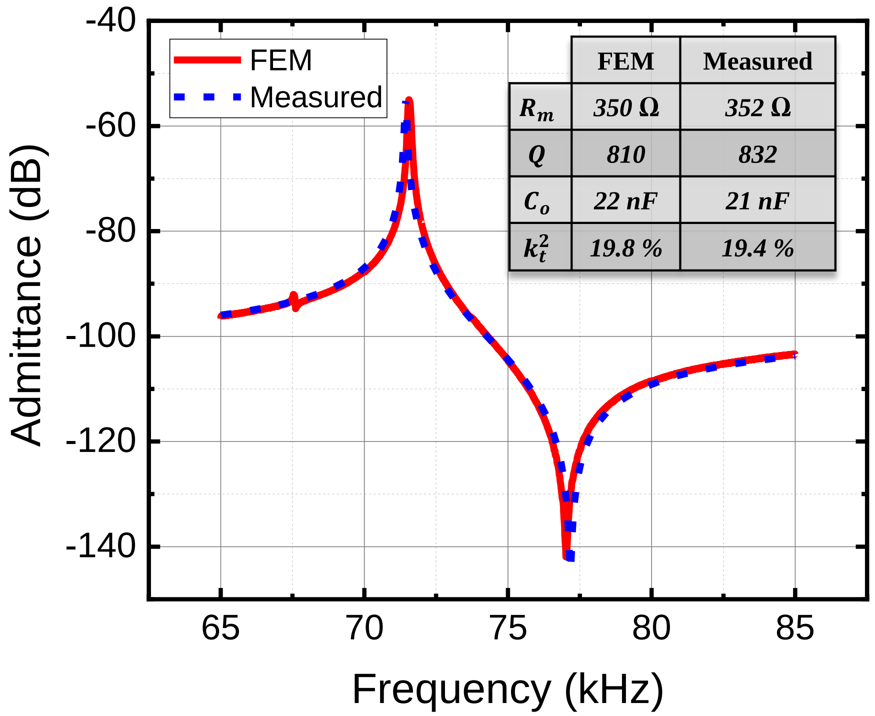

	FEM	Measured
R_m	350 Ω	352 Ω
Q	810	832
C_o	22 nF	21 nF
k_t^2	19.8 %	19.4 %

Fig. 4.12. Simulated and measured impedances at the input terminals (electrodes) of the PZT rod.

conductive silver epoxy which cures at room temperature was used to connect the electrodes to the external circuitry.

Characterization of the PZT is conducted by connecting a Tektronix AFG3152C function generator directly to the electrodes via BNC cable. An Agilent E4445A spectrum analyzer connected in series with the PZT resonators is then used to characterize the impedance of the PZT as a function of frequency, from which the motional resistance, electromechanical coupling (k_t^2) and mechanical quality factor are extracted as shown in Fig. 4.11 and Fig 4.12 During testing, the PZT resonators operate with mechanically free boundary conditions, such that all moving surfaces are free to move without constraint which theoretically results in the lowest damping and highest Q. The mechanically free boundary condition is achieved by resting the bottom center of the resonator on a small piece of foam. Multiple mounting configurations were considered, with the small foam base ultimately chosen for simplicity as it was experimentally verified to not reduce resonator Q. For the array, in order to ensure that all array elements are vertically aligned, the rod elements are placed on small wooden runners. Input power to the PZT disk is characterized by

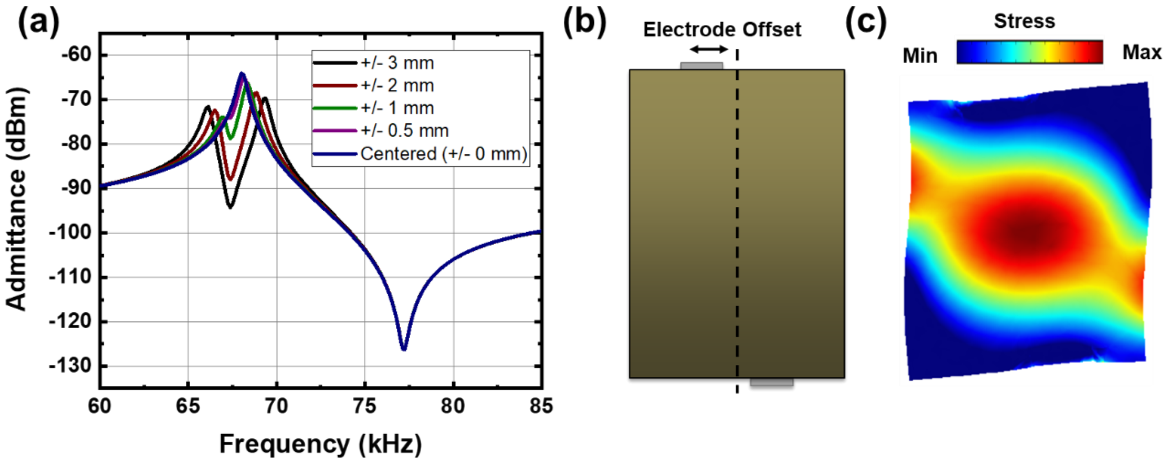

Fig 4.13. Spurious antisymmetric mode due to electrode misalignment. (a) Simulated admittance as a function lateral electrode separation. (b) Mock-up of resonator cross-section and laterally misaligned electrodes. (c) FEM simulation of the shear mode that that arises due to asymmetric applied electric fields.

adding an Agilent MSO7104B oscilloscope with 1 MΩ impedance in parallel with the disk with the power dissipation measured from the voltage drop across the PZT.

FEM simulation of the finalized disk PADA design shown in Fig. 4.10. A 0.5 cm wide ring electrode is chosen based on Fig. 4.2 to yield the highest radiation efficiency. The disk diameter and height of 8 cm and 1 cm respectively are chosen to yield a resonant frequency near the upper bound of the VLF band. A motional resistance of 50 Ω is designed to match with typical 50 Ω systems at the 33.6 kHz. However, measured Q is reduced by electrical loading in the driving circuit, resulting in an increase in the measured R_m of 63 Ω. Since $P_{del} = V_{in}^2/R_m$ for the PADA, the simulated Q is tuned to 1690 to achieve the same R_m and input power for efficiency comparison.

The FEM simulated response of the PZT rod PADA is shown in Fig. 4.12. A 3 mm diameter circular electrode is chosen to balance peak radiation efficiency and increased power handling in order to extend the measurement range. A small spurious resonant mode can be seen near 67.5 kHz due to slight misalignment of the top and bottom electrodes (< 0.2 mm) which are patterned by hand. Lateral misalignment of the top and bottom electrodes causes an asymmetric electric field between the electrodes, which can lead to the generation of a shear resonant mode as shown in Fig. 4.13 for misalignment greater than 1 mm. Due to the small electrode misalignment in the fabricated resonator, the spurious mode is sufficiently small and off resonance to not affect the PADA performance at resonance.

4.4 PADA Arrays

As seen in Table 4.1, PADAs have the potential to greatly exceed the efficiency possible from electrical antennas. As higher FoM materials become commercially available at suitable sizes for VLF and LF resonators, the efficiency of PADAs can be expected to increase by multiple orders of magnitude due to the extremely high coupling coefficients exhibited by relaxor type ferroelectrics such as PMN-PT. However, while piezoelectric antennas show great promise for more efficient operation in the VLF and LF frequency ranges than electrical antennas, significant progress must be made for them to be commercially viable. Since efficiency is purely a ratio of input power to output power, a PADA can exhibit high efficiency but only a small radiated power if the input power handling is limited. Maximum radiated power for PADAs is primarily capped by three mechanisms: electrical breakdown, thermal nonlinearity, and mechanical nonlinearity. For high Q, low permittivity piezoelectric antennas, electrical breakdown of the gases surrounding the antenna is usually the limiting factor [48] due to insufficient confinement of the fields produced by the piezoelectric polarization. Due to the high permittivity of PZT, the rod and disk PADA operate well below the breakdown limit, and instead the maximum radiated power is primarily limited by thermal nonlinearity as shown in Fig. 4.8. As discussed in Section 4.1, power handling can be increased by optimizing the resonator and electrode geometry to increase thermal conductivity, but sometimes at the cost of decreased efficiency. Alternatively, the power handling can be increased by increasing the volume and thus heat capacity, of the resonator. However, since both resonant frequency and electromechanical coupling are geometry dependent, increasing the volume may come at the expense of efficiency or the desired operating frequency. Instead, total radiated power can be increased without sacrificing efficiency or operating frequency by arraying multiple PADA elements together. Arraying N elements together scales the effective PADA volume, where $V_{eff} = NV_{element}$, and thus both the radiation efficiency and power handling since efficiency scales with volume (2.15) and the total power dissipated power can be divided among the individual elements.

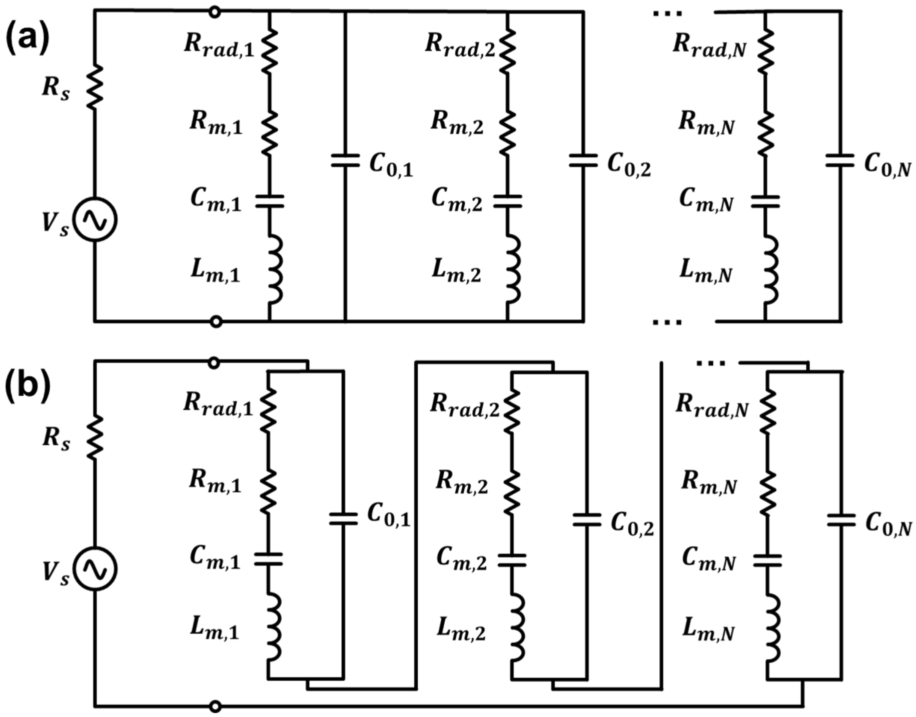

Fig. 4.14. MBVD equivalent circuit models for PADA arrays in (a) parallel and (b) series.

Therefore, in order to increase the efficiency of the rod PADA, an array of eight rod elements is implemented. Although the thickness extensional rod is more efficient compared to an equivalent ESA than the dilutional mode disk due to the higher d_{33} coefficient, due to the smaller size of the rod, a single rod element is approximately as efficient as a single disk element since $V_{disk} = 6.4V_{rod}$ and radiation efficiency scales with volume as shown in (2.15). Furthermore, the smaller size results diminished power handling, and thus the total radiation expected from the rod PADA is less than the disk PADA despite being more volumetrically efficient. The PADA elements can be arrayed in either a series configuration or a parallel configuration as shown in Fig. 4.14, with each configuration having pros and cons.

When PADA elements are arrayed in parallel, the same potential is applied across all devices simultaneously as shown in the equivalent circuit model in Fig. 4.14b. Since each motional branch is connected directly to ground, each individual resonator will its own resonant frequency at $\omega_0 = \sqrt{1/L_{m,n}C_{m,n}}$ where *n* denotes the properties of the nth resonator in the array. If the individual resonators have slightly different resonant frequencies, as shown for the case of a two element array in Fig. 4.15, then the resonators cannot be driven simultaneously at their resonant frequency and some efficiency is lost due to one or both resonators being driven off resonance. Due to a narrower acoustic bandwidth, resonators with high-quality factors are more susceptible to frequency misalignment caused by variance in the fabrication process. If frequency synchronization cannot be achieved in fabrication, a reactive tuning element can be added in series with a detuned resonator in order to shift its resonance back to the operating frequency of the array as shown in Fig. 4.16. The shifted resonant frequency is:

$$f_s \approx \frac{1}{2\pi}\sqrt{\frac{C_o + C_m + C_T}{(C_T + C_o)C_m L_m}} \tag{4.2}$$

where the tuning capacitor C_T is added in series with the resonator as shown in Fig. 4.16a. The admittance response of a resonator tuned by a capacitor is shown in Fig. 4.16b, with the tuning range as a function of capacitance given in Fig. 4.16c. Therefore, tuning capacitors can be added to the frequency desynchronized resonators in the array in order to align all the resonance frequencies and maximize efficiency. However, even if all the resonant frequencies are synchronized, since resonator quality factor and thus motional resistance will likely vary due to variance in the fabrication process, the power dissipated in each resonator will not be equal. As the input power is increased to increase the radiated power, the resonators with smaller motional impedance will absorb more power and thus heat faster than the other resonators in the array. The increased temperature will result in a shift in resonance frequency, causing the array to detune. Therefore, even if frequency synchronization in fabrication can be maintained with high fidelity, PADAs comprised of high FoM materials with low quality factors such as PMN-PT are more suited to parallel array implementation since they have a wide 3 dB bandwidth and are thus less susceptible to frequency offset. Additionally, due to the inverse relationship between Q and R_m, PADA's with a high motional impedance can be easily matched to lower impedance sources since:

$$R_{array}^{parallel} = \frac{1}{\sum_{n=1}^{n=N} \frac{1}{R_{m,n}}} \tag{4.3}$$

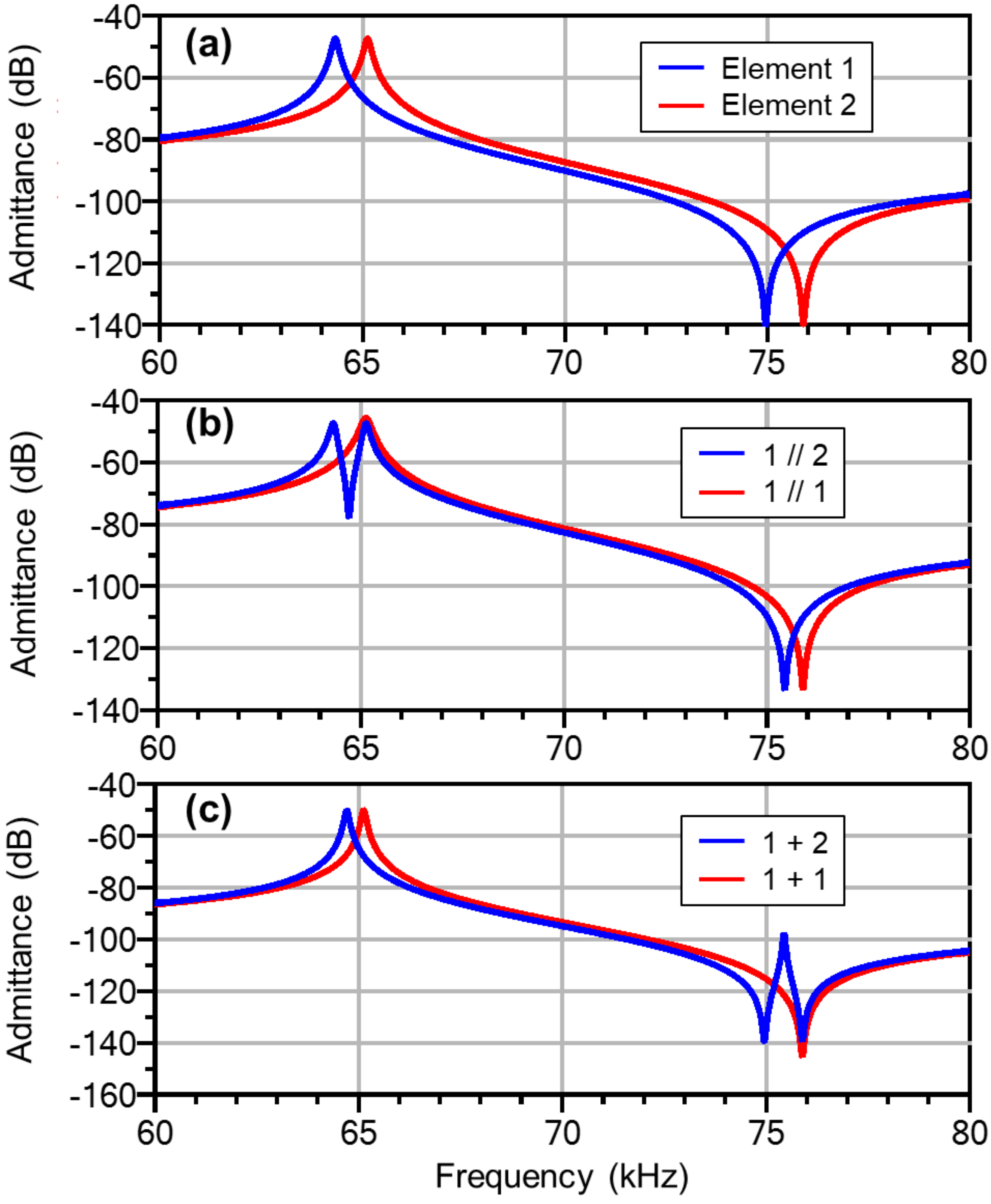

Fig. 4.15. Resonant frequency desynchronization in PADA arrays. (a) Admittance response of two individual resonators (1 and 2) with 1 kHz frequency misalignment. (b) Admittance response of an array comprised of the two frequency-shifted elements in a (blue curve) connected in parallel, compared to the parallel combination of two identical elements (red curve). (c) Admittance response of an array comprised of the two frequency-shifted elements in a (blue curve) connected in series, compared to the series combination of two identical elements (red curve).

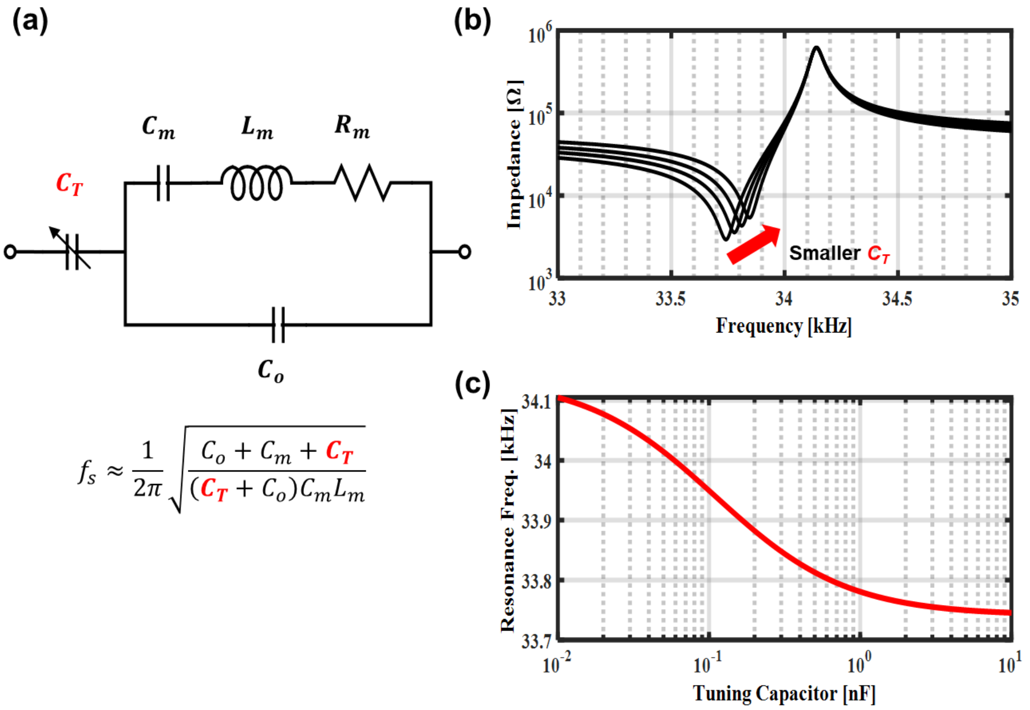

Fig. 4.16. Frequency tuning of offset resonators. (a) A tuning capacitor can be added in series to a resonator in order to shift the resonant frequency. (b) Admittance response of the tuned resonator for different values of the tuning capacitor. (c) The tuning range of the resonant frequency as a function of tuning capacitance.

Unlike parallel arrays where offsets in the resonant frequencies of individual elements result in desynchronization of the array of PADAs, the series configuration of a PADA array exhibits only a single resonance even if the frequencies of the individual components are offset as seen in Fig. 4.15c. The array resonance occurs at:

$$f_0^{series} = \frac{1}{\sqrt{L_{m,tot} C_{m,tot}}} \tag{4.4}$$

where $L_{m,tot}$ and $C_{m,tot}$ are the series combinations of the motional inductance and capacitances of the individual resonators. Therefore, a series configuration is preferred if the frequency offset of the individual elements cannot be kept sufficiently small during fabrication. Since the current in the array elements is constant, series arrayed elements will also experience non-uniform heating based on their motional resistances. Due to the series configuration, the elements will maintain frequency synchronization even if some of them start to exhibit thermal nonlinearity, and only the drive frequency needs to be synchronized to the array resonant frequency. However, one drawback

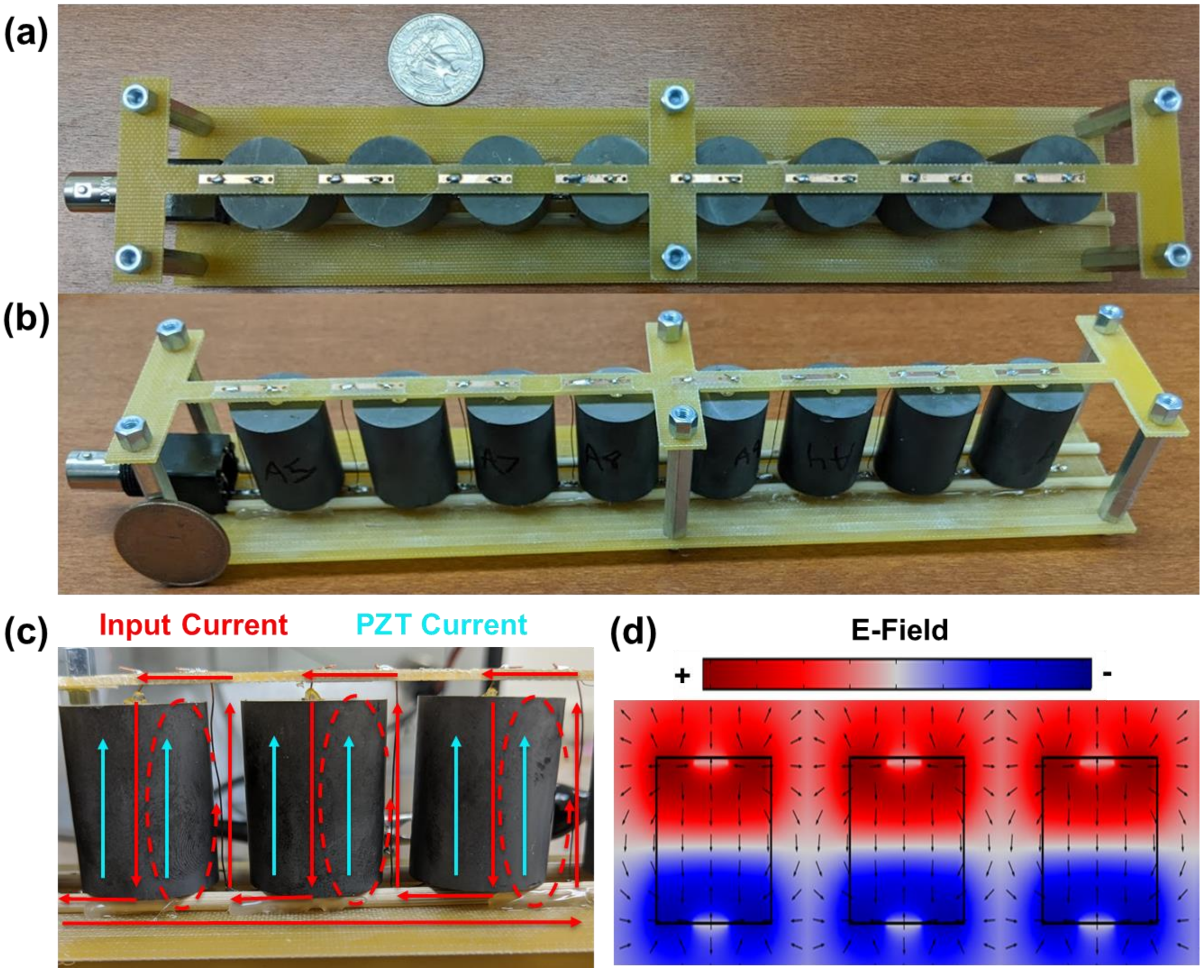

Fig. 4.17. (a) Top and (b) side view of the fabricated 8-elements series array with a quarter for size reference. (c) Array is laid out so that all current elements are in-plane, allowing the loops formed by the input current to be aligned to have a radiation null in the direction of the receiving antenna. (d) Due to the confinement of the electric fields within the PZT, array elements can be aligned in close proximity with negligible near-field coupling to adjacent resonators.

to arraying in series is that lower Q, higher motional resistance elements in the array will consume more power than the higher Q elements resulting in the most power being dissipated in the least efficient element. As the power consumed by the low Q elements increases, so does the thermal nonlinearity, and therefore the array may exhibit nonlinear behavior even when the majority of the elements in the array are operating in the linear regime. Therefore, elements in series arrays should exhibit similar quality factors in order to maximize efficiency. Series arrays are well suited for high Q resonator elements with R_m the source resistance, since:

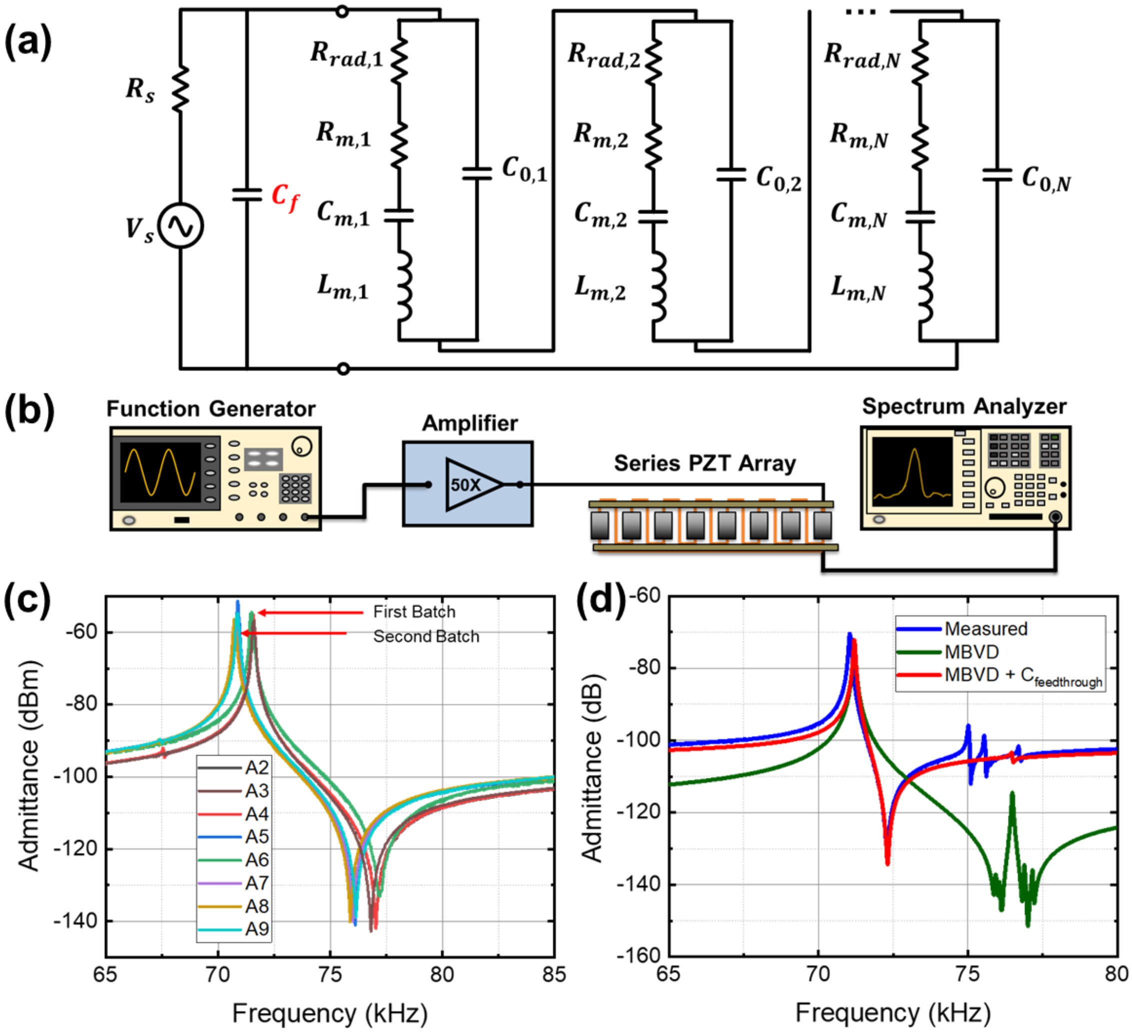

Fig. 4.18. Measured array admittance (a) Modified equivalent circuit model to account for feedthrough capacitance introduced by the array circuitry. (b) Measurement setup used to characterize the admittance response (c) Measured admittance curves of the 8 individual rod elements (c) Measured admittance curve of the entire array compared to the MBVD response of the 8 individual elements added in series. The fabricated array has additional feedthrough capacitance due to metal traces connecting the individual resonators, which causes decreases in k_t^2.

$$R_{array}^{series} = \sum_{n=1}^{n=N} R_{m,n} \tag{4.5}$$

and the arrayed elements can be impedance matched to the source without sacrificing element efficiency.

The PZT rod elements were fabricated in two batches with a ~1 kHz frequency shift between the two batches likely due to variance in fabrication. Therefore, to synchronize the frequencies, a prototype eight-element series array formed from rod PADAs is designed in order to demonstrate the potential for extending the measurement range. The fabricated array is designed to minimize radiation from the input circuitry toward the receiver. As shown in Fig. 4.6, the ratio of the PZT current to the input current for a rod PADA with a 3 mm electrode is only 2.8, and therefore the input current can be a significant source of noise in the measurement. In order to reduce the input noise, the lengths of the electrical connections were minimized by spacing the elements with 5 mm separation. Due to the large field confinement within the high permittivity PZT, as well as the low radiation efficiency of the rod PADAs, the coupling between devices has a negligible impact on device performance. A horizontal linear array was opted for stability, and the electrical connections were aligned so that the input current elements are in plane with the PZT current as shown in Fig. 4.17. The input currents between adjacent elements form a small current loop as shown in Fig. 4.17b, and the total array is oriented so that all current loops are orthogonal to the receiving antenna and thus radiate a null in that direction.

The measured admittance curves of the array elements are shown in Fig. 4.18. First, the 8 individual PADA rods are measured separately as shown in Fig. 4.18c using the measurement setup in Fig. 4.18b. The rods used for building the array were ordered in two separate shipments, and a significant frequency shift can be seen between the two batches. The response of the total fabricated array is shown in Fig. 4.12d and is compared to the extracted array response comprised of the series combination of the MBVD equivalent circuits for the eight individual elements. A significant feedthrough capacitance (12 pC), depicted in Fig. 4.18a, is introduced in parallel with the measured array admittance due to the metal traces shown in Fig. 4.17a which decreases the k_t^2 of the array. However, PADA radiation is independent of k_t^2, and therefore the prototype array is not optimized to decrease the feedthrough capacitance.

The thermal nonlinearity of the array is characterized using a Polytec OFV-5000 laser vibrometer to measure the velocity of the edge of the resonator. Edge velocity is measured at the center of the resonator as shown in Fig. 4.19a where lateral displacement is largest. The nonlinearity of a single array element is shown in Fig. 4.19b as a function of input power to the array. For a 5 W input, the velocity, and thus radiation, is reduced by ~1/3 from the expected linear response due to the

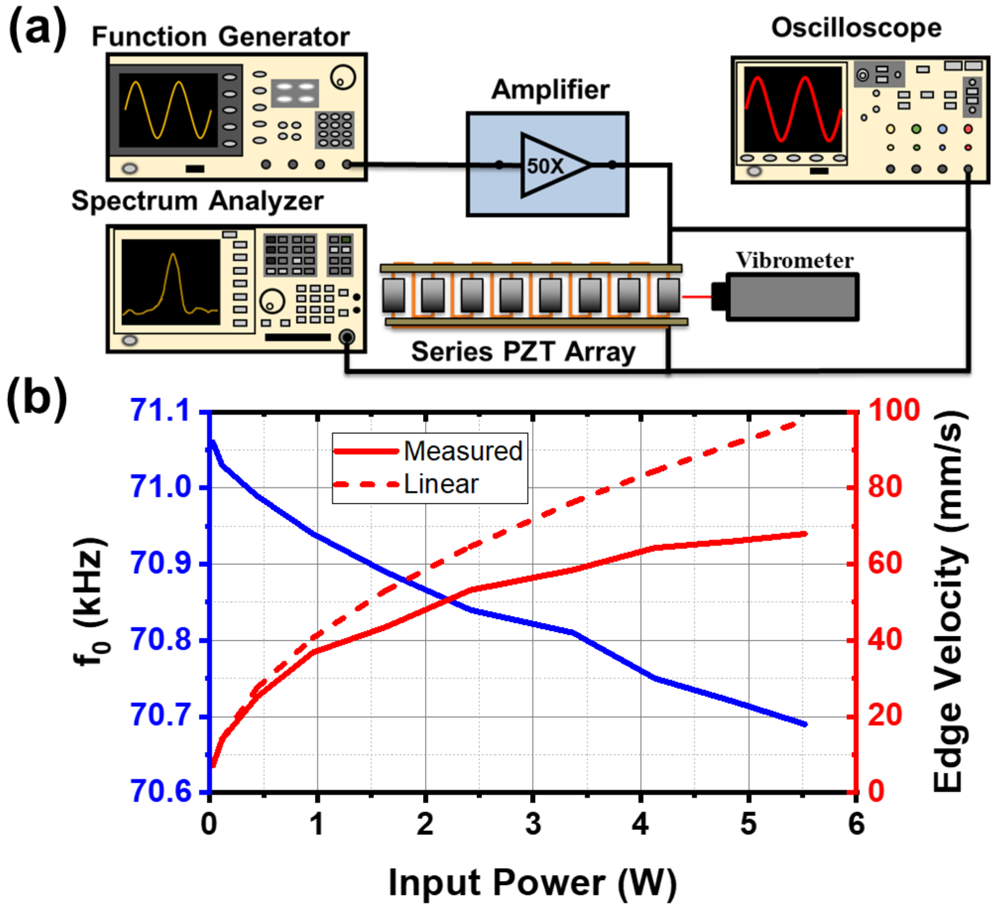

Fig. 4.19. Thermal nonlinearity in 8-element series array. (a) Mock-up of the measurement setup. A laser doppler vibrometer is used to measure the lateral displacement at the center of each rod element, while spectrum analyzer and oscilloscope are used to characterize the input power to the array. (b) Measured nonlinearity in the edge velocity and thus radiation and the shift in resonance as a function of input power.

nonlinearity. Due to the different motional impedances of the different rod elements, the absorbed power is non-uniform across the array, resulting in each element radiating different levels of power. Since the radiation is proportional to resonator velocity, the relative radiation for each element in the array as a function of frequency can be determined using the laser vibrometer as shown in Fig. 4.20 with a 1 W input power supplied to the array. Each device exhibits maximum mechanical displacement at the same resonant frequency due to the series configuration, but the radiation varies based on the resonator *Q* which ranges from 940 to 1370. Total array efficiency can be increased by removing the lowest *Q* elements, but at the expense of total radiated power due to the diminished power handling of the smaller array.

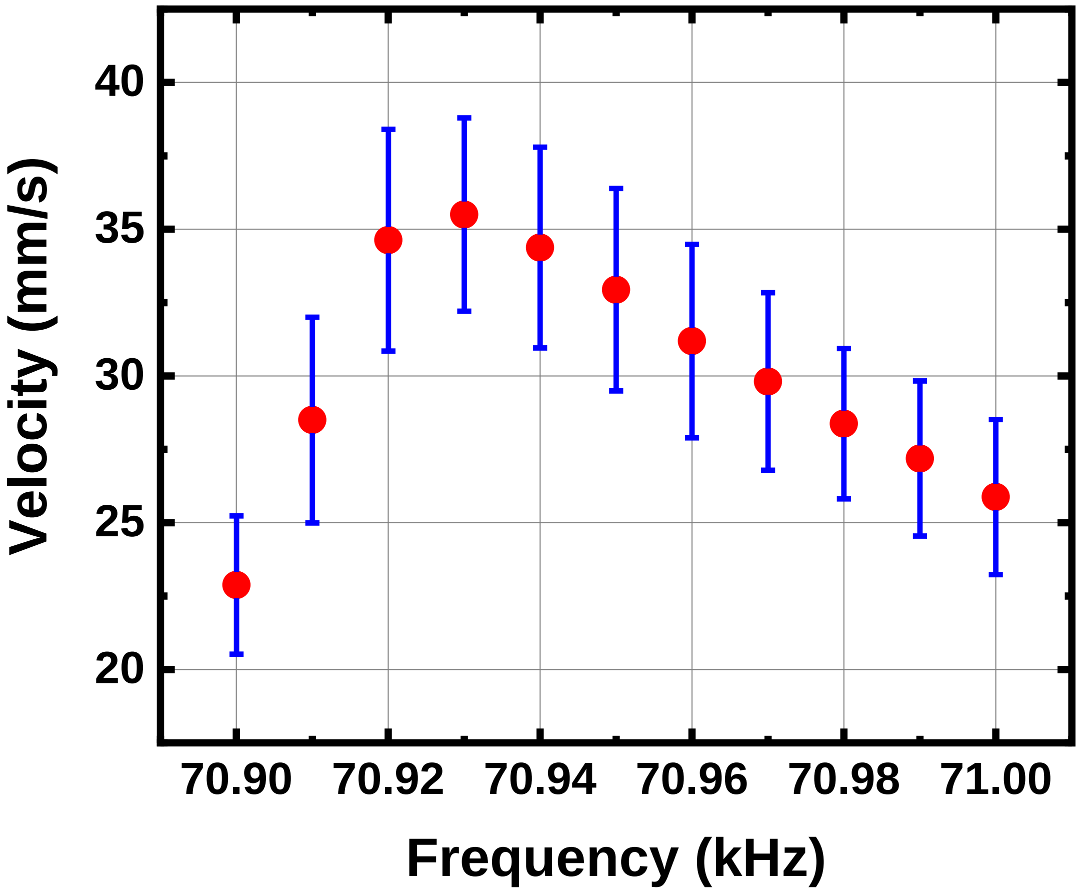

Fig. 4.20. Measured edge velocity of array elements as a function of frequency with an input power of 1 W.

In addition to arrays comprised solely of either series or parallel combinations of elements, partial combinations of series and parallel elements may yield superior performance. The frequency shifted elements can be combined in small series sub-arrays to synchronize their resonance at a single frequency. Since the resonance frequency of a series array is approximately the average of the resonant frequency of the individual elements, the resonance of the series array can be tuned to the desired operating frequency by carefully selecting the individual components. The frequency synchronized series arrays can then be arrayed in parallel so that the total power handling is not limited by the least efficient series sub-array. Additionally, by choosing the number and element size of the sub-arrays, the total array impedance can be matched to the source impedance without modifying individual element R_m.

Chapter 5: Antenna Measurement

5.1 Radiation Measurement

The radiation measurements of the PADA are complicated by the near-field confinement due to the high permittivity of the PZT. Unlike the far-field radiation of the PADA which is dependent only on the equivalent current caused by the flipping dipole moments, the reactive near-fields are confined by the large relative permittivity of PZT within the dielectric. Consequently, the reactive fields, characterized by $1/r^3$ for electric fields and $1/r^2$ for magnetic fields, are diminished in both magnitude and distance compared to an electrical antenna with equivalent radiated power. An equivalently sized 33 kHz ESA exhibits near-field dominant electric and magnetic fields up to 1 km compared to the disk and rod PADA antennas which reach their far-field dominant regime (magnetic) after approximately 1.3 meters and 5 meters respectively. Since each of the rod elements has a cross-over point at 5 m, the cross-over point for an array of rod elements is ~5 m provided that the size of the array is much smaller than the electromagnetic wavelength of the radiated signal as is the case for the eight-element array shown in Fig. 4.17. One advantage of the reduced cross-over distance is that all measured signals with a $1/r$ roll-off can be attributed solely to radiation from the PZT PADAs, since the fields from electrical traces in the driving circuit, or scattering from nearby objects will exhibit higher-order roll-off. Therefore, no complex de-embedding is required to extract the PADA radiation from the measured field.

The drawback of the reduced cross-over distance is the reduction in field strength close to the PADA due to the confinement of the reactive energy. Low permittivity PADAs or ESAs will exhibit greater field strength prior to the cross-over point than a high permittivity PADA with greater reactive field confinement even if they radiate the same power. Consequently, a less efficient antenna radiating less power such as an electrically small dipole may produce a higher measured signal-to-noise ratio in its near-field regime than a PADA radiating more power. For example, consider an ESA and PADA operating at 30 kHz with cross-over distances of 1.6 km and 5 m respectively and the PADA radiating 1000 times more power as shown in Fig. 5.1. The ESA would produce the same magnetic field at ~150 m as the PADA ($B \propto \sqrt{\mathrm{P_{rad}}}$) and a greater field at closer distances than the PADA despite $B_{PADA} > 30B_{ESA}$ at distances beyond 5 km where the near-field terms of both antennas are negligible. Therefore, PADA prototypes for long-distance

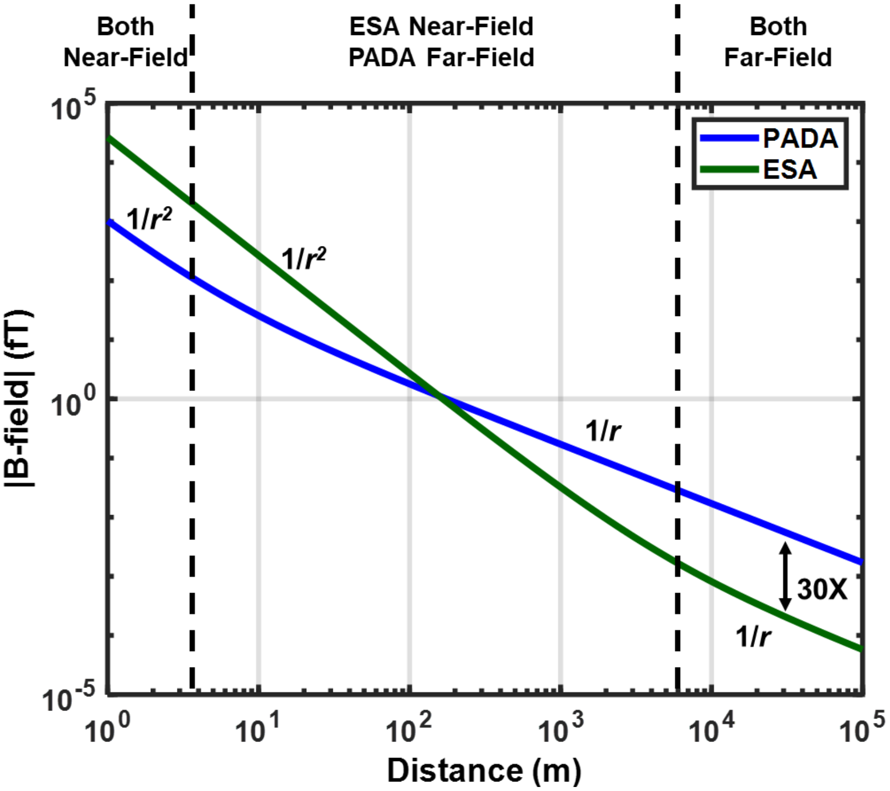

Fig. 5.1. Simulated magnetic field comparison between and ESA and PADA radiating 1000 times more power. Due to the confinement of reactive energy inside of the piezoelectric material, a PADA with a near-to-far-field cross-over distance of 5 m generates a smaller magnitude magnetic field at distances less than 150 m compared to an electrical antenna radiating 1000 times less power.

communication applications can be more difficult to characterize than less efficient antennas that exhibit larger, non-radiated reactive fields due to the smaller measured signal close to the transmitter.

In order to maximize the measured signal-to-noise ratio in the receiving loop antenna, both the PZT PADAs and the measurement setup are designed to minimize RF interference from the leads and connections so that the PZT radiation is not obscured. Since the radiation from the alternating piezoelectric dipoles inside the PZT PADAs are the only fields generated by the transmitter that exhibit a 1/r roll-off before 500 m, any fields exhibiting a 1/roll-off can be attributed solely to the PADA radiation. If the near-field noise from the current leads is greater than the near-field component of the PADA, as shown in Fig. 5.2a, the magnetic field measurement will exhibit $1/r^2$ roll-off beyond the theoretical cross-over from the PADA. Since the near-field components of both the PZT and the wires exhibit the same roll-off, and near-field measurements can be unpredictable due to scattering and coupling, it is difficult to distinguish the magnitude of the PADA radiation

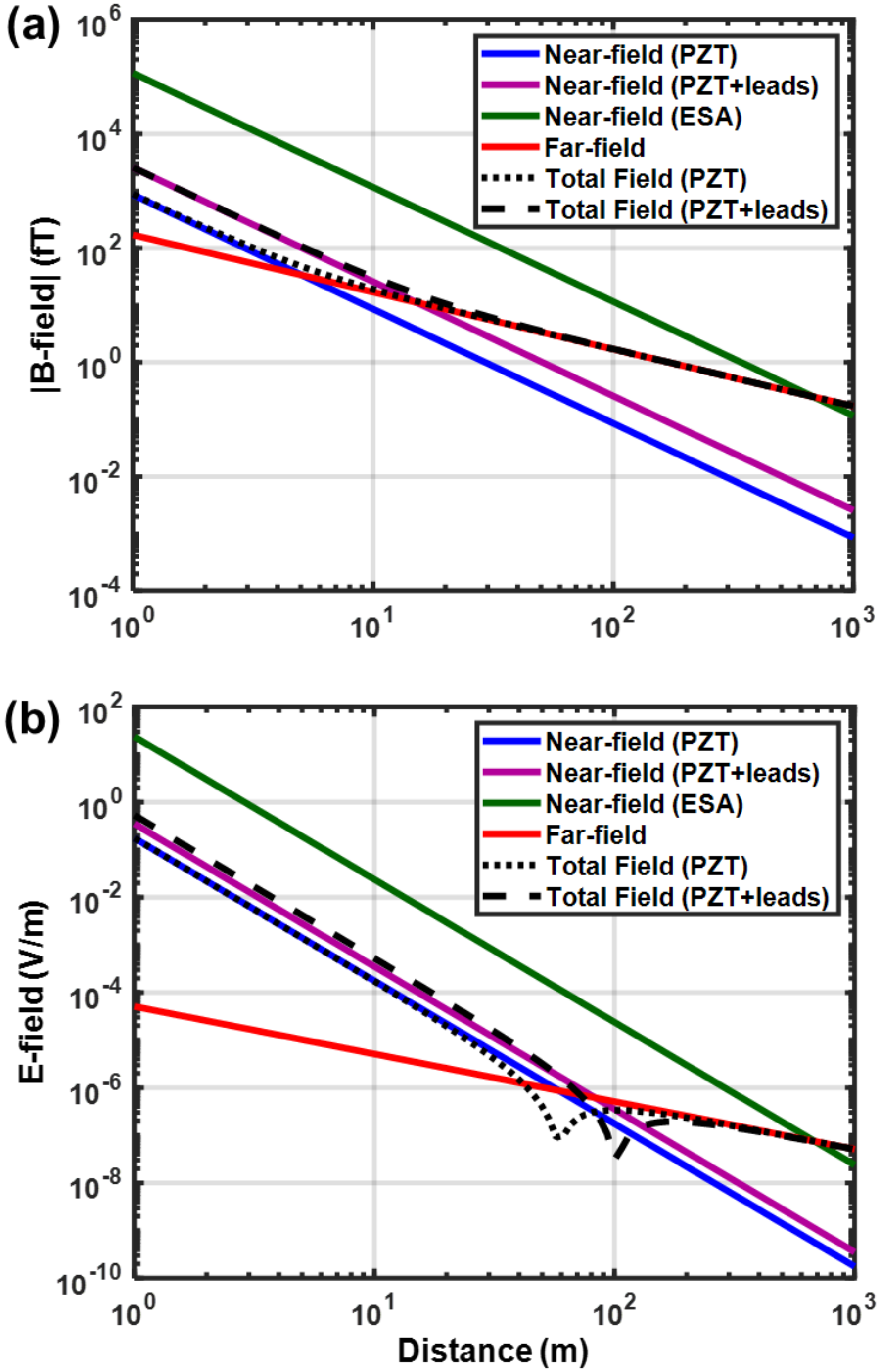

Fig. 5.2. Simulated (a) magnetic and (b) electric field roll-offs for a single PADA rod element as well as hypothetical roll-offs for the same PADA rod element with additional radiation from electrical leads. Fields exhibiting 1/r roll-off correspond solely to radiation from the PZT PADA, whereas fields exhibiting $1/r^2$ (magnetic field) and $1/r^3$ (electric field) roll-off may include contributions from non-piezoelectric sources such as electrical traces in the PADA circuitry or re-radiation from scattering objects. Fields from non-PADA radiators such as the electrical leads increase the cross-over distance, requiring measurement of the PADA radiation at a greater distance where the signal-to-noise ratio is diminished.

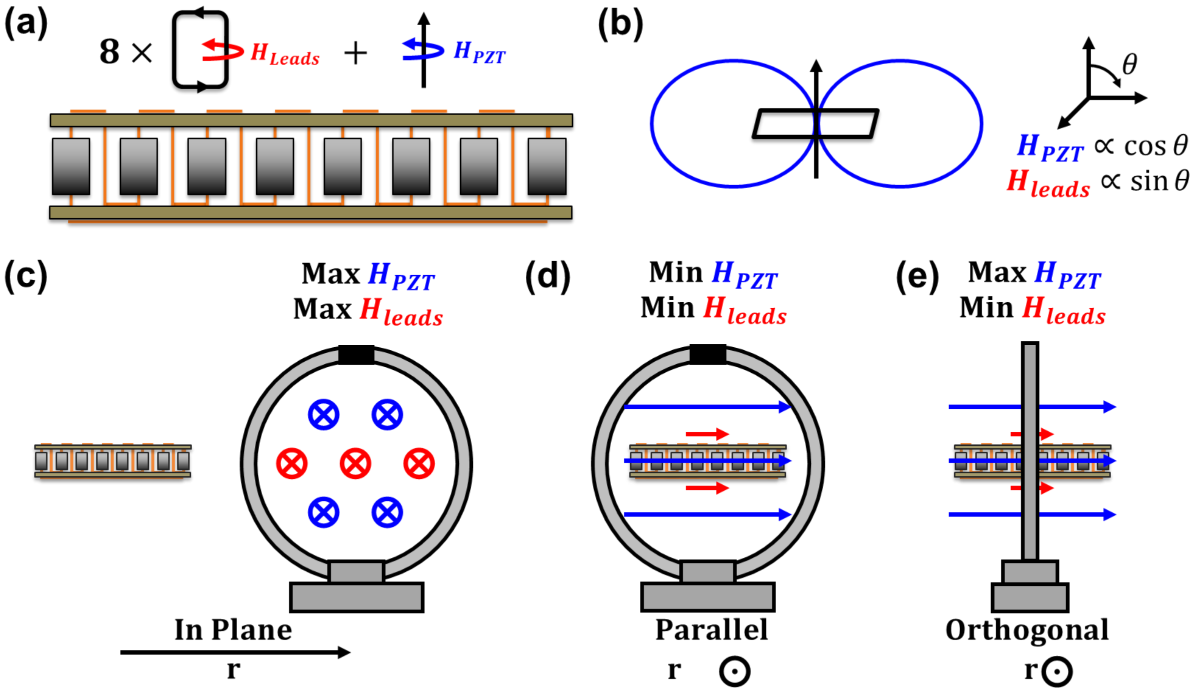

Fig. 5.3. PADA alignment to minimize noise from the driving electronics and wire leads. (a) Mock-up of the loop and linear current elements in the rod PADA array and the corresponding direction of the generated magnetic field. (b) Radiation pattern for ideal electric and magnetic dipoles (current loop) and the angular dependence of the generated magnetic fields on the orientation of the transmitting and receiving antennas. Mock-up of the (c) in-plane, (d) parallel, and (e) perpendicular orientations of transmitter and receiving loops and the relative magnitudes of the measured fields from the current elements in the PADA transmitter.

from the near-field measurement. Once the fields of from the leads become smaller than the radiation from the PADA, the roll-off will converge to 1/r beyond the extended cross-over point. However, due to the greater distance from the transmitter, the measured signal-to-noise ratio in the receiver is diminished.

Measurement of the PADA antennas is conducted using a loop antenna to measure the generated magnetic fields, since for both PADA designs the magnetic field roll-off begins to converge to $1/r$ beyond 5 m. The electric field roll-off converges to $1/r$ beyond 100 m as shown in Fig. 5.2b, even in the absence field contributions from the electrical traces in the transmitter circuitry. Additionally, unlike the magnetic field roll-off which exhibits a smooth transition from $1/r^2$ to $1/r$ roll-off, the electric field roll-off exhibits a null at the cross-over point due to the opposite signs of the near and far-field electric field terms (1.14). Due to the null at the cross-over point, predicted magnitude of the E-field of the eight-element array near 200 m where the roll-off starts to converge to $1/r$ is ~1 μV, which is difficult to measure with commercial antennas. Therefore, the magnetic field measurement is prioritized.

In order to minimize near-field radiation from current loops, all-metal wires and traces are minimized and oriented to exhibit a radiation null toward the receiving antenna as shown in Fig. 5.3. For all PADA configurations, both a linear radiating element, arising from the flipping piezoelectric polarization, and a loop radiating element, arising from the input current used to excite the PADA as well as the displacement current through the PADA, exist. For the case of an array of N elements, as depicted in Fig. 5.3a, N sets of linear and loop currents exist. The radiation patterns from these currents are depicted in Fig. 5.3b and be modeled as ideal electric and magnetic dipoles respectively and with the magnitude of the generated fields exhibiting dependence on the angle between the transmitting currents and the receiving antenna. When the input loop currents are in the same place as the receiving loop antenna, as shown in Fig. 5.3c, the magnetic fields from both the input currents and the PZT cut through the center of the loop, resulting in the maximum measured magnetic field. Although the measured field from piezoelectric radiation is maximized in this configuration, so too is the radiation from the loop. When the transmitting loops and receiving loops are parallel, the magnetic fields from both current components in the PADA transmitter are in the plane of the receiving antenna, resulting in the minimum measured field.

Instead, the optimum configuration to reduce the magnitude of the fields from the input circuit in the measured data is to orient the transmitting loops orthogonal to the receiving loop. For an orthogonal setup, the magnetic fields from the PZT pass through the loop and are maximally coupled to the receiver, while the magnetic field from the electrical currents are in the plane of the receiver and are not coupled. Therefore, an orthogonal setup yields the shortest cross-over distance and largest signal-to-noise measurement of the PADA radiation and utilized for the following measurements.

Wireless radiation measurements of the generated magnetic field are conducted in an open environment to minimize scattering and noise as shown in Fig. 5.4b. The transmitting system consists of a Tektronix AFG3152C function generator connected in series to a 50x Trek model 2100HF amplifier to generate a sufficiently large excitation to measure the far-field as shown in Fig. 5.4a. The amplifier presents a resistance of ~150 Ω in series with the motional resistance of the PZT PADA or PADA array at resonance which results in a diminished loaded quality factor

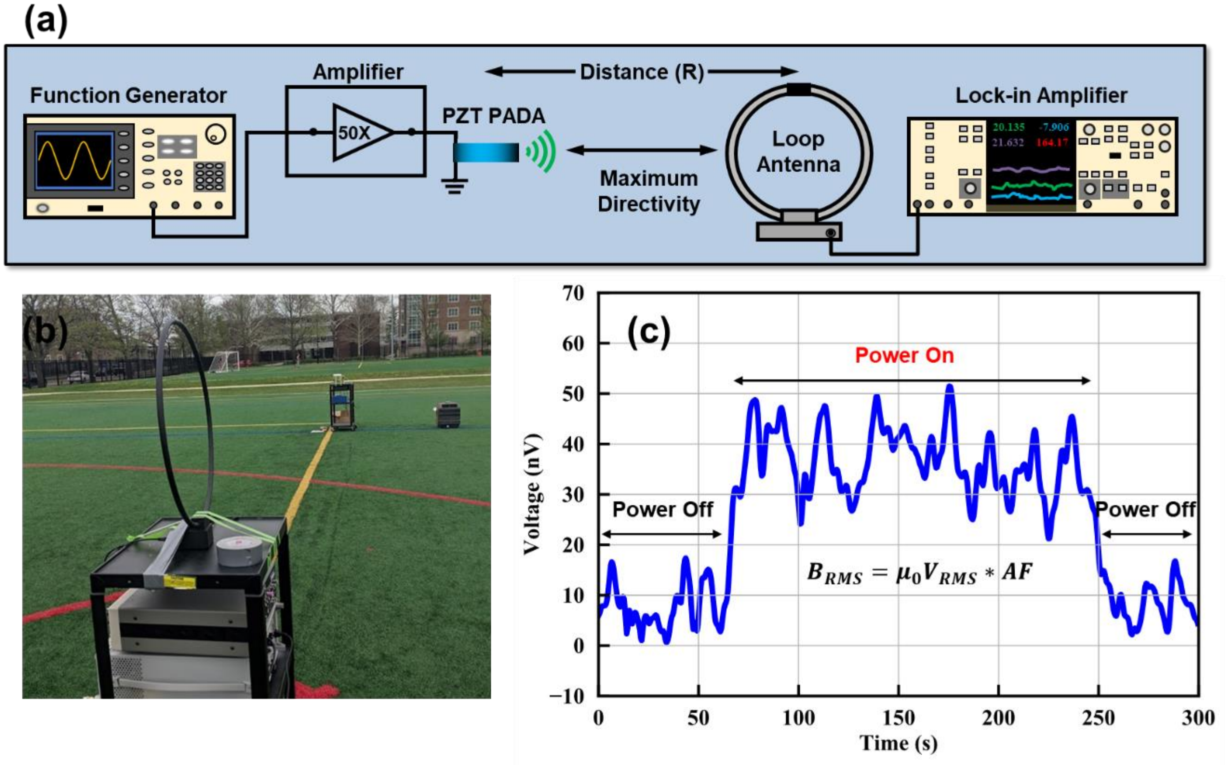

Fig. 5.4. Radiation measurement. (a) Mock-up of the measurement setup. (b) Field measurement in an open athletic field to reduce scattering and background noise. The transmitter (consisting of the function generator, amplifier, and the PADA) is powered separately from the receiver (consisting of the passive loop antenna and lock-in amplifier) using gas generators to remove ground loop radiation. (c) Sample of measured voltage from lock-in amplifier vs. time at 2 meters. The measured voltage from the antenna terminals from which the measured magnetic field is extracted using the antenna factor. Both the field measurements (power on) and noise (power off) are post-processed and extracted. Average noise < 10 nV (14 fT).

where $Q_L \approx QR_m/(R_m + R_s)$. The magnetic field is measured using an AH-Systems SAS-565L 24” shielded passive loop antenna which is oriented to receive the maximum signal from the PZT far-field component. Antenna pattern is not directly measured due to the weak radiation field strength but is assumed to approximate the field pattern of an ideal dipole due to the linear nature of the alternating piezoelectric dipoles and the small size of the radiating elements relative to their electromagnetic wavelength. Incident radiation generated by the PADAs induces an open circuit voltage across the antenna terminals proportional to the field strength. The antenna factor of the loop receiver is calibrated by the manufacturer post-production to be 1.74 Ω^{-1}m^{-1} at 33 kHz and 1.07 Ω^{-1}m^{-1} at 71 kHz, and is used to extract the measured B-field where $B_{RMS} = \mu_0 V_{RMS} * AF$. The calibration of the passive loop antenna is verified using a commercially calibrated FMZB

1519B active loop antenna to measure an identical source, with < 5% difference in the measured field magnitudes. The open-circuit voltage of the SAS-565L antenna is measured using a Stanford Research Systems SR865A lock-in amplifier that is frequency locked to the transmitting PZT PADA and employs a 24 dB/octave bandpass filter to attenuate noise around the locked frequency.

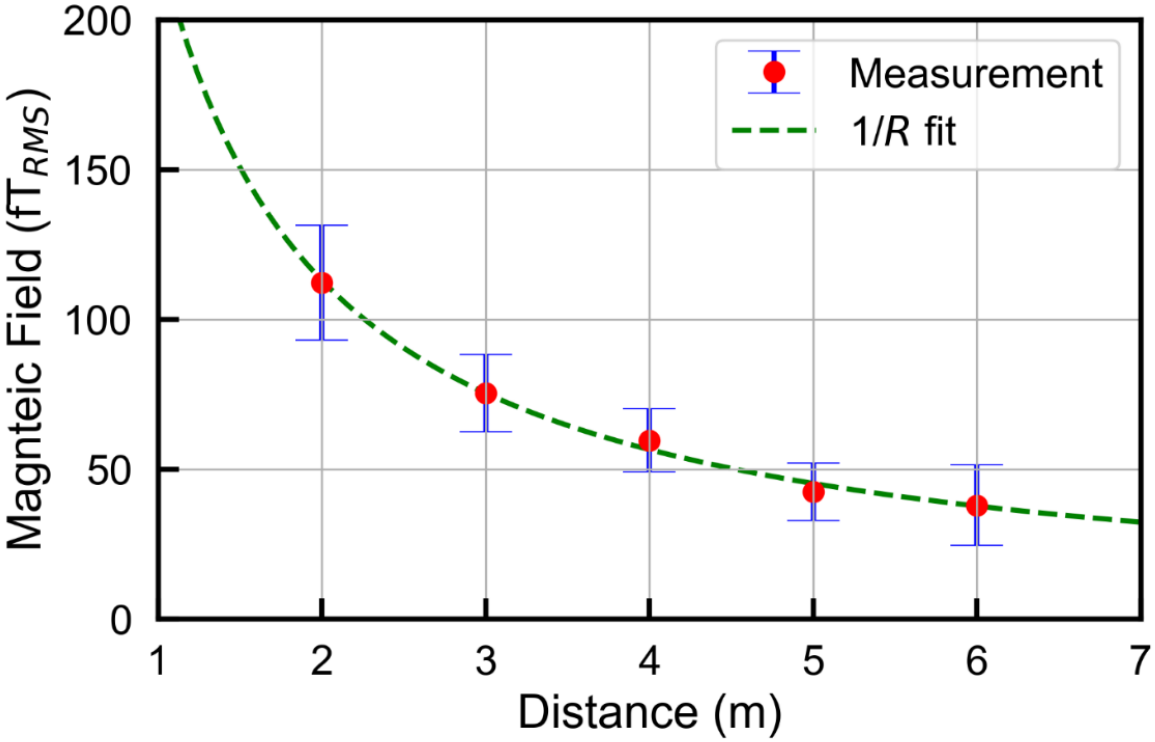

Fig. 5.5. The measured B-field roll-off with distance for the disk PADA with a cross-over point at 1.3 m.

Measurements were made at 1 m distance intervals for 2 minutes at a time, as shown in Fig. 5.4c, using a 1 second time constant. The measured B-field strengths of the disk and rod PADAs are shown in Fig. 5.5 and Fig. 5.6 respectively. The B-fields extracted from the average terminal voltage over the 2-minute measurement window, with 1 standard deviation error bars also provided to account for variance in the measured field strength due to noise. Between field measurements, the noise floor is measured at 1-minute intervals with the input signal turned off. The measured radiation of the PADA disk is presented in Fig. 5.5. Measurements beyond 6 m exhibit a signal-to-noise ratio < 2 and are not shown. Extrapolating the measured data to 1 km yields a magnetic field of 0.45 fT_{RMS} with a driving power of 1.2 W compared to a simulated magnetic field of 1 fT_{RMS}. The roll-off of the B-field with distance for the eight-element rod array is plotted in Fig. 5.6a along with the theoretical $1/r$ and $1/r^2$ curves fit to the measured field at the cross-over point.

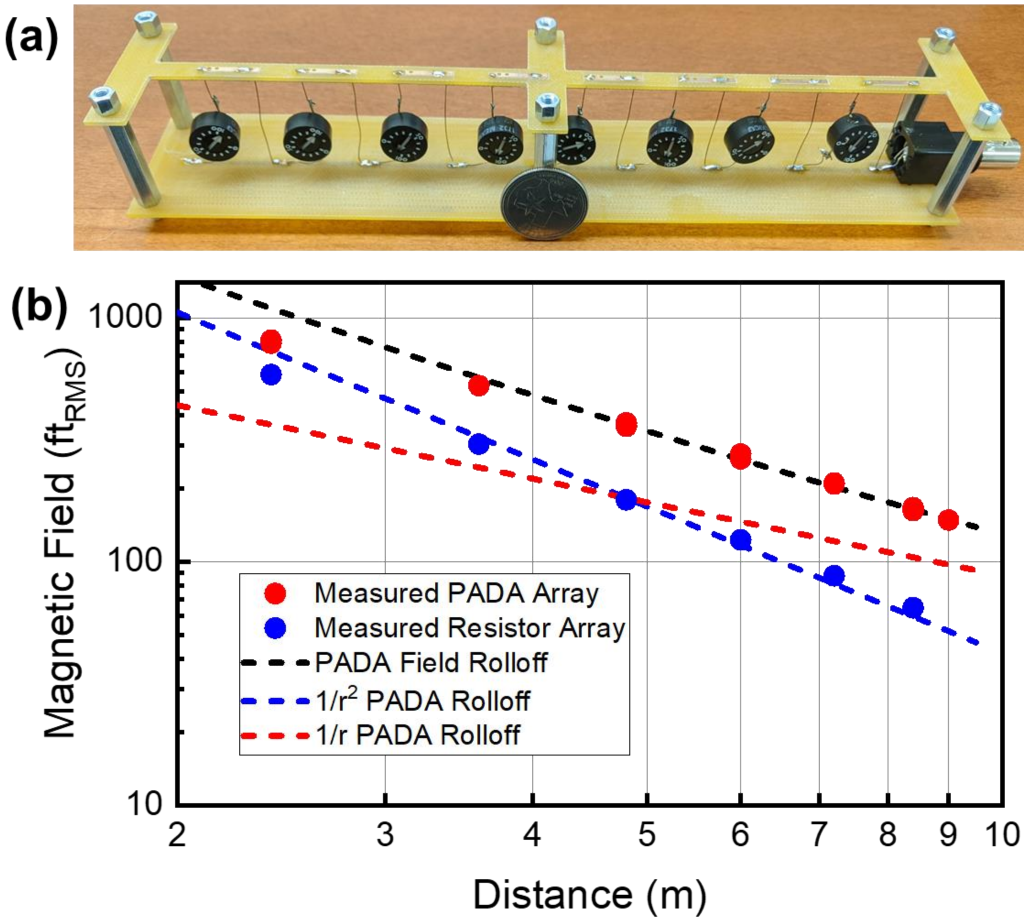

Fig. 5.6. Characterization of radiation from 8-element rod array. (a) 8-element resistor array to de-embed radiation from electrical current from the measured radiation (b) Measured roll-off for both the 8-element PADA and resistor arrays including the simulated roll-off curves fit to the measured fields from the PADA array at the expected cross-over point. The roll-off for the PADA array converges to 1/r beyond 5 m while the resistor array falls off as ~1/r^2.

The measured B-field exhibits a cross-over point at 5 m as expected from simulation, with the roll-off converging to 1/*r* near 10 m. Close to the antenna, the deviation of the measured data from the expected 1/r^2 fit is attributed to misalignment error between the transmitting current loops and the receiver antenna resulting the receiver measuring the input current in the electrical traces as well as the rod PADA array. To verify that the 1/r roll-off is due to the PADA radiation, an eight-element variable resistor array is fabricated as shown in Fig. 5.6a. Each resistor is tuned to the average motional impedance of the array elements at the operating frequency of 70.8 kHz such that the input power, current, and voltage is identical for both the resistor and PADA arrays. An input voltage of 125 V, corresponding to an input power of 2.42 W, is applied to the PADA array, which generates an extrapolated B-field at 1 km of 1.34 fT$_{RMS}$ compared to the simulated field

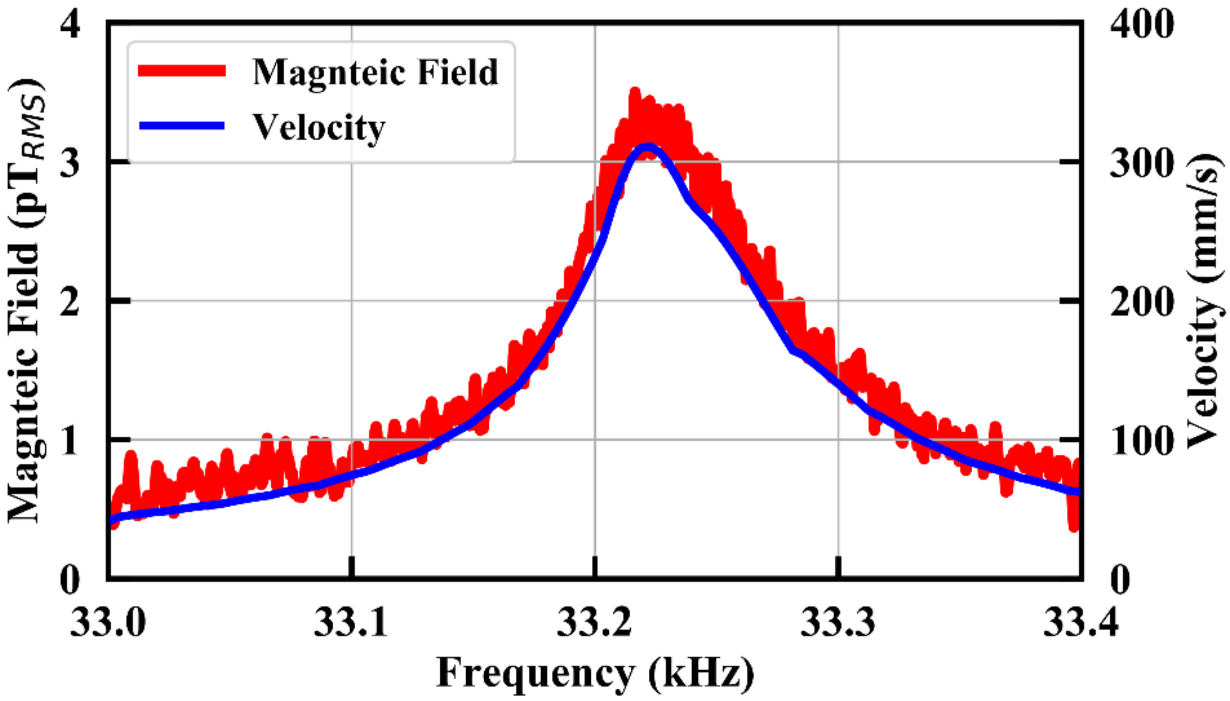

Fig. 5.7. Correlation between PADA radiation and edge velocity of the disk PADA as a function of frequency.

strength of 2.26 fT$_{RMS}$. The discrepancy between the simulated and measured field strengths is likely due to imperfect earth ground effects [13], shifts in resonance due to ambient temperature changes and thermal nonlinearity.

The efficiency of the PADA elements is limited by the power handling of the PZT elements. Although the presented PADA efficiency is more than three orders of magnitude greater than an equivalently sized electrical antenna, from Fig. 4.5 the radiation efficiency is still poor (~10^{-10}) and therefore in order to wirelessly measure the radiation, high input power (> 1 W) is required. As the resonators start to exhibit thermal nonlinearity at increased power levels, resulting in diminished efficiency. Since PADA radiation occurs due to physical charge displacement in the piezoelectric, the magnitude of the radiation can be extrapolated from the physical displacement of the resonator. Figure 5.7 shows the measured velocity and magnetic field of the PZT disk PADA. The magnetic field is measured at 1 with the SAS-565L loop antenna connected to a spectrum analyzer while the edge velocity of the disk PADA is simultaneously measured using a Polytec OFV-5000 laser vibrometer. From Fig. 4.19, driving the 8-element array at 2.42 W results in a 19% reduction resonator edge-velocity and piezoelectric current, corresponding to a 34% loss

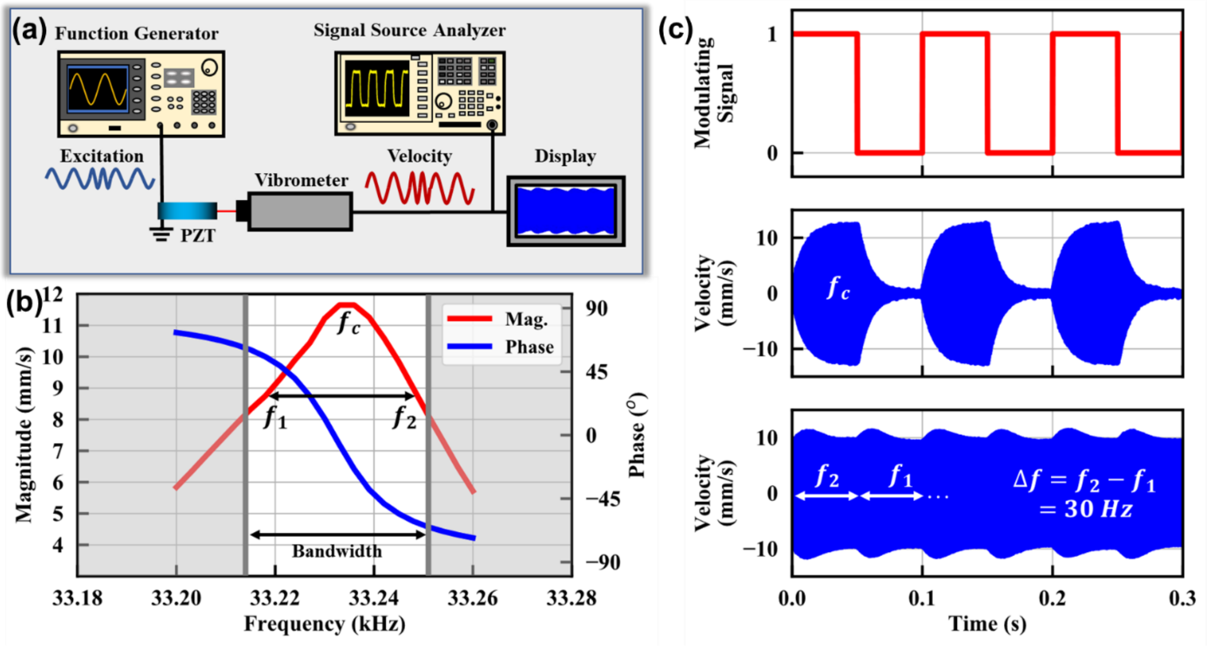

Fig 5.8. Different modulation schemes applied to the PADA. (a) Mock-up of the measurement setup. (b) Frequency response of the velocity (both magnitude and phase are measured) at the PZT disk edge. (c) (top) 10 Hz bit stream, (middle) vibrometer velocity measurement of the amplitude-shift keyed (ASK) signal, and (bottom) vibrometer velocity measurement of the frequency-shift keyed (FSK) signal.

in efficiency. Additionally, due to the bifurcation and shifting resonance frequency due to thermal nonlinearity at elevated temperatures, the PADAs cannot be driven at resonance. As seen in Fig. 5.7, driving off-resonance results in a diminished magnetic field, and further contributing to the reduced measured efficiency relative to the simulated (linear) efficiency.

5.2 Modulation

Direct digital modulation of the PADA can be done by altering amplitude, frequency, and phase of the excitation signal which in turn modulates the mechanical resonance of the PADA and thus radiated signal. In this dissertation, BFSK is chosen since it has a continuous phase which lowers the mechanical settling time compared to both BPSK and BASK. The modulation is evaluated using the measurement setup in Fig. 5.8a. The setup consists of a Tektronix AFG3152C function generator that directly excites the disk PADA with continuous phase BASK or BFSK signals. A Polytec OFV-5000 laser vibrometer is used to measure the velocity of the PZT edge while vibrating in the dilation mode. The two BFSK modulation frequencies are chosen to be within the 3-dB bandwidth as shown in Fig. 5.8b. Figure 5.8c shows the modulated velocity of BASK and

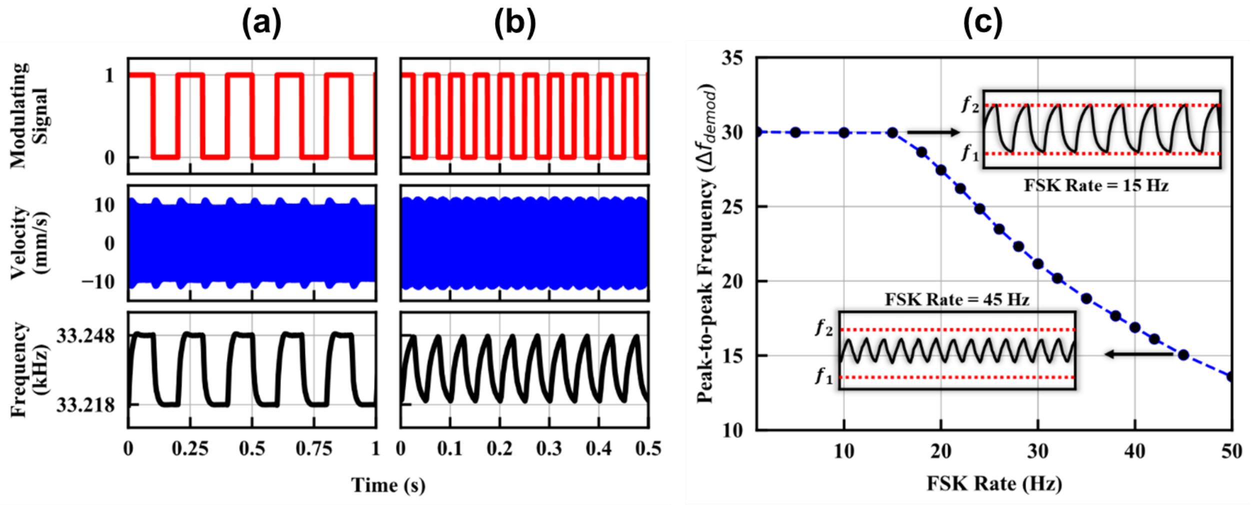

Fig 5.9. Measured FSK modulation of the PZT PADA at different FSK data rates. (a) 5 Hz, and (b) 20 Hz FSK rate. (a, b) (Top) modulating signal, (middle) measured velocity, and (bottom) demodulated signal using signal source analyzer (SSA). (c) Peak-to-peak frequency difference ($\Delta f_{demod} = f_2 - f_1$) after demodulation with SSA at different FSK rates. The upper limit for direct modulation using the 3-dB bandwidth is limited by frequency settling as the maximum direct modulation frequency is approached resulting in a distorted modulation waveform.

BFSK with a 10 Hz modulation rate. The velocity signal is then inputted to a Rohde & Schwarz FSUP signal source analyzer with FM demodulation capability to demodulate the signal as shown in Fig. 5.9a and 5.9b (bottom figures) for 5 Hz and 20 Hz BFSK rates, respectively.

The PZT disk is directly modulated using a function generator outputting both ASK and FSK signals with the resonant response of the PZT disk captured using an optical vibrometer as shown in Fig. 5.8a. In both cases, the 10 Hz binary bitstream at the top of Fig. 5.9c is used. With the ASK signal, as the driving signal is switched on and off the resonator energy ramps up and down over a duration inversely proportional to the loaded quality factor ($Q_L \approx 850$) The ramping time limits the fundamental modulation rate for direct BASK to approximately 1/2T, where the time constant $T = 3 \times (2Q_L/\omega) \approx$ 24.4 ms (corresponding to 95% settling from the peak value) for the demonstrated measurement. A fundamental design tradeoff must be considered to balance the inversely proportional data rate with the high Q desired for the radiation FoM. BFSK modulation is conducted within the 3-dB bandwidth of the PZT resonator corresponding to BFSK frequencies of f_1 = 33.218 kHz and f_2 = 33.248 kHz. The input is a continuous-phase FSK with no discontinuity when switching between the two frequencies. However, due to the phase difference of the mechanical resonator at the two frequencies, the mechanical resonance is out of phase with the modulated driving signal when it is switched and ramping of the PZT edge velocity occurs while energy is transferred from one resonant frequency to another as seen in Fig. 5.8c (bottom). As the modulation frequency approaches the limit set by the frequency settling, although the amplitude of resonance is not diminished, the demodulated output signal is distorted as seen in Fig. 5.9a and 5.9b.

Modulation of the rod PADAs is conducted similarly to the disk. Modulation is investigated both for a single rod element, as well as for three elements connected in both a series and parallel array configuration. The measured admittance response of the single element and two array configurations is shown in Fig. 5.10a. The three array elements are chosen to have a small resonant frequency separation (<10 Hz) resulting in negligible frequency desynchronization of the parallel array. Input power to each resonator is kept constant across configurations, such that heating and thermal resonance shifts are constant, and the same resonant frequency is maintained. Due to the loading of the source impedance, the quality factor of the single PADA and PADA arrays is loaded. The series array exhibits the greatest motional resistance, and thus highest loaded Q and smallest 3 dB bandwidth compared to the other configurations. An FSK frequency separation of 100 Hz between 71.54 and 71.64 kHz is chosen for each array to be within the 111 Hz 3 dB bandwidth of the series array and the measured modulation with a 5 Hz FSK rate is shown in Fig. 5.10b. The modulation of the single element is measured from the edge velocity using the setup shown in Fig. 5.8a. Due to the different quality factors of the individual elements used in the arrays, each resonator exhibits a unique velocity magnitude, making it difficult to extract the array modulation from the velocities of the individual elements. Instead, the modulated magnetic field generated by the array is measured at a 0.5 m standoff using the SAS-565L loop antenna connected to the FSUP signal source analyzer. The stand-alone rod is not measured wirelessly due to the small signal-to-noise ratio of the diminished radiated power. From Fig. 5.10b, some additional noise is added to the demodulated signal due the low signal-to-noise ratio of the measured signal. As the modulation rate is increased, the magnitude of the frequency separation diminishes due to the Q-defined settling rate exceeding the bit duration as shown in Fig. 5.11. Due to the diminished Q of the rod PADAs, the maximum direct modulation rate is nearly double the disk resonators, while also demonstrating greater efficiency.

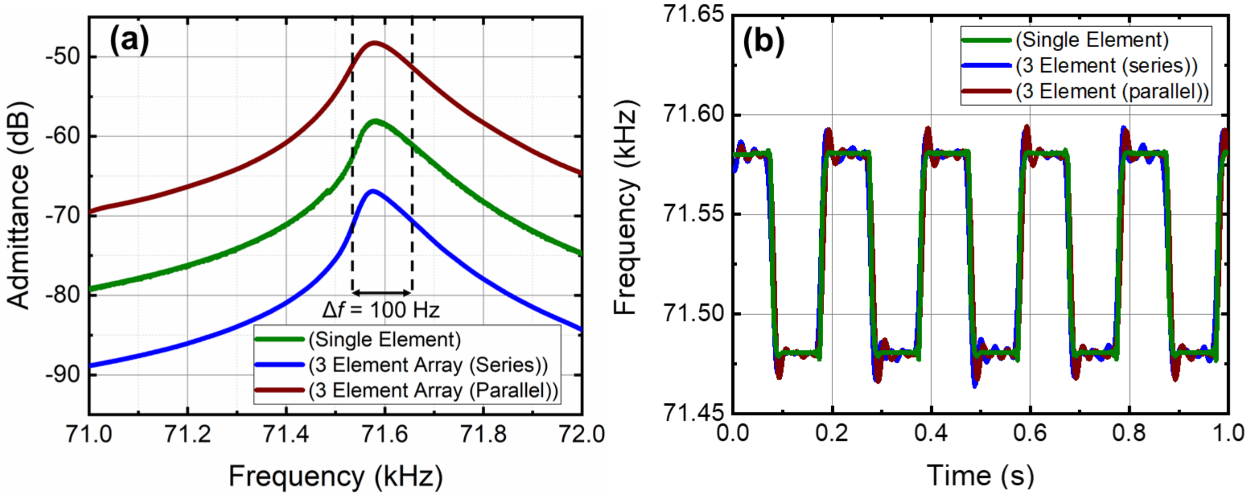

Fig 5.10. Measured frequency response and modulation of rod PADAs both as single element and in 3-element series and parallel arrays. a, Measured frequency response of the three rod PADA configurations with a 100 Hz FSK frequency separation chosen to be within the 3 dB bandwidth of all three configurations. b, Modulation of the three rod PADA configurations at 5 Hz.

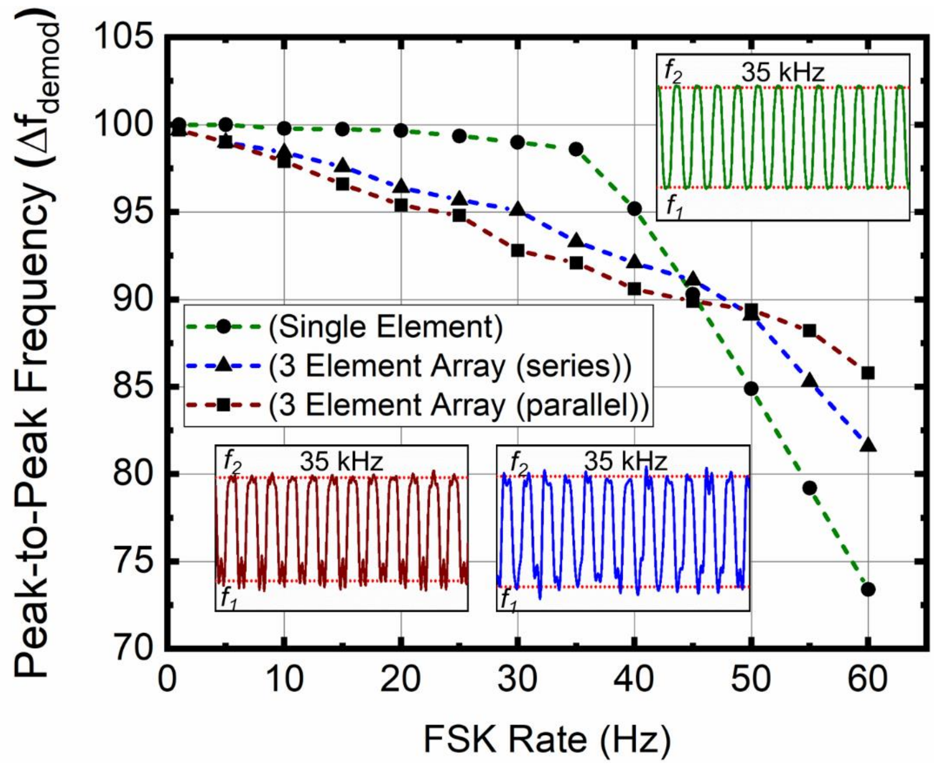

Fig 5.11. Peak-to-peak frequency difference ($\Delta f_{demod} = f_2 - f_1$) after demodulation with SSA at different FSK rates. The upper limit for direct modulation using the 3-dB bandwidth is limited by frequency settling as the maximum direct modulation frequency is approached resulting in a distorted modulation waveform.

Chapter 6: Discussion and Future Work

Despite the demand for portable VLF communication for long-range, low-power applications with modest bandwidth requirements, electrical antennas have proven untenable at VLF frequencies due to the inherently poor tradeoff between electrical size and efficiency. Acoustic antennas operating at wavelengths up to five orders of magnitude less than EM wavelengths have been considered as alternatives to overcome the inefficiency of sub resonance operating sizes. However, until recently, piezoelectric materials have been insufficient to meet demands for handheld communication. As shown in (2.15), efficient radiation requires both large electromechanical coupling coefficients and a high mechanical quality factor, which is difficult to achieve since most piezoelectric materials empirically exhibit an inverse relationship between these parameters. Moreover, the relative permittivity of the piezoelectric material must be as high as possible in order to relax the electrical breakdown limit of the surrounding medium and maximize the radiated power. Additionally, even if desirable piezoelectric material properties can be achieved, fabricating the piezoelectric geometry and orientation to achieve the desired fundamental acoustic resonance mode can prove difficult due to poling and material growth considerations.

Unlike most electrical antennas where the far-field regime of VLF antennas occurs kilometers away from the source, far-field radiation from the ADMIRE can be measured as close as two meters. Typically, at distances less than a wavelength away from an antenna, the near-field reactive energy component is much larger than the far-field radiated energy. Since the reactive fields decay ($1/R^2$) much faster with distance than the radiated fields ($1/R$), at some distance approximately one wavelength from the antenna the radiated field becomes larger than the reactive near-fields. However, the high relative permittivity of the PZT (~1000) confines most of the reactive energy inside of the PZT, greatly reducing the cross-over point where the radiated fields become dominant and allowing the radiated far-field to be directly measured at distances as close as two meters. Although such a close far-field region is unconventional for VLF electrical antennas, the theoretically predicted phenomena were experimentally verified as shown in Fig. 5.4 and Fig. 5.5 where the measured magnetic field decays at a rate of $1/R$ beyond the cross-over point. Since the reactive fields are normally much larger than the radiated fields near the antenna, the reduction of the reactive fields due to confinement inside of the PZT limits the currently achievable communication distance of the ADMIRE prototype for near-field communications. However, the high permittivity does not diminish the radiated fields, and as more efficient materials, designs, and power handling schemes are implemented, scaling the link distance is much more promising than for ESAs.

To achieve orders of magnitude distance scaling without greatly increasing the size of transmitters, better designs are needed to harness the ultimate efficiency of piezoelectric antennas, which theoretically can be orders of magnitude greater than demonstrated here. In particular, higher coupling coefficient modes and materials provide significant promise for increasing efficiency. The demonstrated PZT PADAs are presented as a proof-of-concept and to lay the groundwork for piezoelectric antennas. From (2.15), maximizing resonator designs and materials with higher d^2V products will lead to improvements in efficiency. High coupling materials such as PMN-PT with piezoelectric coupling coefficients more than 10 times higher than PZT have the potential for even more drastic efficiency enhancement [132]. Although the quality factors (typically < 100 for current commercial availability) of relaxor ferroelectric materials such as PMN-PT are low, the massive coupling coefficients, more than 10 times the PZT coupling coefficient, compensate in (2.15) to potentially provide orders of magnitude enhancement in volumetric efficiency over the PADA demonstrated here. However, as discussed in Chapter 4, (2.15) is strictly a material efficiency and proper resonator design must be utilized to approach the theoretical material efficiency. For resonators comprised of a single material, fringing fields within the resonator is primarily determined by the area and separation of the exciting electrodes. Therefore, low aspect, ratio lateral vibrating resonators with small fringing fields show great promise for approaching the material efficiency limit.

The demonstrated PZT PADAs are constrained to operate in fundamental resonance modes in order to minimize internal current cancelation and maximize efficiency. However, additional work is needed to investigate the potential for higher-order extensional modes. Strictly from a material standpoint, higher-order extensional modes result in diminished efficiency due to canceling current elements as discussed in [55], however as discussed in Chapters 3 and 4, resonator efficiency is also diminished due to displacement fields from the PADA electrodes. For the case of higher aspect ratio resonators such as the rod PADA, the fringing field from the electrodes results in significant piezoelectric charge neutralization and lost efficiency. If electrode configurations in higher-order mode resonators are chosen to neutralize the opposing charge portion of the resonator, higher frequency modes may be possible without significant loss in efficiency, allowing higher frequency operation without sacrificing element size.

Although the current measurement distance is limited, the short standoff is primarily limited by power handling considerations and is not indicative of the ultimate communication distance of acoustic antennas. Thermal dissipation in the demonstrated PADA limits the input power to be well below the mechanical (ultimate stress) or electrical (breakdown) driving limits. Improving temperature control to achieve greater power handling or implementing arrays of PADAs, where phase synchronization is simplified by the moderate *Q*, can enable a significant improvement in the PADA range. In particular, arrays show great promise for PADA systems operating above VLF, where the physical size of individual elements is constrained by the acoustic wavelength of the resonant mode and element volume is reduced. PADA radiation efficiency scales with volume and the cube of frequency, but due to the intrinsic relationship between operating frequency and resonator size, that ratio is roughly constant as the frequency is increased. Arrays allow for the effective volume to be maintained, such that effective efficiency scales as frequency cubed similar to electrical antennas. Additionally, the negligible coupling between adjacent, higher permittivity PADA elements allows for a compact array with high volumetric efficiency. Due to the large electromagnetic wavelength and relatively weak individual element radiation, it is unlikely that PADA arrays will exhibit significant beam-forming capabilities, however, additional work must be conducted to verify the capabilities large PADA arrays.

High coupling, lower quality factors also provide the potential for larger bandwidths and greater data rates. PADA modulation is demonstrated here with continuous phase BFSK in order to avoid amplitude settling. The directly modulated PADA achieved modulation rates of up to 90 bps, which could potentially be increased to beyond 1 kbps in PMN-PT antennas ($Q = 100$) without loss of efficiency. If much faster modulation rates are required, implementing additional circuitry such as reactive tuning elements for DAM to avoid settling times or improving the receiver demodulation scheme can be adopted. Further investigation is required to modulation of PADA arrays consisting of resonators with non-uniform quality factors and resonant frequencies.

Appendix A: PZT Material Properties

The PZT elements (PIC-181) were bought commercially from PI Ceramics (www.piceramic.com). Relevant material properties necessary for PADA modeling and design are given below. Material properties are characterized by the manufacturer prior to shipping and therefore may vary slightly from the manufacturer's website.

$$\varepsilon_r^T = \begin{bmatrix} 1224 & 0 & 0 \\ 0 & 1224 & 0 \\ 0 & 0 & 1135 \end{bmatrix}$$

$$\varepsilon_r^S = \begin{bmatrix} 740 & 0 & 0 \\ 0 & 740 & 0 \\ 0 & 0 & 624 \end{bmatrix}$$

$$d = \begin{bmatrix} 0 & 0 & 0 & 0 & 389 & 0 \\ 0 & 0 & 0 & 389 & 0 & 0 \\ -108 & -108 & 253 & 0 & 0 & 0 \end{bmatrix} \text{ pC/N}$$

$$e = \begin{bmatrix} 0 & 0 & 0 & 0 & 475 & 0 \\ 0 & 0 & 0 & 475 & 0 & 0 \\ -120 & -120 & 265 & 0 & 0 & 0 \end{bmatrix} \text{ C/m}^2$$

$$S^E = \begin{bmatrix} 11.75 & -4.07 & -4.996 & 0 & 0 & 0 \\ -4.07 & 11.75 & -4.996 & 0 & 0 & 0 \\ -4.996 & -4.996 & 14.11 & 0 & 0 & 0 \\ 0 & 0 & 0 & 35.3 & 0 & 0 \\ 0 & 0 & 0 & 0 & 35.3 & 0 \\ 0 & 0 & 0 & 0 & 0 & 31.6 \end{bmatrix} \text{ pm}^2\text{/N}$$

$$C^E = \begin{bmatrix} 152.3 & 89.09 & 85.47 & 0 & 0 & 0 \\ 89.09 & 152.3 & 85.47 & 0 & 0 & 0 \\ 85.47 & 85.47 & 134.1 & 0 & 0 & 0 \\ 0 & 0 & 0 & 28.3 & 0 & 0 \\ 0 & 0 & 0 & 0 & 28.3 & 0 \\ 0 & 0 & 0 & 0 & 0 & 31.61 \end{bmatrix} \text{ GPa}$$

Appendix B: Measurement Equipment

The following is a list of all measurement equipment used for the data collection presented here.

Tektronix AFG3152C function generator: Used to generate all input signals to the PADA elements including single-tone excitation for radiation measurements, frequency swept excitation for admittance measurements, and modulated excitation including FSK, ASK and BASK for modulation measurements.

50x Trek model 2100HF amplifier: Used for all radiation measurement to step up the voltage produced by the Tektronix AFG3152 function generator and increase the input power and thus the radiated power.

Agilent E4445A spectrum analyzer: Used in all characterization measurements to measure both the admittance response of the PADAs as well as the power consumed by the PADAs. Power consumption is measured separately from radiation due to the ground loops in the characterization measurement setup generating a large magnetic field that dominates the PADA radiation.

Stanford Research Systems SR865A lock-in amplifier: Used to measure the fields generated by the PADAs by measuring the voltage across the receiver loop terminals. The lock-in amplifier is frequency locked to the function generator signal and the DC component of the reference lock-in frequency mixed with the received signal is low-pass filtered to minimize spectral noise.

Polytec OFV-5000 laser vibrometer: Used to measure the edge velocity of the PZT resonators. Since the magnetic field is proportional to piezoelectric current, and piezoelectric current is proportional to edge velocity, radiation is extracted from measured velocity to compared to the measured fields. The velocity measured by the laser vibrometer is also used to measure the modulation of individual rod and disk elements as demonstrated in Figs. 5.8-5.11 as well as their thermal nonlinearity as shown in Fig. 4.19 and Fig. 4.20.

ROHDE & SCHWARZ FSUP signal source analyzer: Used to demodulate the modulated PADA signals measured by both the laser vibrometer and the passive loop antenna as shown in Figs. 5.8-5.11.

Schwarzbeck FMZB 1519B: Active loop antenna used to verify the antenna factor of the SAS-565L passive loop antenna. Measurements using the SAS-565L passive loop antenna are prioritized due to no battery life limitation and lower noise floor.

A.H. Systems SAS-565L 24" passive shielded loop antenna: Used in all reported magnetic field measurements. The voltage across the antenna terminals is measured using the lock-in amplifier when measuring the radiated signal at a single input frequency as in Figs. 5.4-5.6, with the spectrum analyzer when measuring radiation as a function of frequency as in Fig. 5.7, or with the signal source analyzer when measuring the modulation radiation as in Fig. 5.10 and Fig. 5.11.

Calibration of the SAS-565L antenna is conducted by the manufacturer. The calibrated antenna factors defined in (B.1) and (B.2) are given in Table B.1.

Electric Field Antenna Factor:

$$AF^{E} = \frac{E}{V}, \quad AF^{E}_{\frac{dB}{m}} = E_{\frac{dBV}{m}} - V_{dBV} \tag{B.1}$$

Magnetic Field Antenna Factor:

$$AF^{H} = \frac{H}{V}, \quad AF^{H}_{\frac{dB}{m}} = H_{\frac{dBA}{m}} - V_{dBV} \tag{B.2}$$

Table B.1: E- and H-field Calibrated Antenna Factors

Frequency (KHz)	E-Field AF (dB/m)	H-Field AF (dB/m)	Frequency (KHz)	E-Field AF (dB/m)	H-Field AF (dB/m)	Frequency (KHz)	E-Field AF (dB/m)	H-Field AF (dB/m)
0.02	117.67	66.17	17	60.16	8.66	95	51.904	0.404
0.03	113.695	62.195	18	59.737	8.237	100	51.87	0.37
0.04	111.366	59.866	19	59.306	7.806	110	51.744	0.244
0.05	109.578	58.078	20	58.884	7.384	120	51.596	0.096
0.06	108.391	56.891	21	58.601	7.101	130	51.457	-0.043
0.07	107.427	55.927	22	58.303	6.803	140	51.369	-0.131
0.08	105.906	54.406	23	57.995	6.495	150	51.318	-0.182
0.09	104.713	53.213	24	57.813	6.313	160	51.256	-0.244
0.1	103.785	52.285	25	57.484	5.984	170	51.215	-0.285
0.2	98.164	46.664	26	57.012	5.512	180	51.166	-0.334
0.3	94.721	43.221	27	56.7	5.2	190	51.118	-0.382
0.4	91.813	40.313	28	56.456	4.956	200	51.095	-0.405
0.5	89.891	38.391	29	56.302	4.802	210	51.081	-0.419
0.6	88.252	36.752	30	56.204	4.704	220	51.05	-0.45

Table B.1: E- and H-field Calibrated Antenna Factors (cont.)

Frequency (KHz)	E-Field AF (dB/m)	H-Field AF (dB/m)	Frequency (KHz)	E-Field AF (dB/m)	H-Field AF (dB/m)	Frequency (KHz)	E-Field AF (dB/m)	H-Field AF (dB/m)
0.8	85.293	33.793	32	55.916	4.416	240	51.035	-0.465
0.9	84.859	33.359	33	55.742	4.242	250	51.002	-0.498
1	84.188	32.688	34	55.548	4.048	260	50.97	-0.53
1.5	80.324	28.824	35	55.358	3.858	270	50.938	-0.562
2	77.962	26.462	36	55.251	3.751	280	50.921	-0.579
2.5	75.884	24.384	37	55.144	3.644	290	50.95	-0.55
3	74.507	23.007	38	55.026	3.526	300	50.96	-0.54
3.5	73.245	21.745	39	54.859	3.359	320	50.908	-0.592
4	71.902	20.402	40	54.691	3.191	340	50.964	-0.536
4.5	71.243	19.743	41	54.537	3.037	360	50.921	-0.579
5	70.143	18.643	42	54.418	2.918	380	50.938	-0.562
5.5	69.424	17.924	43	54.299	2.799	400	50.687	-0.813
6	68.455	16.955	44	54.208	2.708	420	50.926	-0.574
6.5	67.848	16.348	45	54.157	2.657	440	51.049	-0.451
7	67.152	15.652	46	54.105	2.605	460	50.944	-0.556
7.5	66.591	15.091	47	54.044	2.544	480	50.542	-0.958
8	66.069	14.569	48	53.976	2.476	500	50.377	-1.123
8.5	65.646	14.146	49	53.908	2.408	550	50.414	-1.086
9	65.138	13.638	50	53.836	2.336	600	51.046	-0.454
9.5	64.699	13.199	55	53.351	1.851	650	51.011	-0.489
10	64.27	12.77	60	52.929	1.429	700	50.448	-1.052
11	63.495	11.995	65	52.634	1.134	750	50.508	-0.992
12	62.761	11.261	70	52.571	1.071	800	51.016	-0.484
13	62.333	10.833	75	52.41	0.91	850	51.47	-0.03
14	61.768	10.268	80	52.307	0.807	900	51.435	-0.065
15	61.109	9.609	85	52.241	0.741	950	51.293	-0.207
16	60.556	9.056	90	52.076	0.576	1000	51.223	-0.277

Appendix C: Rod Fabrication, Characterization and Array Assembly

A mock-up of the rod resonator fabrication is shown in Fig. 4.9. A nitric acid resistant adhesive polyvinyl chloride tape mask is patterned using a 3 mm diameter hole punch and manually positioned on the top and bottom surface of the PZT rod. Due to the moderate adhesion between the PZT and silver electrode, during tape mask delamination after electrode definition, the silver electrode can be peeled off the PZT along with the tape mask, causing electrode deformation as shown in Fig. C.1a. Both a Sn60:Pb40 solder and an MG Chemicals 8331-14G conductive silver epoxy are used to mechanically and electrically fix the silver electrodes to the copper lead wires. In order to minimize the thermal depolarization of the PZT, the solder temperature is kept below the reported 330^o C Curie temperature of the PZT. Since thermal depolarization begins to occur below the Curie temperature [133], soldering prioritized minimizing the temperature rise in the PZT. Solder temperature is maintained at 300^o C to balance the tradeoff between a high temperature, short-duration contact and a lower temperature, longer duration contact. Due to the relatively low thermal conductivity of the PZT [~1.3 W/(m-K)] which is more than 100 times lower than the thermal conductivity of the silver electrodes, PZT surface temperature near the solder contact is maintained below 65^o C as measured by an Etekcity laser infrared thermometer temperature gun. However, the temperature from the solder can cause delamination of the silver electrodes from the PZT as shown in Fig. C.1b due to the stress generated at the silver-PZT interface from the thermal expansion of the silver film [134]. Partial delamination of the electrodes can lead to frequency misalignment or spurious mode generation as shown in Fig. 4.13.

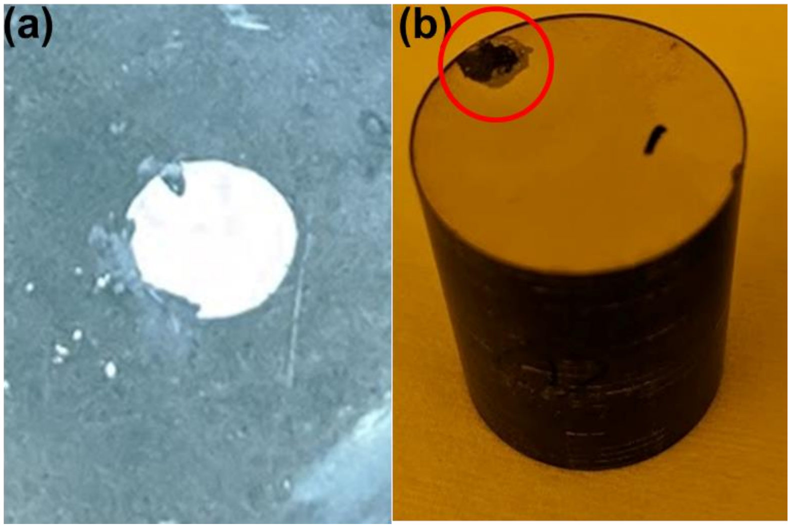

Fig. C.1. Delamination of the silver electrode from PZT. (a) Peeling of the silver electrode during etch mask removal. (b) Removal of the silver electrode where hot solder is applied due to delamination.

Silver epoxy is substituted for the solder connections as a low-temperature alternative with negligible change in resonator quality factor. However, the silver epoxy exhibited moderate adhesion to the silver electrodes, resulting in potential delamination due to applied mechanical stress in the assembly process as shown in Fig. C.2a. Additionally, while the epoxy exhibited relatively stronger static adhesion to the copper wire, after resonant PADA operation the adhesion between the wire and silver epoxy weakens, likely due to the vibration of the rod resonator, particularly when driven at resonance with $P_{in} > 0.2$ W. As adhesion deteriorates, electrical conductivity diminishes, resulting in increased electrical loading of the resonator and inconsistent power delivered to the resonator. Figure C.2b shows the gap between the silver epoxy and copper wire due to loosening after operation, while Fig. C.2c shows a cavity in the epoxy after a loosened wire has fallen out. Due to the lack of robustness of the epoxied connections over sustained operation time and elevated input powers, soldered connections are opted for array operation.

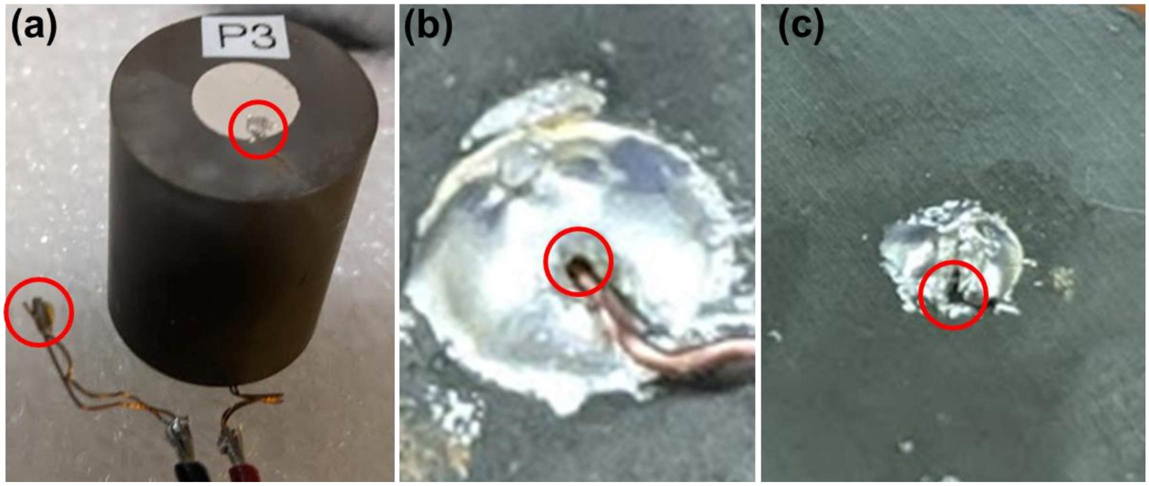

Fig. C.2. Dynamic robustness of silver conductive epoxy adhesion. (a) Removal of the silver electrode where hot solder is applied due to delamination caused by mechanical adhesion between silver electrodes and silver epoxy. (b) Loosening of silver epoxy adhesion to the copper wire during PADA operation. (c) Loose copper wire removed from epoxy after PADA operation due to lack of adhesion.

Characterization of individual rods was conducted by epoxying or soldering copper, 30 AWG wire to the top and bottom electrodes. BNC-to-alligator clips are then used to connect the top electrode to the input signal from the Tektronix AFG3152C function generator and the bottom electrode to the Agilent E4445A spectrum analyzer to characterize the admittance response of the individual rod resonators as a function of input power and frequency. Multiple clamping configurations are considered to hold the resonators with examples shown in Fig. C.3. The rod PADAs were position with both the flat ends and rounded sides resting on both a rigid wood surface and a rigid foam surface as shown in Fig. C.3a and Fig. C.3b. Additionally, a metallic fixture with a half-circle cut-out as shown in Fig. C.3c was used to hold the resonator from the thickness-extensional displacement null which occurs at the resonator midpoint in the thickness direction as shown in Fig. 4.4. Negligible difference in mechanical Q is measured for the different configurations, and therefore the vertical orientation of the rods with the bottom surface resting flat on two wooden slates as shown in Fig. C.4 is chosen for simple implementation. Extrinsic mechanical clamping and anchor losses are common sources of Q degradation in acoustic resonators, however, for the PZT rod PADAs with a mechanical Q of approximately 1000, the negligible change in Q with the different types of fixtures indicates that intrinsic material losses are the dominant form of loss. For higher quality factor PADAs, additional care may be needed to minimize extrinsic losses in the packaging configuration.

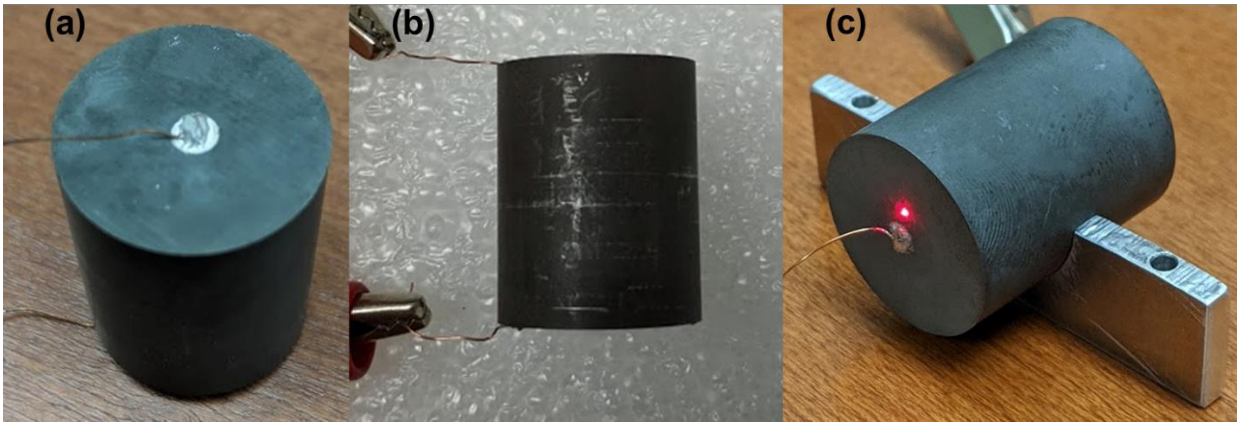

Fig. C.3. Examples of fixtures for rod PADA. (a) End of rod PADA placed on a rigid wood base. (b) Side of rod PADA placed semi-rigid foam base. (c) Thickness extensional resonance null placed on a rigid clamp.

Due to the solder ball deforming the flatness of the bottom surface of the rod PADA elements, the rod elements are mounted on two parallel wooden slates with a diameter greater than the solder ball. The slates increase the mechanical stability of the array and ensure that all rod elements are oriented vertically for alignment to the receiving antenna.

Fig. C.4. Rod PADA array elements mounted on wooden slates to ensure vertical alignment.

References

[1] Y. Yang, R. Lu, T. Manzaneque, and S. Gong, “Toward Ka band acoustics: Lithium niobate asymmetrical mode piezoelectric MEMS resonators,” *IFCS 2018 - IEEE Int. Freq. Control Symp.*, pp. 1–5, 2018.

[2] M. Swan, “Sensor mania! The Internet of Things, wearable computing, objective metrics, and the quantified self 2.0,” *J. Sens. Actuator Networks*, 2012.

[3] A. Costanzo and D. Masotti, “Energizing 5G: Near-and far-field wireless energy and data transfer as an enabling technology for the 5G IoT,” *IEEE Microw. Mag.*, 2017.

[4] D. Blaauw *et al.*, “IoT design space challenges: Circuits and systems,” in *Digest of Technical Papers - Symposium on VLSI Technology*, 2014.

[5] H. B. Singh and R. Pal, “Submarine communications,” *Def. Sci. J.*, vol. 43, no. 1, pp. 43–51, 1993.

[6] S. Yarkan, S. Güzelgöz, H. Arslan, and R. Murphy, “Underground mine communications: A survey,” *IEEE Commun. Surv. Tutorials*, vol. 11, no. 3, pp. 125–142, 2009.

[7] J. K. Hargreaves and R. D. Hunsucker, *The High-Latitude Ionosphere and Its Effects on Radio Propagation*. Cambridge: Cambridge University Press, 2007.

[8] R. H. Olsson, “Microsystems Technology Office (MTO) Broad Agency Announcement: A MEchanically Based Antenna (AMEBA) (Document HR001117S0007),” 2016.

[9] H. A. Wheeler, “Fundamental limitations of a small VLF antenna for submarines,” *IRE Trans. Antennas Propag.*, 1958.

[10] Waheed-uz-Zaman, “Design and construction of very low frequency antenna,” *J. Basic Appl. Sci.*, 2011.

[11] G. A. Ashdown, “Study of a VLF distributed antenna array,” in *AGARD, ELF/VLF/LF Radio Propagation and Systems Aspects 13 p (see N93-30727 11-32)*, 1993.

[12] T. Simpson, M. Roberts, and E. Berg, “Developing a broadband circuit model for the Cutler VLF antenna,” in *IEEE Antennas and Propagation Society, AP-S International Symposium (Digest)*, 2001, vol. 4, pp. 250–253.

[13] C. A. Balanis, *Antenna Theory Analysis and Design Third Edition*, no. 3. 2005.

[14] H. T. Friis, “A note on a simple transmission formula,” *Proc. IRE*, 1946.

[15] H. A. Wheeler, “Fundamental limitations of small antennas,” *Proc. IRE*, vol. 35, no. 12, pp. 1479–1484, 1947.

[16] S. R. Best, “A discussion on power factor, quality factor and efficiency of small antennas,” in *IEEE Antennas and Propagation Society, AP-S International Symposium (Digest)*, 2007.

[17] C. E. Shannon, “Communication in the presence of noise,” *Proc. IRE*, 1949.

[18] H. A. Wheeler, “Fundamental limitations of small antennas,” *Proc. IRE*, vol. 35, no. 12, pp. 1479–1484, 1947.

[19] L. J. Chu, “Physical limitations of omni-directional antennas,” *J. Appl. Phys.*, vol. 19, p. 1163, 1948.

[20] R. E. Collin and S. Rothschild, “Evaluation of antenna Q,” *IEEE Trans. Antennas Propag.*, vol. 12, no. 1, pp. 23–27, 1964.

[21] R. C. Hansen, “Fundamental limitations in antennas,” *Proc. IEEE*, vol. 69, no. 2, pp. 170–182, 1981.

[22] J. S. McLean, “A re-examination of the fundamental limits on the radiation Q of electrically small antennas,” *IEEE Trans. Antennas Propag.*, vol. 44, no. 5, p. 672, 1996.

[23] R. F. Harrington, “Effect of antenna size on gain, bandwidth, and efficiency,” *J. Res. Natl. Bur. Stand. Sect. D Radio Propag.*, 2012.

[24] D. M. Binkley, J. M. Rochelle, B. K. Swann, L. G. Clonts, and R. N. Goble, “A micropower CMOS, direct-conversion, VLF receiver chip for magnetic-field wireless applications,” *IEEE J. Solid-State Circuits*, 1998.

[25] M. Youssef, A. Yousif, N. El-Sheimy, and A. Noureldin, “A novel earthquake warning system based on virtual MIMO-wireless sensor networks,” in *Canadian Conference on Electrical and Computer Engineering*, 2007.

[26] W. L. Stutzman and G. A. Thiele, “Antenna theory and design,” *IEEE Antennas and Propagation Society Newsletter*. 1981.

[27] H. A. Wheeler, “Small antennas,” *IEEE Trans. Antennas Propag.*, vol. 23, no. 4, pp. 462–469, 1975.

[28] S. R. Best and D. L. Hanna, “A performance comparison of fundamental small-antenna designs,” *IEEE Antennas Propag. Mag.*, vol. 52, no. 1, pp. 47–70, 2010.

[29] C. Pfeiffer, “Fundamental efficiency limits for small metallic antennas,” *IEEE Trans. Antennas Propag.*, vol. 65, no. 4, pp. 1642–1650, 2017.

[30] C. E. Shannon, “A mathematical theory of communication,” *Bell Syst. Tech. J.*, vol. 27, no. 3, pp. 379–423, 1948.

[31] R. Guertler, “Impedance transformation in folded dipoles,” *Proc. IRE*, vol. 38, no. 9, pp. 1042–1047, 1950.

[32] S. R. Best, “The radiation properties of electrically small folded spherical helix antennas,” *IEEE Trans. Antennas Propag.*, vol. 52, no. 4, pp. 953–960, 2004.

[33] S. R. Best, “Low Q electrically small linear and elliptical polarized spherical dipole antennas,” *IEEE Trans. Antennas Propag.*, vol. 53, no. 3, pp. 1047–1053, 2005.

[34] J. D. Kraus, “The helical antenna,” *Proc. IRE*, vol. 37, no. 3, pp. 263–272, 1949.

[35] G. S. Smith, “Efficiency of electrically small antennas combined with matching networks,” *IEEE Trans. Antennas Propag.*, vol. 25, pp. 369–373, 1977.

[36] H. A. Wheeler, “The spherical coil as an inductor, shield, or antenna,” *Proc. IRE*, vol. 46, pp. 1595–1602, 1958.

[37] H. L. Thal, “New radiation Q limits for spherical wire antennas,” *IEEE Trans. Antennas Propag.*, vol. 54, pp. 2757–2763, 2006.

[38] J. J. Adams, S. C. Slimmer, T. F. Malkowski, E. B. Duoss, J. A. Lewis, and J. T. Bernhard, “Comparison of spherical antennas fabricated via conformal printing: Helix, meanderline, and hybrid designs,” *IEEE Antennas Wirel. Propag. Lett.*, vol. 10, pp. 1425–1428, 2011.

[39] A. Erentok and R. W. Ziolkowski, “Metamaterial-inspired efficient electrically small antennas,” *IEEE Trans. Antennas Propag.*, vol. 56, no. 3, pp. 691–707, 2008.

[40] C. Pfeiffer, X. Xu, S. R. Forrest, and A. Grbic, “Direct transfer patterning of electrically small antennas onto three-dimensionally contoured substrates,” *Adv. Mater.*, vol. 24, no. 9, pp. 1166–1170, 2012.

[41] M. Shahpari and D. V. Thiel, “Fundamental limitations for antenna radiation efficiency,” *IEEE Trans. Antennas Propag.*, vol. 66, no. 8, pp. 3894–3901, 2018.

[42] L. Jelinek, K. Schab, and M. Capek, “Radiation efficiency cost of resonance tuning,” *IEEE Trans. Antennas Propag.*, vol. 66, no. 12, pp. 6716–6723, 2018.

[43] J. D. Maines and E. G. S. Paige, “Surface-acoustic-wave devices for signal processing applications,” *Proc. IEEE*, vol. 64, no. 5, pp. 639–652, 1976.

[44] C. K. Campbell, “Applications of surface acoustic and shallow bulk acoustic wave devices,” *Proc. IEEE*, vol. 77, no. 10, pp. 1453–1484, 1989.

[45] R. Lu, T. Manzaneque, Y. Yang, L. Gao, A. Gao, and S. Gong, “A radio frequency nonreciprocal network based on switched acoustic delay lines,” *IEEE Trans. Microw. Theory Tech.*, vol. 67, no. 4, pp. 1516–1530, 2019.

[46] D. J. Griffiths, *Introduction to Electrodynamics*. Pearson Education, 2013.

[47] T. Nan *et al.*, “Acoustically actuated ultra-compact NEMS magnetoelectric antennas,” *Nat. Commun.*, vol. 8, no. 1, p. 296, 2017.

[48] M. A. Kemp *et al.*, “A high Q piezoelectric resonator as a portable VLF transmitter,” *Nat. Commun.*, vol. 10, no. 1, 2019.

[49] N. Barani and K. Sarabandi, “Mechanical antennas: Emerging solution for very-low frequency (VLF) communication,” in *2018 IEEE Antennas and Propagation Society International Symposium and USNC/URSI National Radio Science Meeting, APSURSI 2018 - Proceedings*, 2018, pp. 95–96.

[50] M. N. S. Prasad, S. Selvin, R. U. Tok, Y. Huang, and Y. Wang, “Directly modulated spinning magnet arrays for ULF communications,” in *IEEE Radio and Wireless Symposium, RWS*, 2018, pp. 171–173.

[51] M. Golkowski, J. Park, J. Bittle, B. Babaiahgari, R. A. L. Rorrer, and Z. Celinski, “Novel mechanical magnetic shutter antenna for ELF /VLF radiation,” in *2018 IEEE Antennas and Propagation Society International Symposium and USNC/URSI National Radio Science Meeting, APSURSI 2018 - Proceedings*, 2018, pp. 65–66.

[52] Z. Yao, Y. E. Wang, S. Keller, and G. P. Carman, “Bulk acoustic wave-mediated multiferroic antennas: Architecture and performance bound,” *IEEE Trans. Antennas Propag.*, vol. 63, no. 8, pp. 3335–3344, 2015.

[53] R. D. Mindlin, “Electromagnetic radiation from a vibrating quartz plate,” *Int. J. Solids Struct.*, vol. 9, no. 6, pp. 697–702, 1973.

[54] P. C. Y. Lee, Y. G. Kim, and J. H. Prevost, “Electromagnetic radiation from doubly rotated piezoelectric crystal plates vibrating at thickness frequencies,” *J. Appl. Phys.*, vol. 67, no. 11, pp. 6633–6642, 1990.

[55] J. P. Domann and G. P. Carman, “Strain powered antennas,” *J. Appl. Phys.*, vol. 121, no. 4, 2017.

[56] M. Gustafsson, M. Capek, and K. Schab, “Tradeoff between antenna efficiency and Q-factor,” *IEEE Trans. Antennas Propag.*, vol. 67, no. 4, pp. 2482–2493, 2019.

[57] A. Díaz-Ballester *et al.*, “Charge storage and retention in electret dielectric layers for energy harvesting applications,” in *2014 IEEE 9th IberoAmerican Congress on Sensors*, 2014, pp. 1–4.

[58] W. Künstler, Z. Xia, T. Weinhold, A. Pucher, and R. Gerhard-Multhaupt, “Piezoelectricity of porous polytetrafluoroethylene single- and multiple-film electrets containing high charge densities of both polarities,” *Appl. Phys. A Mater. Sci. Process.*, vol. 70, no. 1, pp. 5–8, 2000.

[59] Y. Suzuki, “Development of a MEMS energy harvester with high-perfomance polymer electrets,” in *PowerMEMS*, 2010, pp. 47–52.

[60] U. Mescheder, B. Müller, S. Baborie, and P. Urbanovic, “Properties of SiO2 electret films charged by ion implantation for MEMS-based energy harvesting systems,” *J. Micromechanics Microengineering*, vol. 19, p. 094003, 2009.

[61] H. Asanuma, H. Oguchi, M. Hara, R. Yoshida, and H. Kuwano, “Ferroelectric dipole electrets for output power enhancement in electrostatic vibration energy harvesters,” *Appl. Phys. Lett.*, vol. 103, p. 162901, 2013.

[62] J. D. Larson, P. D. Bradley, S. Wartenberg, and R. C. Ruby, “Modified Butterworth-Van Dyke circuit for FBAR resonators and automated measurement system,” in *Proceedings of the IEEE Ultrasonics Symposium*, 2000, pp. 863–868.

[63] G. Piazza, P. J. Stephanou, and A. P. Pisano, “Piezoelectric aluminum nitride vibrating contour-node MEMS resonators,” *J. Microelectromechanical Syst.*, vol. 15, no. 6, pp. 1406–1418, Dec. 2006.

[64] K. K. Park, M. Kupnik, H. J. Lee, Ö. Oralkan, and B. T. Khuri-Yakub, “Zero-bias resonant sensor with an oxide-nitride layer as charge trap,” in *Proceedings of IEEE Sensors*, 2010, pp. 1024–1028.

[65] S. Boisseau, A.-B. Duret, J.-J. Chaillout, and G. Despesse, “New DRIE-patterned electrets for vibration energy harvesting,” *EPJ Web Conf.*, vol. 33, p. 02010, 2012.

[66] J. J. Lowke, “Theory of electrical breakdown in air—the role of metastable oxygen molecules,” *J. Phys. D. Appl. Phys.*, vol. 25, no. 2, p. 202, 1992.

[67] N. H. Malik and A. H. Qureshi, “A review of electrical breakdown in mixtures of SF6 and other gases,” *IEEE Trans. Electr. Insul.*, vol. 14, no. 1, pp. 1–13, 1979.

[68] Yao-Joe Yang, M.-A. Gretillat, and S. D. Senturia, “Effect of air damping on the dynamics of nonuniform deformations of microstructures,” in *Proceedings of International Solid State Sensors and Actuators Conference*, 1997, pp. 1093–1096.

[69] L. Mol, L. A. Rocha, E. Cretu, and R. F. Wolffenbuttel, “Squeezed film damping measurements on a parallel-plate MEMS in the free molecule regime,” in *TRANSDUCERS 2009 - 15th International Conference on Solid-State Sensors, Actuators and Microsystems*, 2009, pp. 1425–1428.

[70] R. A. Draughn and A. Catlin, “Effect of low pressure on surface charge of electrets,” *J. Electrochem. Soc.*, vol. 115, no. 4, pp. 391–394, 1968.

[71] G. Piazza, P. J. Stephanou, and A. P. Pisano, “Piezoelectric aluminum nitride vibrating contour-mode MEMS resonators,” *J. Microelectromechanical Syst.*, vol. 15, no. 6, pp. 1406–1418, Dec. 2006.

[72] X. Liu, Y. Wang, X. Le, Z. Xu, C. Wu, and J. Xie, “A dual-driving piezoelectric DETF resonator with high quality factor and low multimode effect,” *J. Micromechanics Microengineering*, vol. 28, no. 10, p. 105006, 2018.

[73] A. Ballato and J. G. Gualtieri, “Advances in high-Q piezoelectric resonator materials and devices,” *IEEE Trans. Ultrason. Ferroelectr. Freq. Control*, vol. 41, no. 6, pp. 834–844, 1994.

[74] Y. Yang, A. Gao, R. Lu, and S. Gong, “5 GHz lithium niobate MEMS resonators with high FoM of 153,” in *IEEE Micro Electro Mechanical Systems (MEMS)*, 2017, pp. 942–945.

[75] R. Bechmann, “Elastic and piezoelectric constants of alpha-quartz,” *Phys. Rev.*, vol. 110, p. 1060, 1958.

[76] S. A. Chandorkar, M. Agarwal, R. Melamud, R. N. Candler, K. E. Goodson, and T. W. Kenny, “Limits of quality factor in bulk-mode micromechanical resonators,” in *Proceedings of the IEEE International Conference on Micro Electro Mechanical Systems (MEMS)*, 2008, pp. 74–77.

[77] A. Safari and E. K. Akdoğan, Eds., *Piezoelectric and Acoustic Materials for Transducer Applications*. New York, NY USA: Springer, 2008.

[78] G. M. Rebeiz, *RF MEMS: Theory, Design, and Technology*. John Wiley & Sons, 2003.

[79] G. K. Fedder, “Capacitive resonators,” in *Resonant MEMS: Fundamentals, Implementation, and Application*, Wiley Online Library, 2015, pp. 119–146.

[80] N. Zouache and A. Lefort, “Electrical breakdown of small gaps in vacuum,” *IEEE Trans. Dielectr. Electr. Insul.*, vol. 4, no. 4, pp. 358–364, 1997.

[81] A. Emad, R. Lu, M.-H. Li, Y. Yang, T. Wu, and S. Gong, “Resonant torsinal micro-actuators using thin-film lithium niobate,” in *IEEE Micro Electro Mechanical Systems (MEMS)*, 2019.

[82] B. J. Kim *et al.*, “Fabrication of thick periodically-poled lithium niobate crystals by standard electric field poling and direct bonding,” *J. Opt. Soc. Korea*, vol. 14, no. 4, pp. 420–423, 2010.

[83] I. Camlibel, “Spontaneous polarization measurements in several ferroelectric oxides using a pulsed-field method,” *J. Appl. Phys.*, vol. 40, p. 1690, 1969.

[84] J. H. Ro, O. Y. Jeon, T. H. Kim, J. H. Ro, and M. Cha, “Non-stoichiometric defect effect on coercive field in lithium niobate crystals,” *Ferroelectrics*, vol. 269, no. 1, pp. 231–236, 2002.

[85] H. Asanuma, H. Oguchi, M. Hara, and H. Kuwano, “A spontaneous polarization electret for electrostatic vibration energy harvesting,” in *Transducers and Eurosensors XXVII*, 2013, pp. 1332–1335.

[86] A. Gemant, “Electrets,” *Phys. Today*, vol. 2, no. 3, p. 8, 1949.

[87] A. E. Hassanien, M. Breen, M.-H. Li, and S. Gong, “Acoustically driven and modulation inducible radiating elements,” *arXiv:1906.07797*, 2019.

[88] M.-G. Kang, W.-S. Jung, C.-Y. Kang, and S.-J. Yoon, “Recent progress on PZT based piezoelectric energy harvesting technologies,” *Actuators*, vol. 5, no. 1, p. 5, 2016.

[89] Z. Yang and J. Zu, “Comparison of PZN-PT, PMN-PT single crystals and PZT ceramic for vibration energy harvesting,” *Energy Convers. Manag.*, vol. 122, pp. 321–329, 2016.

[90] G. Piazza, “Contour-mode aluminum nitride piezoelectric MEMS resonators and filters,” in *MEMS-Based Circuits and Systems for Wireless Communication*, 1st ed., New York, NY USA: Springer, 2013, pp. 29–54.

[91] J. G. Gualtieri, J. A. Kosinski, and A. Ballato, “Piezoelectric materials for acoustic wave applications,” *IEEE Trans. Ultrason. Ferroelectr. Freq. Control*, 1994.

[92] Z. Hao, A. Erbil, and F. Ayazi, “An analytical model for support loss in micromachined beam resonators with in-plane flexural vibrations,” *Sensors Actuators A Phys.*, vol. 109, no. 1–2, pp. 156–164, 2003.

[93] Z. Hao and F. Ayazi, “Support loss in the radial bulk-mode vibrations of center-supported micromechanical disk resonators,” *Sensors Actuators A Phys.*, vol. 134, no. 2, pp. 582–593, 2007.

[94] Y.-H. Cho, A. P. Pisano, and R. T. Howe, “Viscous damping model for laterally oscillating microstructures,” *J. Microelectromechanical Syst.*, vol. 3, no. 2, pp. 81–87, 1994.

[95] R. Tabrizian, M. Rais-Zadeh, and F. Ayazi, “Effect of phonon interactions on limiting the fQ product of micromechanical resonators,” in *TRANSDUCERS 2009-2009 International Solid-State Sensors, Actuators and Microsystems Conference*, 2009, pp. 2131–2134.

[96] A. B. Pippard, “Theory of ultrasonic attenuation in metals and magneto-acoustic oscillations,” *Proc. R. Soc. London. Ser. A. Math. Phys. Sci.*, vol. 257, no. 1289, pp. 165–193, 1960.

[97] Z. Djurić, “Mechanisms of noise sources in microelectromechanical systems,” *Microelectron. Reliab.*, vol. 40, no. 6, pp. 919–932, 2000.

[98] J. G. Smits, “Influence of moving domain walls and jumping lattice defects on complex material coefficients of piezoelectrics,” *IEEE Trans. Sonics Ultrason.*, vol. 23, no. 3, pp. 168–173, 1976.

[99] R. Holland, “Representation of dielectric, elastic, and piezoelectric losses by complex coefficients,” *IEEE Trans. Sonics Ultrason.*, vol. 14, no. 1, pp. 18–20, 1967.

[100] H. P. Loebl, C. Metzmacher, R. F. Milsom, P. Lok, F. Van Straten, and A. Tuinhout, “RF bulk acoustic wave resonators and filters,” *J. Electroceramics*, vol. 12, no. 1–2, pp. 109–118, 2004.

[101] S. Sherrit, H. D. Wiederick, and B. K. Mukherjee, “Accurate equivalent circuits for unloaded piezoelectric resonators,” in *1997 IEEE Ultrasonics Symposium Proceedings. An International Symposium (Cat. No. 97CH36118)*, 1997, vol. 2, pp. 931–935.

[102] A. K. Jonscher, “Dielectric relaxation in solids,” *J. Phys. D. Appl. Phys.*, vol. 32, no. 14, p. R57, 1999.

[103] A. K. Jonscher, “Physical basis of dielectric loss,” *Nature*, vol. 253, no. 5494, pp. 717–719, 1975.

[104] T. Tsurumi, Y. Kil, K. Nagatoh, H. Kakemoto, S. Wada, and S. Takahashi, “Intrinsic elastic, dielectric, and piezoelectric losses in lead zirconate titanate ceramics determined by an immittance-fitting method,” *J. Am. Ceram. Soc.*, vol. 85, no. 8, pp. 1993–1996, 2002.

[105] A. V Mezheritsky, “Elastic, dielectric, and piezoelectric losses in piezoceramics: How it works all together,” *IEEE Trans. Ultrason. Ferroelectr. Freq. Control*, vol. 51, no. 6, pp. 695–707, 2004.

[106] S. Zhang and T. R. Shrout, “Relaxor-PT single crystals: Observations and developments,” *IEEE Trans. Ultrason. Ferroelectr. Freq. Control*, vol. 57, no. 10, pp. 2138–2146, 2010.

[107] G. Arlt and H. Dederichs, “Complex elastic, dielectric and piezoelectric constants by domain wall damping in ferroelectric ceramics,” *Ferroelectrics*, vol. 29, no. 1, pp. 47–50, 1980.

[108] A. Thakre *et al.*, “Enhanced mechanical quality factor of 32 Mode Mn doped 71Pb (Mg 1/3 Nb 2/3) O3–29PbZrTiO 3 piezoelectric single crystals,” *Electron. Mater. Lett.*, pp. 1–8, 2020.

[109] L. Zheng *et al.*, “Origin of improvement in mechanical quality factor in acceptor-doped relaxor-based ferroelectric single crystals,” *Phys. Rev. Appl.*, vol. 9, no. 6, p. 64028, 2018.

[110] S. Zhang, S.-M. Lee, D.-H. Kim, H.-Y. Lee, and T. R. Shrout, “Characterization of Mn-modified Pb (Mg 1⁄ 3 Nb 2⁄ 3) O3–PbZr O3–PbTi O3 single crystals for high power broad bandwidth transducers,” *Appl. Phys. Lett.*, vol. 93, no. 12, p. 122908, 2008.

[111] R. Lu and S. Gong, “Study of thermal nonlinearity in lithium niobate-based MEMS resonators,” in *2015 Transducers-2015 18th International Conference on Solid-State Sensors, Actuators and Microsystems (TRANSDUCERS)*, 2015, pp. 1993–1996.

[112] J. Segovia-Fernandez and G. Piazza, “Thermal nonlinearities in contour mode AlN resonators,” *J. Microelectromechanical Syst.*, vol. 22, no. 4, pp. 976–985, 2013.

[113] S. Yarlagadda, M. H. W. Chan, H. Lee, G. A. Lesieutre, D. W. Jensen, and R. S. Messer, “Low temperature thermal conductivity, heat capacity, and heat generation of PZT,” *J. Intell. Mater. Syst. Struct.*, vol. 6, no. 6, pp. 757–764, 1995.

[114] S. N. Kallaev, G. G. Gadzhiev, I. K. Kamilov, Z. M. Omarov, S. A. Sadykov, and L. A. Reznichenko, “Thermal properties of PZT-based ferroelectric ceramics,” *Phys. Solid State*, vol. 48, no. 6, pp. 1169–1170, 2006.

[115] M. Tachibana and E. Takayama-Muromachi, “Thermal conductivity and heat capacity of the relaxor ferroelectric [PbMg 1/3 Nb 2/3 O 3] 1− x [PbTiO 3] x,” *Phys. Rev. B*, vol. 79, no. 10, p. 100104, 2009.

[116] S. Yao *et al.*, “Growth, optical and thermal properties of near-stoichiometric LiNbO3 single crystal,” *J. Alloys Compd.*, vol. 455, no. 1–2, pp. 501–505, 2008.

[117] D. Damjanovic, “A morphotropic phase boundary system based on polarization rotation and polarization extension,” *Appl. Phys. Lett.*, vol. 97, no. 6, p. 62906, 2010.

[118] A.-B. M. A. Ibrahim, R. Murgan, M. K. A. Rahman, and J. Osman, “Morphotropic phase boundary in ferroelectric materials,” *Ferroelectr. Eff.*, 2011.

[119] S. Trolier-McKinstry, S. Zhang, A. J. Bell, and X. Tan, “High-performance piezoelectric crystals, ceramics, and films,” *Annu. Rev. Mater. Res.*, vol. 48, pp. 191–217, 2018.

[120] K. Uchino, “High electromechanical coupling piezoelectrics: relaxor and normal ferroelectric solid solutions,” *Solid State Ionics*, vol. 108, no. 1–4, pp. 43–52, 1998.

[121] X. Jiang, F. Tang, J. T. Wang, and T.-P. Chen, “Growth and properties of PMN–PT single crystals,” *Phys. C Supercond. Its Appl.*, vol. 364, pp. 678–683, 2001.

[122] Z.-W. Yin, H.-S. Luo, P.-C. Wang, and G.-S. Xu, “Growth, characterization and properties of relaxor ferroelectric PMN-PT single crystals,” *Ferroelectrics*, vol. 229, no. 1, pp. 207–216, 1999.

[123] M. D. Aggarwal, F. Kochary, B. G. Penn, and J. Miller, “Bulk crystal growth of piezoelectric PMN-PT crystals using gradient freeze technique for improved SHM sensors,” in *Structural Health Monitoring*, 2007.

[124] S. Haykin, *Communication Systems*, Fourth. John Wiley & Sons, 2000.

[125] W. Yao and Y. Wang, “Direct antenna modulation: A promise for ultra-wideband (UWB) transmitting,” in *2004 IEEE MTT-S International Microwave Symposium Digest (IEEE Cat. No. 04CH37535)*, 2004, vol. 2, pp. 1273–1276.

[126] M. Manteghi, “A wideband electrically small transient-state antenna,” *IEEE Trans. Antennas Propag.*, vol. 64, no. 4, pp. 1201–1208, 2016.

[127] K. Schab, D. Huang, and J. J. Adams, “Pulse characteristics of a direct antenna modulation transmitter,” *IEEE Access*, vol. 7, pp. 30213–30219, 2019.

[128] H. Wolff, “High-speed frequency-shift keying of LF and VLF radio circuits,” *IRE Trans. Commun. Syst.*, vol. 5, no. 3, pp. 29–42, 1957.

[129] J. Galejs, “Switching of reactive elements in high-Q antennas,” *IEEE Trans. Commun. Syst.*, vol. 11, no. 2, pp. 254–255, 1963.

[130] J. R. Clark, W. T. Hsu, M. A. Abdelmoneum, and C. T. C. Nguyen, “High-Q UHF micromechanical radial-contour mode disk resonators,” *J. Microelectromechanical Syst.*, 2005.

[131] “PI Piezo Technology: Piezoelectric Materials.” [Online]. Available: https://www.piceramic.com/en/products/piezoelectric-materials/.

[132] K. K. Rajan, M. Shanthi, W. S. Changa, J. Jin, and L. C. Lim, “Dielectric and piezoelectric properties of [0 0 1] and [0 1 1]-poled relaxor ferroelectric PZN–PT and PMN–PT single crystals,” *Sensors Actuators, A Phys.*, vol. 133, no. 1, pp. 110–116, 2007.

[133] T. R. Shrout and J. Fielding, “Relaxor ferroelectric materials,” in *IEEE Symposium on Ultrasonics*, 1990, pp. 711–720.

[134] A. R. Silva, J. O. Rossi, L. P. S. Neto, and M. Ueda, “Adherence enhancement of metallic film on PZT-type ceramic using nitrogen plasma implantation,” *IEEE Trans. Plasma Sci.*, vol. 42, no. 10, pp. 3173–3179, 2014.